Contents

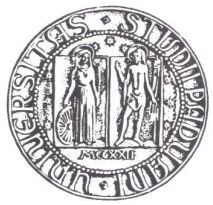

UNIVERSITA' DEGLI STUDI DI PADOVA
FACOLTA' DI SCIENZE MM.FF.NN.
Scuola di Dottorato in Scienza ed Ingegneria dei Materiali
XX CICLO

TESI DI DOTTORATO

FRICTION PROPERTIES OF HOMOGENEOUS AND MICROPATTERNED SURFACES

Direttore della Scuola: Prof. Gaetano Granozzi
Supervisore: Prof. Giampaolo Mistura
Co-supervisore: Prof. Lorenzo Bruschi

Candidato: Giovanni Fois

ANNO ACCADEMICO 2007/2008

A Elena

Abstract (Italiano)

I fenomeni legati alla tribologia quali adesione, attrito e usura si manifestano quando due solidi vengono messi in contatto. Come le dimensioni dei dispositivi si riducono alle micro- e nanoscale, il rapporto superficie-volume aumenta e gli effetti dovuti alle forze di attrazione tra corpi (gravità e inerzia) diventano insignificanti rispetto a quelle superficiali (van der Waals, capillari, elettrostatiche e legami chimici). A queste scale, l'uso di lubrificanti liquidi ed i sistemi macroscopici di riduzione dell'usura sono inefficaci. Nei sistemi microelettromeccanici (MEMS) le forze di attrito e quelle statiche d'interfaccia sono comparabili con le forze che muovono il dispositivo. Nuove strategie devono, quindi, essere messe a punto per ridurre i fenomeni di attrito.

In questa tesi io ho investigato i meccanismi microscopici che regolano l'attrito. Tramite la tecnica della microbilancia a cristallo di quarzo, ho misurato la viscosità interfacciale di monostrati (ML) di gas puri depositati su superfici di piombo (111) estrememante uniformi. Per i film di azoto a temperature sotto i 15K non si osservano effetti di dissipazione, suggerendo che questi film siano rigidamente ancorati alla superficie oscillante degli elettrodi. Aumentando la temperatura fino ai 20K vediamo scivolamento dei film d'azoto per ricoprimenti superiori a circa 0,5 MLs nominali. Un comportamento analogo è mostrato anche dai film di Argon. Per i film di Neon abbiamo invece osservato una marcata transizione di *depinning* che separa una regione a basso ricoprimento superficiale, dove il film è fermamente ancorato al substrato oscillante, da una regione ad alto ricoprimento nella quale si osserva scivolamento all'interfaccia solido fluido. Questi dati suggeriscono che nel sistema avvenga un depinning strutturale dei film di Ne solido quando diventano incommensurati con la superficie di piombo. Con questo sistema ho anche studiato il contributo elettronico all'attrito totale attraversando la transizione superconduttiva. I film di Ne non mostrano nessun comportamento anomalo per la dissipazione attorno a Tc.

Con la tecnica della QCM ho anche misurato l'attrito tra i film di Ne e le superfici di oro. Il tempo di scivolamento calcolato per questo sistema era un ordine di grandezza inferiore a quello calcolato per il piombo. Gli effetti dovuti all'accoppiamento tra gli elettroni superficiali e gli atomi adsorbiti potrebbero essere grossi per questo sistema. Allora è stato depositato uno strato isolante di Kr crescente per ridurre

questo accoppiamento. Per ricoprimenti di Kr fino a 2ML è stato misurato un aumento del tempo di scivolamento mentre per ricoprimenti più alti si è osservato un comportamento inverso.

A temperatura ambiente e criogenica è stato svolto uno studio preliminare per valutare lo scivolamento di nanoparticelle di oro del diametro di $15nm$ depositate su superfici d'oro. Le misure mostrano la inaspettata presenza di scivolamento ad una $T = 5,5K$ su superfici lisce d'oro mentre per superfici rugose è stata trovata una marcata dipendenza dello scivolamento dalla forza esterna applicata .

Infine ho messo a punto una procedura per la realizzazione di superfici di silicio patternate con alchilsilani tramite *micro Contact Printing*. Gli studi preliminari sull'attrito, condotti con una punta di AFM modificata che presenta sulla base un'area di contatto di circa $2 \times 2\mu m^2$, mostrano una riduzione del coefficiente di attrito per la superficie coperta da OTS di un fattore 2 rispetto a quella di silicio.

Abstract (English)

The tribological phenomena of adhesion, friction, and wear arise when solid objects make contact. As the size of devices shrinks to micro- and nanoscales, the surface-to-volume ratio increases and the effects of body forces (gravity and inertia) become insignificant compared with those of surface forces (van der Waals, capillary, electrostatic, and chemical bonding). In this situation, fluids lubrication and wear mitigation methods are ineffective. In microelectromechanical systems (MEMS), tribological and static interfacial forces are comparable with forces driving device motion. Then new strategies must be employed to reduce friction.

In this thesis I have studied the microscopic mechanisms involved in friction. Using a quartz crystal microbalance technique, I have measured the interfacial viscosity of pure gases monolayers deposited on very homogeneous Pb(111) surfaces. For nitrogen films at temperatures below 15 K, no dissipation is detected, suggesting that the N_2 films are rigidly coupled to the oscillating electrode. By raising the temperature close to 20K, we find sliding of the nitrogen film for coverages above about 0,5 nominal layers. Similar behavior is shown by Ar films. For Ne films we have instead observed a pronounced depinning transition separating a low-coverage region, where the film is nearly locked to the oscillating electrode, from a high-coverage region characterized by slippage at the solid-fluid boundary. These data are suggestive of a structural depinning of the solid Ne film when it becomes incommensurate with the lead substrate. With this system I have also studied the electronic contribution to the total friction crossing the superconducting transition of lead. Ne monolayers do not show any anomalous behavior in the dissipation across Tc.

With the QCM technique I have also measured the friction of Ne films on gold surfaces. The calculated slip time was one order of magnitude smaller than for Pb. The effect of the electron coupling with the adsorbate should be high for this system. Then an insulating Kr overlayer was grown on the gold surface to reduce coupling. For Kr coverage lower than 2ML an increase in the slip time was measured while for increasing coverages a reentrant behavior was detected.

A preliminary study of the slippage of $15nm$ diameter gold nanoparticles deposited on gold has been carried out at room and cryogenic temperatures. Measurements reveal unexpected slippage at $T = 5,5K$ for a flat surface while for a rough substrate a strict dependance on the external applied load has been found.

Finally I have developed a formula to produce patterned silicon surfaces via micro contact printing of alkylsilane. Preliminary tribological studies have been done with a modified AFM tip having a square tip wih a contatct area of $\sim 2 \times 2 \mu m^2$. Measurements reveal a reduction of the friction coefficient for OTS patterned surface by a factor 2 with respect to bare silicon.

Introduction

Tribology is the science and technology of interacting surfaces in relative motion[1]. It includes the study and application of the principles of friction, lubrication and wear. The word *tribology* is based upon the Greek *tribos* meaning 'to rub'. Since surface interactions dictate or control the functioning of pratically every device developed by man, tribology has been of central importance for thousands of years. The first practical aspects of friction have their roots in prehistory and along all the human history different strategies were studied to reduce friction and wear. For example Egyptian used wooden rollers to move blocks of stone or statues and liquid lubricant to slide blocks accurately into place. Romans reduced the wear of their soles driving nails in the leather[2]. The first recorded systematic study in the field of tribology is due to Leonardo da Vinci, who in his *Codex* disclosed the first two laws of friction usually attribuited to Amontons[3]. The very comprehensive study on the sliding friction was done two hundreds years later by Coulomb that systematically studied the influence of the five main factors upon friction (nature of materials, extent of surface area, normal force, length of time the surfaces remained in stationary contact and ambient conditions). Thanks to many experimental data, he constructed empirical relations, in particular$F = \mu L$ (L is the normal load), finding that μ doesn't depend on L, on sliding velocity and on contact area. The correct explanation of the empirical relation finded by Coulomb was done in the first decades of the 20th century by Tabor and Bowden[4], in terms of the crucial difference between apparent and real area of contact, due to the surface roughness.

A new impulse in friction studies was done in very recent years by the design and development of miniaturized systems for which reduced dimensions mean an increase in the friction influence because of the increase of the surface to volume.ratio *Micro-Electro-Mechanical Systems* (*MEMS*) are the most developed and used in commercial products like cellulars, automotive sensors, joysticks and so on. A MEMS is the integration of mechanical elements, sensors, actuators, and electronics on a common silicon substrate through microfabrication technology. Figure 1 shows some examples of realized MEMS. The reduced dimensions do not allow to use liquid lubricant. Dry lubricants could be a right answer for the problem. Nevertheless, the understanding of microscopically mechanisms involved in friction and wear processes is necessary to improve the life time and perfomances of these systems.

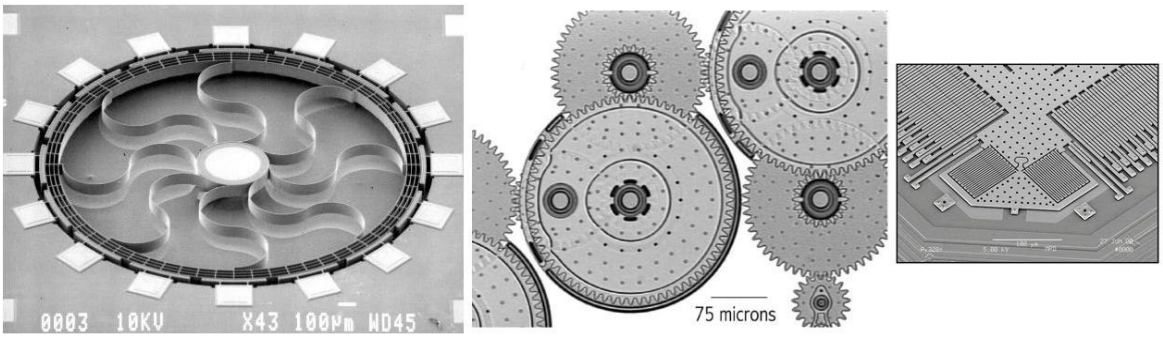

Figure 1: Examples of MEMS.

One possibility is to change the chemical properties of the surface by using a suitable Self Assembled Monolayers (SAM). Recent studies showed that the friction coefficient of alkylthiol SAM is lower than that of gold[42]. The same behavior is shown by alkylsilane SAM on silicon[5] surfaces.

Let us consider the most simple system formed by a flat substrate with some adsorbed atoms (*adatoms*). If the substrate is a metal two mechanisms are involved in the friction process: the first one consists in the excitation of phonons in the substrate, while the other one is relative to the drag of electrons due to their coupling with the moving adsorbate. The electronic channel for dissipation can be eliminated working in the superconducting state. If this were confirmed, this would mean that one can reduce friction by freezing the electronic channel for dissipation in a metal.

Another strategy, suggested by recent studies carried out by Dienwiebel *et al.*[6], consists in using incommensurate surfaces in contact to reduce friction because the sliding friction between two surfaces is very low when they are incommensurated.

Since late 80's new powerful experimental techniques, such as Atomic Force Microscope (AFM), Surface Force Apparatus (SFA) and Quartz Crystal Microbalance (QCM) have succesfully been applied to the study of sliding friction. Despite numerous studies on the microscopic processes of dry friction, fundamental questions are still unanswered. For instance, in the case of a solid monolayer adsorbed on a flat surface does the sliding friction become larger if the substrate is a metal rather than an insulator? An answer to such a question can be provided by studies of the sliding friction on a superconductor: the observation of a change in friction at the superconducting transition temperature of the substrate, T_c, can only be ascribed to the freezing of the electronic dissipation channel. Another question is: two incommensurated solids experience always a low friction regime? And also: is the SAM coating a versatile strategy in the reduction of friction in MEMS?

In this thesis work I have studied the microscopic friction mechanisms. First of all, with the QCM technique I have investigated the electronic contribution to dissipation studying friction of nitrogen and rare gases adsorbed films on a lead sur-

face crossing the superconducting transition. Another way to evaluate the electronic contribution is to cover the metallic surface with an insulating layer to reduce the coupling between surface electrones and adatoms. Then, I have studied the friction variation of Neon adsorbed on gold with increasing Krypton overlayers.

The influence of the surfaces structure has also been studied with QCM technique for gold nanoparticles deposited on a gold surface and for Ne film adsorbed on lead surfaces.

Finally, I have developed a formula to produce patterned silicon surface via micro contact printing of alkyl silane. The tribological properties of the produced samples have been studied with the AFM.

This thesis is organized as follows: the first chapter gives a brief overview of the theoretical models describing the studied systems; in the second chapter the UHV apparatus for QCM measurement is shown; the third chapter gives an overview of the soft lithographic technique involved in the microstructured silicon samples; the fourth chapter illustrates experimental results for friction QCM measurements and finally the fifth chapter shows the preparation of patterned silicon surfaces and the experimental measurements of friction on these samples taken with a modified AFM tip.

Chapter 1

Theoretical models

In this chapter, an introduction to nanofriction theory for the systems surface/adatom and surface/thin film is presented. Starting from the Langevin equation, necessary to understand frictional processes at the nanoscale, the two microscopic mechanisms involved in the dissipation of adsorbed films sliding on metallic flat substrates are also shown. An introduction on electronic and phononic dissipation is presented. Computer simulations of two-dimensional models will be then described, with particular emphasis on Persson's work about dynamical phase transitions. I will, then, introduce recent theoretical models and simulations studying diffusion of nanoclusters on flat cristalline surfaces. Finally I will present a brief overview of the contact mechanical models involved in the Scanning Probe Microscope (SPM) measurements of friction.

The aim of this chapter is not to explain in details all theoretical models, for which I suggest to refer to the bibliography, but to give an overview of theoretical results to better understand experimental results.

1.1 The Langevin equation

Let us consider a generic surface, with any crystalline structure. The motion of an adatom (adsorbed atom) or a system of adatoms sliding on it can be described by using the Langevin equation [1], [7]:

$$m\frac{\partial^2\vec{r}_i}{\partial t^2} + m\eta^*\frac{\partial\vec{r}_i}{\partial t} = -\frac{\partial U(\vec{r}_i)}{\partial\vec{r}_i} - \frac{\partial V(\vec{r}_i)}{\partial\vec{r}_i} + \vec{f}_i + \vec{F} \tag{1.1}$$

here we used the symbols:

$$m = \text{mass of the adatom}$$
$$\vec{r_i} = \text{position of the i-adatom}$$
$$U(\vec{r_i}) = \text{adatom-substrate interactive potential}$$
$$V(\vec{r_i}) = \text{adatom-adatom potential}$$
$$\vec{F} = \text{externally applied force acting on the adsorbate}$$
$$\vec{f_i} = \text{"fluctuating force" acting on the i-adatom}$$

while the term η^*can be represented by a diagonalized matrix:

$$\begin{pmatrix} \eta^*_{\parallel} & 0 & 0 \\ 0 & \eta^*_{\parallel} & 0 \\ 0 & 0 & \eta^*_{\perp} \end{pmatrix}$$

which takes into account the energy dissipation due to friction while the adatom slides, and which is mathematically correlated to fluctuating forces by the fluctuation-dissipation theorem:

$$< f_i^{\alpha}(t) f_j^{\beta}(0) >= 2mK_BT\eta^*_{\alpha\beta}\delta_{ij}\delta(t) \tag{1.2}$$

This expression, universally valid for brownian processes, links fluctuating forces, which represent the effects of substrate thermal motions on the particle, with the dissipative interaction with the substrate itself.

1.1.1 1-dimensional brownian model

We can simplify the model we just introduced by adding some restrictions: first of all, let the surface be crystalline, without any defect or impurity, and suppose we are working at extremely low density, every adatom being thus independent from other ones. If we fix a system of coordinates (x, y) along the surface and consider only the motion along x axis, we have of course a 1-dimensional problem. From now on, we will indicate $\eta^*_{\parallel}$ with the simpler symbol η^*, and thus we write the 1-dimensional Langevin equation, derived simply from 1.1:

$$m\frac{\partial^2 x}{\partial t^2} + m\eta^*\frac{\partial x}{\partial t} = -\frac{\partial U(x)}{\partial x} + f + F \tag{1.3}$$

What we have to do now is to choose an explicit shape for the surface potential similar to the real one:

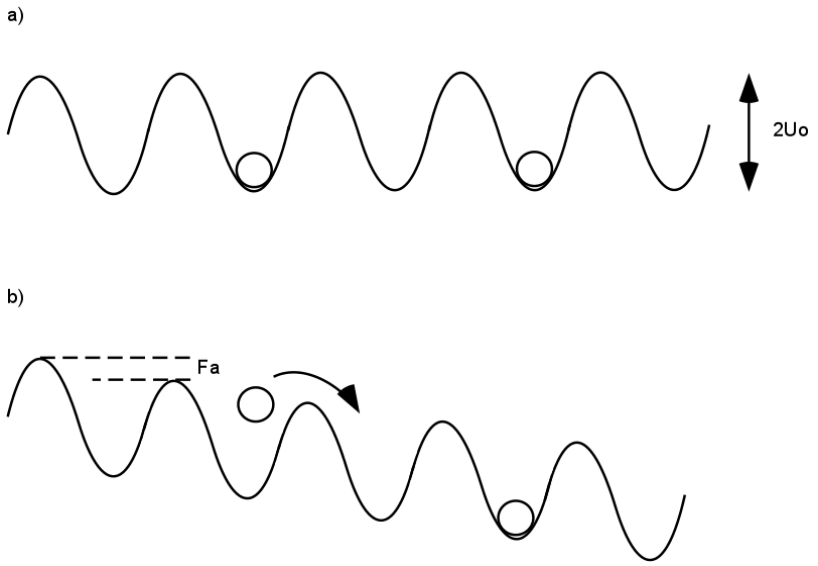

Figure 1.1: a) Surface potential when no external force is applied. b) Total potential when an external force is applied. Now the probability for an adatom to jump in the next minimum (right) is higher than the one to jump in the previous minimum (keft)because of the diffrence in the height of the barriers.

$$U(x) = U_0(1 - \cos(kx)) \tag{1.4}$$

where $k = \frac{2\pi}{a}$, and a is the lattice constant.

Now suppose temperature is sufficiently low to make the thermal energy much lower than the potential barriers around the adatom: $2U_0 - F\frac{a}{2} \gg K_B T$; in this case it can jump only to minima which are first neighbours. F is the externally applied force which, in the case of the QCM technique, is the inertial force acting on the particle due to the substrate's oscillations. Moreover, let η^* be sufficiently high to guarantee a regime in which movements are really limited to first neighbours. Now we use Kramer's theory of activated processes [8] to extimate the drift velocity of the adatoms along the surface. The total value of the potential is $U_{tot}(x) = U(x) - Fx$. What the adatom sees are two energy barriers whose height is different because of the application of the external force. According to Kramer's theory, the probability for the particle to overcome the two walls is different from one barrier to the other:

$$p^+ = \nu e^{-\beta(2U_0 - Fa/2)} \tag{1.5}$$

$$p^- = \nu e^{-\beta(2U_0 + Fa/2)} \tag{1.6}$$

with $\beta = 1/K_BT$ and $\nu = \frac{2\pi U_0}{ma^2\eta^*}$.

The value of the drift velocity is then:

$$v_d = a(p^+ - p^-) = a\nu e^{-2\beta U_0}(e^{\beta Fa/2} - e^{-\beta Fa/2}) \tag{1.7}$$

If we want to extimate the sliding friction we can introduce η, defined as the ratio between F and the impulse of the adatom. We intuitively find that η increases proportionally to η^*:

$$\eta = \frac{F}{mv_d} = \frac{\eta^* e^{2\beta U_0}}{2\pi\beta U_0}\frac{\beta Fa}{e^{\beta Fa/2} - e^{-\beta Fa/2}} \tag{1.8}$$

Typically, in the case of the quartz crystal microbalance, $Fa \ll K_BT$, being $F \approx mA\omega_0^2 \approx 10^{-7}eV/nm$ [1], where A is the amplitude of crystal oscillations and ω_0 represents their frequency. Now if we use the series approximation for exponentials truncated to the first term:

$$\eta = \frac{\eta^*}{2\pi}\frac{K_BT}{U_0}e^{2\beta U_0} \tag{1.9}$$

As we could guess, the friction coefficient has a strong dependence on the temperature, as it tends to infinity as $T \to 0$, limiting case of no thermal excitations: the particle always remains in the same energetic minimum.

This result is valid in the case of extremely low particle density, when we can completely forget the adatom-adatom interaction. Now we can make a little step further and try to understand what may happen by breaking this assumption. A first approximation is to treat atoms like hard spheres, so that an energetic minimum can be occupied by at most one particle. Then we have to multiply p^+ and p^- by the factor $(1 - \vartheta)$ which represents the probability for a sphere to find the place it want to occupy free (ϑ varies continuously in the range between 0 ad 1 and identifies the coverage of the surface). This kind of procedure gives the proportionality:

$$\eta \propto \frac{1}{1 - \vartheta} \tag{1.10}$$

If we increase the coverage we find a continuous decrease in slippage, until the surface is completely covered, when nothing moves; of course this is a very simplified situation but we can learn from it that adatom-adatom interaction can be very important. Moreover, in typical QCM experiments numerical values of parameters such as U_0, η^*, T do not stricly respect given restrictions. As a consequence the regimes of adatoms movement can be different, with jumps of many lattice steps; by the way, when coverage becomes significatively different from zero it can drastically change the adsorbate behaviour as we have just seen.

1.2 Electronic and phononic contributions to sliding friction

The energy dissipated during sliding of simple atoms or thin films along a surface, when the system is ruled by the Van der Waals interaction, takes place involving two kind of mechanisms. Generally speaking, we can say that the first one consists in the excitation of phonons in the substrate, while the other one is relative to the drag of electrons due to their coupling with the moving adsorbate. This latter effect is very debated within the theoretical community, in particular its magnitude. This means that for adsorbates on surfaces the friction coefficient η and the fluctuating force f are due to the coupling between the adsorbate and the vibrational (phonon) and electronic (electron-hole pair) excitations of the substrate.

1.2.1 Electronic contribution

Since phononic and electronic friction are indipendent phenomena we can write:

$$\eta^* = \eta^*_{el} + \eta^*_{fon} \tag{1.11}$$

Now we can try to extimate the electronic contribution to sliding friction through a simple model [1]: let us imagine a metallic substrate whose width is d covered by a layer of physisorbed molecules; if an external electric field is applied in the direction parallel to the surface, then a current will appear, due to the drift of conduction electrons in the metal slab:

$$\vec{J} = ne\vec{v} \tag{1.12}$$

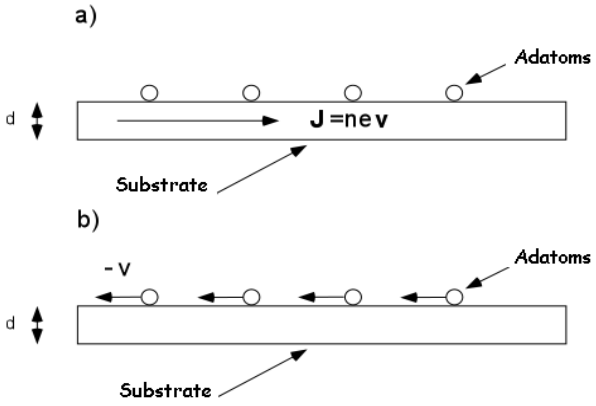

Figure 1.2: Electronic contribution to sliding friction: a) in the reference frame of the lab damping of the translational motion of the adsorbate are detected; b) the same phenomenon, seen in the reference frame of the conduction electrons, is related to the adsorbate-induced increase in film resistivity.

where n is the elecron density and $\vec{v}$ the drift velocity.

Now we analyze the same model from a different point of view, and consider the reference system moving together with the electrons. The adsorbed atoms move with respect to electrons, but they do not move with respect to the metallic lattice. So the only friction force in this case is the electronic one:

$$\vec{F} = m\eta^*_{el}\vec{v} \tag{1.13}$$

and the energy transfer is described as follows:

$$N\vec{F}\vec{v} = Nm\eta^*_{el}\vec{v}^2 \tag{1.14}$$

where N is the total number of adatoms.

In the first reference system we considered, with substrate and adsorbate which do not move, the same energy flow can be ascribed to the resistivity change $\Delta\rho$ induced by the adsorbate. If we indicate with Ad the volume of the metal slab:

$$Ad\vec{J}\vec{E} = Ad\Delta\rho\vec{J}^2 \tag{1.15}$$

From equations 1.14 and 1.15, which describe the same phenomenon from two different points of view, we can derive

$$\Delta\rho = \eta^*_{el}\frac{mN}{An^2e^2d} \tag{1.16}$$

Therefore, from resistivity data we can extimate η^*_{el} and compare it with experimental measurements of η (as defined in 1.8). A systematic study indicates that these two quantities are of the same order of magnitude, within experimental errors, as we can see in the tables [9]:

Electronic friction from resistivity data	
System	$\eta^*_{el}(\mathrm{sec}^{-1})$
C_6H_6/Ag	$7 \cdot 10^8$
C_6H_{12}/Ag	$6 \cdot 10^8$
C_2H_4/Ag	$1.4 \cdot 10^9$
C_2H_6/Ag	$2.8 \cdot 10^8$
Xe/Ag	$3 \cdot 10^8$

Total friction QCM data	
System	$\eta(\mathrm{sec}^{-1})$
H_2O/Ag	$3 \cdot 10^8$
C_6H_{12}/Ag	$5 \cdot 10^8$
N_2/Au	$3 \cdot 10^8$
Xe/Au	$1 \cdot 10^9$
Kr/Au	$1 \cdot 10^8$

Resistivity data suggest that the electronic fritction is quite important. Unfortunately, a sistematic study has not been done. The only data present in literature are those in ref [9] and they have not been confirmed by other measurements.

A direct way to detect the electronic contribution is to study the friction variations when the metal crosses the superconducting transition. When a metal becomes a superconductor, resistance goes to zero and then disappears the electronic contribution. Experimentally, the first detection has been performed in 1998 by Dayo, Arnashrallah and Krim (DAK) [10], who for the first time analyzed the sliding friction of a thin film physisorbed on a superconducting substrate (N_2/Pb) and found a decrease of sliding friction in correspondence to the critical temperature, with friction reduced by a factor ~ 2 when lead became superconductive. Many theories tried, in the last years, to explain this result but no-one is still able to clearly explain the sharpness of the steps separating the two regimes. Other complication: the data have not been reproduced by other groups and the same Krim's group had a lot of difficulties to replicate the original experiment.

1.2.2 Phononic friction

Let us consider a system characterized by physical adsorption, the highest phononic frequency of the substrate being ω_c. If an external force acts on the adsorbate sliding on the surface, then the phononic contribution to sliding friction can be deduced from a continuous elastic model, in the hypotesis that fluctuating forces frequency is lower than ω_c.

The results given by such a model lead to [11], [1]:

$$F_{fon} = -m\eta^*_{fon}\vec{v} \tag{1.17}$$

$$\eta^*_{fon} \approx \frac{3}{8\pi}\frac{m}{\rho_s}\omega_{\parallel}\left(\frac{\omega_{\parallel}}{c_t}\right)^3 \tag{1.18}$$

where we have implicitly considered only the movements of the adsorbate which are parallel to the surface. In formula 1.18 ρ_s is the density of the substrate, c_t is the velocity of sound in it, and:

$$\omega^2_{\parallel} = \frac{1}{m}\frac{\partial^2 U}{\partial x^2} \tag{1.19}$$

is the frequency of vibrations (parallel to surface) characterizing an adatom located in a local minimum of total potential $U(x)$.

Equations 1.17 and 1.18 refer to processes involving a single phonon, and are valid for adsorption of atoms or small molecules. Moreover they have been deduced for single atoms, without taking into account mutual adatom-adatom interaction which is not always negligible, especially at high coverage. In particular, infrared spectroscopy-based studies indicate a lower phononic dissipation in case of very high coverage due to the destructive interference of elastic waves in the substrate.

Together with "direct" energy transfer to the substrate, Persson describes also another process, caused by the presence of corrugated potential [1]. Due to the interaction of the adsorbate with impurities, steps of the surface, and with the surface potential itself, during sliding it is possible an energy transfer to excitations of the substrate.

1.3 Simulation of 2-dimensional models

The parameter η we defined in 1.8 can be extimated through molecular dynamic computer simulations based on 1.1 [1][7]; such algorithms calculate the equilibrium configurations of an adsorbed film depending on parameters such as temperature, surface potential and coverage. Here we will describe the most significative computer simulations carried out by Persson dealing with the system $Xe/Ag(100)$, but the results are qualitatively valid in general systems concerning simple molecules or atoms interacting weakly (Van der Waals) with the crystalline substrate. Let N be the number of adsorbed particles, M the lateral measure of a square representing the substrate (we use as unit the lattice constant), ϑ the coverage obtained from: $\vartheta = N/(M \cdot M)$; typically $M \approx 10$, and periodic boundary conditions are imposed. We can write the interacting potential adatom-surface:

$$U(\vec{r}) = E_B \left(e^{-2\alpha(z-z_0)} - 2e^{-\alpha(z-z_0)}\right) + U_0 \left(2 - \cos(kx) - \cos(ky)\right) e^{-\beta(z-z_0)} \quad (1.20)$$

where (x, y) is the system of coordinates along the surface, z the normal axis, E_B the binding energy and $2U_0$ the height of energetic barriers of the substrate potential; all these parameters, together with α and β, may be deduced from experiments. In our case, we will consider only a 2-dimensional model, and so $\alpha = \infty$ in 1.20. The interacting adatom-adatom potential is the Lennard-Jones one:

$$v(r) = \varepsilon \left(\left(\frac{r_0}{r}\right)^{12} - 2 \left(\frac{r_0}{r}\right)^{6} \right) \quad (1.21)$$

and $V(r)$ is the sum made on every pair. Energy is measured in terms of ε while fluctuating forces $\vec{f_i}$ are simulated using algorithms which generate random numbers with uniform distribution. This kind of programs work as follows: they solve the Langevin equation numerically, starting from fixed conditions for adatoms coordinates and proceed with discrete time-steps, using for every cycle the conditions found at the end of the previous one.

The order of magnitude of time-steps is lower than τ_s ($\sim 10^{-14}$ sec), defined as:

$$\tau_s = \frac{a}{2\pi} \sqrt{\frac{m}{K_B T}} \quad (1.22)$$

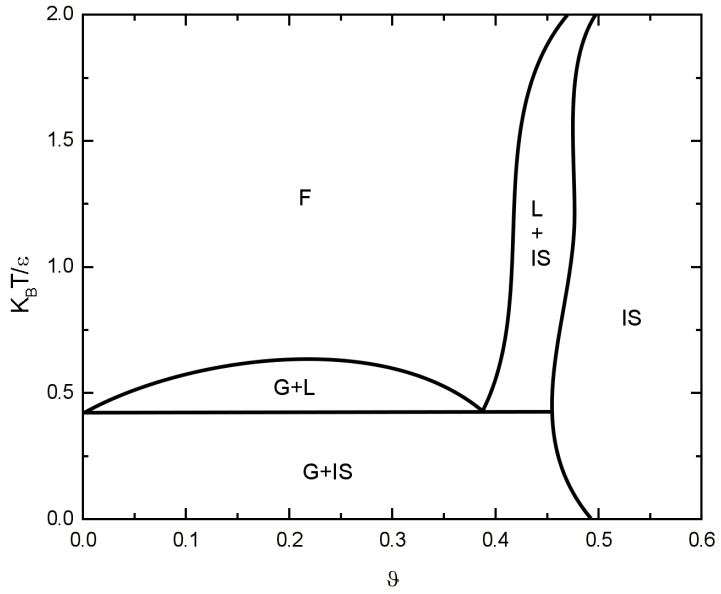

Figure 1.3: Adsorbate fase diagram for low corrugated systems.

which is the time-scale characteristic of particle movements[1]. For this simulations Persson considers only the case of linear response limit were the driving force F in 1.1 is so weak that the drift velocity $\langle v \rangle$ depends linearly with F.

After some cycles, the system reaches the equilibrium condition, with atoms positions minimizing total energy. Of course the configuration strongly depends on T, ϑ and U_0. η is calculated from its "macroscopic" definition, given in the first pages of this chapter, that is the ratio between external force and impulse of the adsorbate:

$$\eta = \frac{F}{m < v >} \tag{1.23}$$

where the velocity is averaged on every particle and on time.

Corrugation of potential U_0 plays an important role to determine the equilibrium configuration. For our studies, we are interested only for systems with low corrugated potential. Let us consider the case $2U_0 = 0.5\varepsilon$: figures 1.3 represent its phase diagram. In the rest of this paragraph we will always consider the system in its own state of equilibrium.

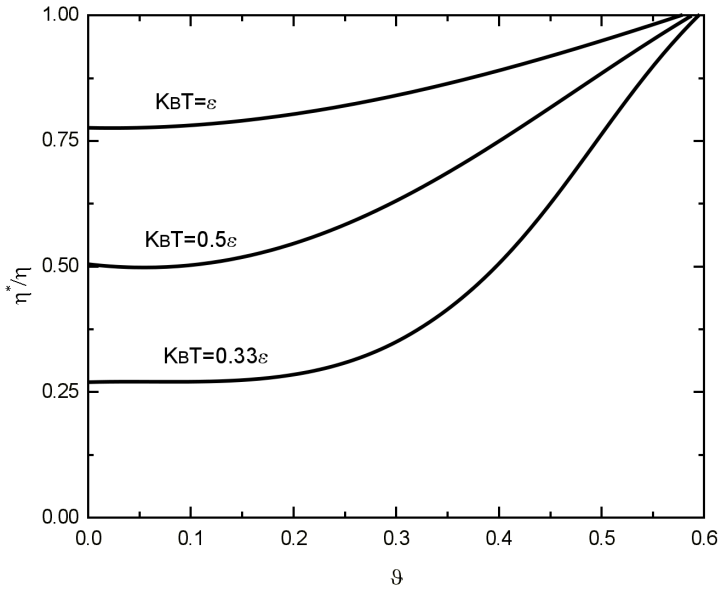

Figure 1.4: The inverse of the normalized drift friction, η^*/η, as a afunction of coverage for several temperature in the case of $2U_0 = 0.5\varepsilon$

In this case potential corrugation is so small that the diagram is very similar to the Lennard-Jones bidimensional one [12]; G, L, F and IS indicate gas, liquid, fluid and incommensurate solid phases, respectively. We define here what "incommensurate solid" and "commensurate solid" mean: if a is the lattice constant of the substrate and b the equilibrium distance between physisorbed molecules (in absence of corrugated potential) the first expression indicates a system in which the ratio b/a is an irrational number; on the other side, if it is a rational number, we say that the solid is commensurate to the surface.

Now we know the equilibrium positions of atoms, and we can start analyzing slippage. To do this, we will calculate the ratio η^*/η, which is a normalization of the sliding friction coefficient defined in 1.23 with respect to the dissipative part of the interaction (see 1.3). Moreover, it is simpler to compare this quantity with experimental data, which are expressed in terms of a "slipping time" τ_s , stricly correlated to η. Here we notice that $\eta^*/\eta =< v > /v_0$, where v_0 is the drift velocity in the case of a flat surface potential ($U_0 = 0$); for further details about the correlation with the slipping time see chapter five.

Let us start analyzing the behaviour in the case of three different temperatures, in the hypothesis of small corrugation ($2U_0 = 0.5\varepsilon$), qualitatively shown in figure 1.4; at high coverage the system is mainly ruled by the adatom-adatom interaction,

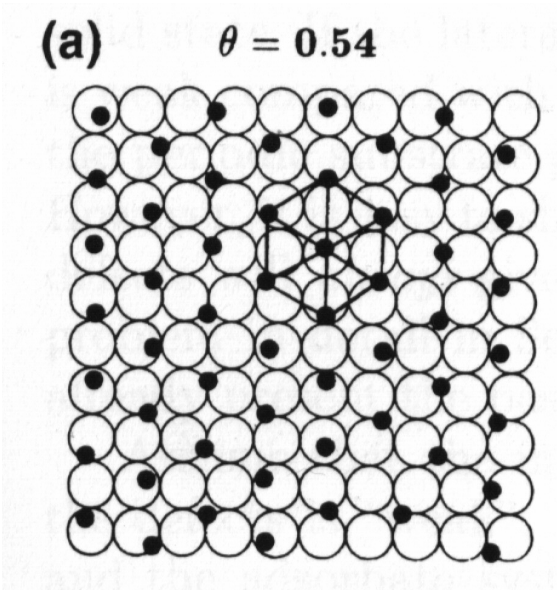

Figure 1.5: Snapshot of the adsorbate structure for $2U_0/\epsilon = 0.5$ and coverage $\theta = 0.54$ where a triangular incommensurate structure occur.

and so we observe great slippage because interaction with potential minima is small; as a consequence η is small and η^*/η tends to unity.

The corresponding adlayer structure is that triangular (fluid phase), shown in figure 1.5. In this case the reciprocal distance between molecules is maximized and any temperature is sufficient to make adatoms overcome the small barriers and move freely. This explains the poor dependence on the temperature of the system.

When coverage becomes small, $V(\vec{r})$ almost vanishes and particles are free to move independently from each other. When $\vartheta < 0.5$ slippage is lower than at higher coverages because $U(\vec{r})$, not so large, is predominant on $V(\vec{r})$.

1.3.1 Role of defects

It is not so realistic to simulate an adsorption surface completely free from defects such as steps, impurities and so on, which give rise to potential barriers drastically affecting adatoms movements on the surface. We have already seen that a low-corrugation potential, for every value of coverage, never locks the film. We will see now that a small numer of randomly distributed impurities on the surface may cause a great increase in friction [7], [13], when coverage is sufficiently high. In fact, an anomaly in the film-substrate interaction (i.e. a step), may lock an adatom; if it is far from other ones (low density) it will be the only one to be locked. But if coverage of the surface is much higher, repulsive Lennard-Jones potential will indirectly lock many other particles.

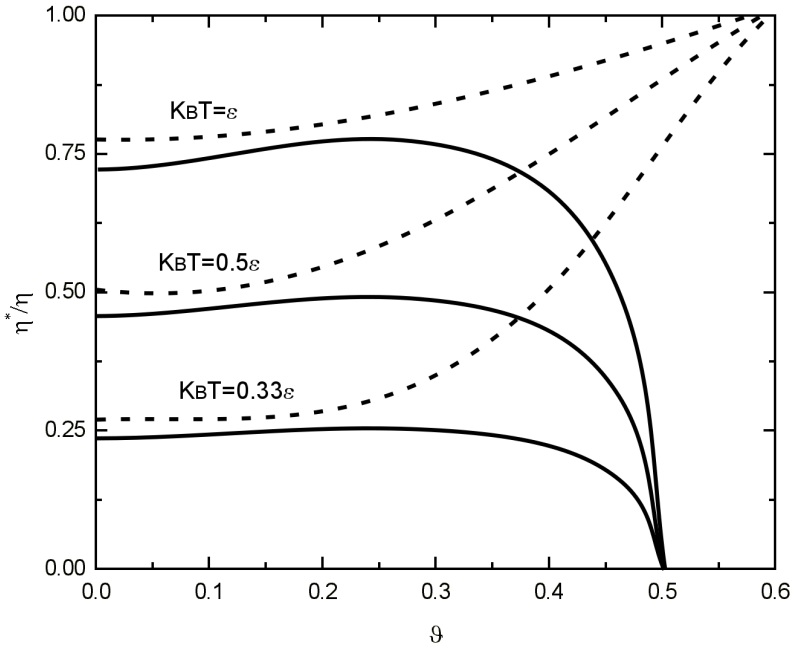

Figure 1.6: Influence of impurities on slippage: calculated slip time as a function of covergae for ideal flat surface (dashed line) and random distribuited impurities.

Let us consider an area $A_d = \xi \cdot \xi$, where N_d defects are randomly located. We can try to extimate the value of the force F_d which acts on the film and locks it. From statistical arguments about random walks [1], we find that the total force acting from defects on the surface portion A_d is $g_o\sqrt{N_d}$, where g_0 indicates the mean square root of the force acting on the film due to a single impurity.

Then the force per unit area is:

$$F_d = g_0\sqrt{\frac{n_d}{A_d}} \tag{1.24}$$

with $n_d = N_d/A_d$, which is the density of defects per unit area.

As a consequence, if external forces are small, and temperature is sufficiently low, our high coverage film (suppose $\vartheta \sim 0.5$) will show a small slippage, and high temperature are necessary to make particles move from a $U(\vec{r})$ minimum to another. More precisely, if $K_BT \ll U_1 = F_dA_da$, where a is the lattice constant of the substrate (this means thermal energy is very low with respect to the barrier due to the defect), then only film islands as large as ξ^2 will move coherently [13], [1], while if $K_BT \gg U_1$ the presence of defects is not so important.

Suppose, for example, that one of the atoms represented in figure 1.5 is rigidly locked to the substrate and interacts with other atoms via the usual Lennard-Jones potential (1.21); in computer simulations, because of periodic boundary conditions, this means that infinite defects are uniformly present. If we consider the realistic condition of QCM experiments, the external force is not so high, and then defects play a vey important role.

1.4 Diffusion of nanoparticles

Up to this point we have dealt with the most simple system: atoms adsorbed on a crystalline substrate interacting via a Lennard-Jones potential. Let us now consider clusters of hundreds of atoms deposited on a flat surface. Understanding the diffusion mechanisms and the frictional properties of aggregates of atoms or molecules of nanometric size (*nanocluster*) on a surface is important for both fundamental and technological view points[14]-[18].

Recent experimental studies show unexpected results for gold cluster diffusion on graphite. The diffusion coefficient D for this system is several orders of magnitude higher than that predicted theoretically[14].

Studying cluster diffusion on a flat substrate is more complicated than adatoms because surface interaction is not punctiform for cluster. Cluster interface is formed by tens of atoms having a certain crystalline structure, also different from surface structure. Let us consider Lennard-Jones potentials for the interaction between clusters and crystalline substrates. Landman *et al.*[16] simulated gold cluster diffusion on graphite surface. They report a novel surface diffusion phenomenon, where large three-dimensional gold clusters adsorbed on a graphite surface show anomalous diffusive motion with very high rates, occurring through a collective slip-diffusion mechanism, involving long sliding trajectories. Normal diffusion is characterized by a variance of displacements $\sigma^2(t) \sim t^\gamma$ growing in the long time limit linearly with t, i.e. $\gamma = 1$, while for superdiffusion $\gamma > 1$ and long displacements, termed *Lévy flights*, occur. For gold clusters of 140 atoms with a face-centered-cubic structure and a truncated-octahedral morphology adsorbed on the basal plane of graphite, Landman simulations reveal long average displacements of $\sim 100\,\text{Å}$, with distribution of flight speeds about a mean value of $15m/s$, alternated to short Brownian motions of $\sim 2\,\text{Å}$, figure (1.7). In all these simulations temperature was fixed at $500K$. This kind of simulations was repeated by Lewis et al[17] using different potential parameters. Both works uncovered a cluster diffusion mechanism that has a very interesting nature.

Via molecular dynamic simulations Deltour *et al*[15] found a surprisingly high diffusivity when the interface of large clusters ($50 < N < 500$, with N number of atoms forming the cluster) are incommensurated with the substrate. The cluster is

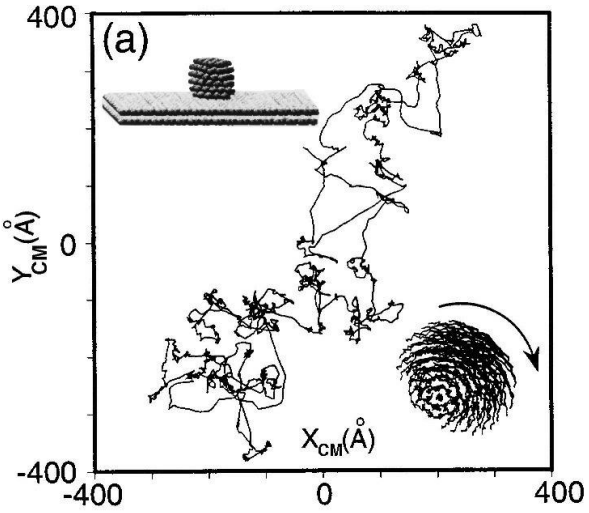

Figure 1.7: A $90ns$ (xy) trajectory of the center of mass (CM) of a Au_{140} cluster diffusing on the basal plane of graphite at $500K$ (x and y in units of Å). Insets: top left: atomic configuration of the adsorbed cluster on the surface; bottom right: a top view of a short-time trajectory of the cluster[16].

not locked by the substrate and can vibrate relatively free.

The physical interpretation is simple: cluster interface is a finite plane with a given crystalline structure while flat substrate is like an infinite surface with a different structure. The vibrations (phonons) of the substrate and the internal vibrations of the cluster both create a "random" force on the cluster center of mass (CM), which executes a Brownian motion in this weak external potential. During one such fluctuation the two crystalline surfaces in contact, that of the gold cluster and that of the graphite plane, behave as hard incommensurate sliders, and thus slip for a while essentially freely. This beacuse when the cluster is not commensurated with the substrate, the modulation of the potential felt by the center of mass is small.

This stick–slip-type dynamics still leads to an activated diffusion coefficient of the form[18]:

$$D(T) = \frac{\nu a^2}{4} \exp\left(-\frac{E_d}{k_B T}\right) \tag{1.25}$$

where a is the jump step, ν is the attempt frequency, and E_d is the energy barrier to be overcome. It has the same form predicted by the model of jump over simple monatomic steps barriers[19]: the cluster motion is ascribed to adatom evaporation and condensation at the periphery of the cluster (atoms are exchanged between the cluster and the surrounding "gas" of adatoms on the surface). Faceted clusters diffuse as facet ledges are completed or eroded. A completed ledge is the row of

atoms making up one facet, or ledge, of the cluster; a partial ledge is terminated by one or two kink. To maintain the cluser size, the cluster and adatom populations must again be in equilibrium and, additionally, the rate of ledge nucleation on a facet and the rate of facet erosion must be substantially equal.

Simulations described above give a prefactor for 1.25 of $\sim 10^{-3}\,\mathrm{cm}^2\,\mathrm{s}^{-1}$ and an effective barrier of $0,08$ eV while from experiments prefactor is $\sim 10^{3}\,\mathrm{cm}^2\,\mathrm{s}^{-1}$and effective barrier is $0,5\,\mathrm{eV}$[14]. The source of discrepancy between simulations and experiment is probably related to a large error in the adsorption energy. An experimental estimate for the adsorption energy of Au on graphite is $E_a = 0,64$ eV. Ab initio calculations suggested even larger values for the adsorption energy of about $0,9\,\mathrm{eV}$. On the other hand, the LJ model potentials imply much smaller adsorption energies, $E_a \sim 0.15\,\mathrm{eV}$. With this smaller adsorption energy, a cluster could experience a smaller effective energy barrier when trying to disentangle itself from the graphite substrate. Starting from this simple model Pisov et al[18] calculate the prefactor $D_0 = \nu a^2/4$ and the energy barrier E_d fitting experimental data of Bardotti et al[14], finding $D_0 = 10^3\,\mathrm{cm}^2\,\mathrm{s}^{-1}$ and $E_d = 0,5\,\mathrm{eV}$.

1.5 Contact mechanics

Another way to measure friction consists in sliding a probe across the surface of a counterpart and measuring the frictional force f at different applied load F_l. Atomic Force Microscope (AFM) is a suitable tool to perform tribological characterization of materials down to the nanometer scale. An AFM can simultaneously acquire topographic maps of surfaces with nanometric resolution, and friction maps operating in the so-called Friction-Force mode (FFM).

It is common to introduce a friction coefficient μ as the ratio of the tangential friction force to the normal applied load ($\mu = f/F_l$). At the macroscopic scale μ is in general a constant, but at microscopic scale μ may depend on load, thus the friction coefficient is better defined as $\mu = \frac{df}{dF_l}$. The friction force acting on the slider is the result of the collective action of frictional forces acting on smaller and smaller portions of the contacting surface.

In a tipical AFM scan it is likely to occur a single-asperity contact because of the reduced dimension of the tip. The occurrence of wear during sliding and the pollution of the tip by contaminant causes the possibility to have a multi-asperity contact. The morphology of the sample to be scanned is very important to define the contact area and the contact regime for the measurements.

A fundamental relation is the proportionality between the friction force f and the contact area A between two bodies:

$$f = \chi A \tag{1.26}$$

χ being the shear modulus, i.e. the friction force per unit area. The true contact area A is usually much smaller then the apparent (geometric) contact area. Eq. 1.26 has been verified experimentally both directly (with the Surface Force Apparatus or friction-current measurements) for single-asperity contacts and indirectly, through the validity of the contact mechanics models. The shear modulus depends in general on the number and nature of bonds forming at the interface, while the contact area depends on the mechanical properties of the interface, that is on the bulk properties of tip and sample materials.

Contact mechanics aims to provide for every contact regime the functional relation $A(N)$ between the contact area A and the load N. Once the relation $A(N)$ is established, the friction vs. load characteristics $f(N)$ for a particular system is given by Eq. 1.26.

More than 120 years ago Hertz[20] solved the perfectly elastic, non adhering case of contact between two spheres of radii R_1 and R_2 and external applied load F_l, that simulated the single-asperity contact. In the case of $R_2 \to \infty$ mimicying the contact between a sphere and a flat surface, he showed that the contact area A depends on the applied load F_l as: $A \propto F_l^{2/3}$and so $f \propto \chi F_l^{2/3}$.

Johnson-Kendall-Roberts (JKR) in 1971[21] considered the adesion work between the sphere and the substrate, due to short range interactions acting at the contact area; the contact area scale as: $A \propto F_{JKR}^{2/3}$ and consequently $f \propto \chi F_{JKR}^{2/3}$. The effect of adhesion in the contact model is to replace the external load F_l with the total load F_{JKR} that includes the sum of the external force and the adhesive force.

Considering adhesion in the contact model has a few interesting consequences. First, at zero applied load ($F_l = 0$) there is a finite contact radius and this means a finite friction force f_0. If the sphere is retracted, applying a negative load in order to overcome the attractive adhesive force, at a certain point the contact is suddenly broken. The applied force at this point is called *pull-off force* (F_{PO}). The pull-off force F_{PO} can be directly measured by AFM. We can then define an effective load F_n:

$$F_n = F_l + F_{PO} \tag{1.27}$$

In the case of non-adhering elastic and plastic multi-asperity contact, a linear dependence of friction on load F_l is expected, the so-called Amontons's law:

$$f = \mu F_l \tag{1.28}$$

because A is linearly proportional to applied load[22]. A considerable effort has been made in order to include adhesion in the models of multi-asperity elastic contact. A definite model of roughness-dependent adhesion is still lacking. The available studies on adhesive multi-asperity contacts do not provide the relation between the area of contact and the load, which would provide in turn the actual friction law through Eq. 1.26 in the case of multi-asperity adhesive contacts. If adhesion is considered

explicitly in Amontons's equations, the external load F_l must be replaced by an effective load given by Eq. 1.27. Eq. 1.28 then becomes:

$$f = \mu(F_l + F_{PO}) \cong k + \mu F_l \tag{1.29}$$

This form of the Amontons's law is also known as the Coulomb equation.

The contact mechanics of an FFM represents an intermediate case between the macro-scopic multi-asperity case and the UHV single-asperity case, in that the contacting asperities, especially in the low-load regime, can be really a few. This point makes the study of the multi-asperity adhesive regime in FFM experiments very difficult. Without a complete contact theory, one may try to use reasonable models justifying them a posteriori with the experimental observations and theoretical results in the single-asperity limit.

Chapter 2

Experimental apparatus for QCM measurements

The Quartz Crystal Microbalance (QCM) technique has been successfully applied to many research fields such as physical and chemical adsorption, analytic chemistry, biochemistry [23]. Dealing with physics, this technique has been used to study phenomena such as wetting transitions of simple molecules (H_2, He, Ne) on alkaline surfaces [24] and superfluidity of helium films on gold [25]. More recently, it has been applied to the study of nanotribology of thin films physisorbed onto metallic surfaces [26], [27], because it is possible to measure the energy dissipation due to friction of the adsorbate sliding with respect to the substrate [28],[30]; for this kind of experiments electrodes surfaces must be very clean and regular to avoid the presence of pinning centres that can strongly affect the results. Measurements must be done in Ultra High Vacuum (UHV) environment to keep clean surfaces from contaminants.

In the first part of this chapter I will show how QCM could be used as a tribological probe: the goal is not an accurate explanation of this topic (for which refers to bibliography) but an intuitive description of the main aspects in order to better understand the data analysis. In the latter part I will describe the experimental set-up mounted in the LaFSI. How said to study friction across the superconductive transition it is necessary an UHV environment together with low temperature. The home made chamber built in our lab integrates these two aspects.

2.1 QCM

The sensor used in the QCM is an AT cut quartz disk ($1cm \times 0.3mm$) schematized in figure 2.1. The two principal faces are optically polished and covered with metallic films. The piezoelectric properties of this crystal give rise to an elastic deformation when an external electric field is applied as shown in figure 2.1. In particular, being only the central part of the faces covered by the metallic films which act as electrodes,

the shear deformation does not propagate to the peripheric part of the disk[29].

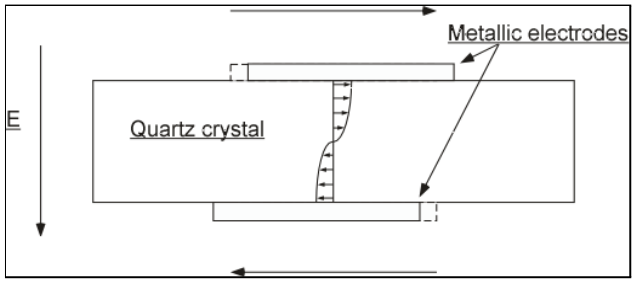

Figure 2.1: Lateral section of the quartz disc: when excited by an external electric field the principal faces move in transverse shear motion.

If we apply a sinusoidal electric field, it is possible to drive the system to one of its own resonant frequencies, typically of the order of some MHz. The amplitude of surfaces movements has been theoretically estimated[31] and experimentally measured[32] recently, ranging from a couple of Angstrom to a few nanometers depending on the voltage applied and the Q-factor of the crystal. When this system is driven to one of its normal modes we can measure the frequency shift and the Q-value variation due to the presence of adsorbed molecules.

2.2 The acoustics of the QCM

The AT crystal has a natural mechanical resonance when the plate thickness h is half of the transverse mode wavelength λ, or an odd multiple of $\lambda/2$, e.g. $h = n\lambda/2$, where n is called the overtone number ($n = 1$ is the fundamental mode, $n = 3$ is the third overtone...). At room temperature, the resonance frequency of such a plate oscillating in vacuum is related to its thickness h by the simple relation:

$$f_{0,n} = \frac{1,75n}{h} - C \tag{2.1}$$

where $f_{0,n}$ is measured in MHz, h in mm and C is a small correction factor which increases with electrode thickness. (Typical values of $f_{0,1}$ for AT plates employed as QCM sensors lie in the range 1-10MHz).

At a certain frequency f^*, its behavior in vacuum can be described by a complex acoustical impedance:

$$Z_0 = R_0 - jX_0 = R_0 - j\pi nAZ_q\frac{f^* - f_{0,n}}{f_{0,n}} \tag{2.2}$$

where A is the area of one electrode, $Z_q = 8.862 \times 10^5\ g/cm^2\ sec$ is the quartz acoustic impedance and the dissipative term R_0 , which accounts for all the losses in the plate, is related to the quality factor Q_0 via

$$\frac{1}{Q_0} = \frac{2R_0}{\mu n A Z_q} \tag{2.3}$$

When the quartz plate is immersed in a fluid, its impedance will change because of the adsorption of a film onto the quartz surfaces and of the viscous coupling with the surrounding vapor. The global contribution per unit area can be expressed in terms of a complex impedance $R_{sfv} - jX_{sfv}$, in series with Z_0 . If both faces of the quartz plate are exposed to the fluid, the total dissipative and inertial terms become, respectively, $R_0 + 2AR_{sfv}$ and $X_0 + 2AX_{sfv}$. The quality factor will then decrease by an amount $\Delta\frac{1}{Q}$ equal to:

$$\Delta\frac{1}{Q} \equiv \frac{1}{Q} - \frac{1}{Q_0} = \frac{4R_{sfv}}{\pi n Z_q} \tag{2.4}$$

and the resonance frequency f will also be diminished by:

$$\Delta f \equiv f - f_{0,n} = -sX_{sfv}\frac{f_{0,n}}{\pi n Z_q} \tag{2.5}$$

The exact shifts will obviously depend on the explicit forms of R_{sfv} and X_{sfv}. In order to determine them, we have applied the linearized Navier-Stokes equation to the combined system quartz crystal-adsorbed film-bulk vapor. Let d be the thickness of the adsorbed film and ρ_f and η_f its bulk mass density and viscosity, respectively, while η_v and ρ_v represent the viscosity and the density of the bulk vapor. If we assume, as customary, that the transverse velocity field depends only on the vertical distance z from the electrode surface, the general stationary solutions to the Navier-Stokes equations in the vapor and film regions are determined apart from four integration constants.

These can be univocally determined by imposing the following boundary conditions on the velocity fields v_f and v_v:

a. $v_v = 0$ very far from the film;

b. $v_v = v_f$ at the film-vapor interface (i.e. no slippage at this boundary);

c. at this interface, the force exerted by the vapor on the film must be equal to that caused by the film on the vapor, that is

$$\eta_v \left(\frac{dv_v}{dz}\right)_{z=0} = -\eta_f \left(\frac{dv_f}{dz}\right)_{z=d}$$

d. we assume, in general, that there may be slippage at the solid-film interface.

Because of this, there will be a frictional force F_{sf} at this boundary. As the last condition, we then impose that the force F_{sf} must be equal and opposite to that due to the film, that is: $F_{sf} = +\eta_f \left(\frac{dv_f}{dz}\right)_{z=0}$. Finally, we make the plausible assumption that F_{sf} depend linearly on the relative velocity between the quartz plate and the film:

$$F_{sf} = -\eta_2 \left[v_0 - v_f(0)\right]$$

where η_2 is called coefficient of sliding friction or interfacial viscosity, v_0 is the velocity of the electrode and $v_f(0)$ that of the film at the electrode surface. This condition is consistent with recent QCM studies of the velocity dependence of η_2[**?**]. If there is no slippage at the solid-fluid interface, $\eta_2 = \infty$. The opposite limit, $\eta_2 = 0$, corresponds instead to a superfluid whose motion is totally decoupled from that of the oscillating substrate.

By carrying out the necessary algebra, one finds that the reciprocal of Z_{sfv} can be easily rewritten as:

$$\frac{1}{Z_{sfv}} = \frac{1}{Z_v + Z_{fd}} + \frac{1}{\eta_2} \tag{2.6}$$

which says that the total acoustic impedance Z_{sfv} of the combined system substrate-film-vapor can be considered as the parallel between the series of the vapor impedance, Z_v , and that of the film Z_{fd} , and the impedance η_2 due to the slippage of the film at the solid boundary.

The formula 2.6 means that it is possible, at least in principle, to measure the friction force of a film adsorbed on a solid surface with a quartz microbalance. In nanotribology one is interested in studying the friction of an adsorbed monolayer. This implies that the acoustic impedance of the film can be simplified as

$$Z_{fd} \simeq -j\omega\rho_f d \tag{2.7}$$

where $\omega = 2\pi f$.

If we solve the equation 2.6 in terms of R_{sfv} and X_{sfv} we get:

$$\frac{X_{sfv}}{R_{sfv}^2 + X_{sfv}^2} = \frac{\omega\rho_f d + X_v}{R_v^2 + (\omega\rho_f d + X_v)^2} \tag{2.8}$$

and

$$\frac{R_{sfv}}{R_{sfv}^2 + X_{sfv}^2} = \frac{R_v}{R_v^2 + (\omega\rho_f d + X_v)^2} + \frac{1}{\eta_2} \tag{2.9}$$

The first equation yields the film thickness d as

$$d = \frac{1}{2\omega\rho_f}\left[R_{sfv}^2 + X_{sfv}^2 + \sqrt{\left(R_{sfv}^2 + X_{sfv}^2\right)^2 - 4R_v^2 X_{sfv}^2}\right] - \frac{X_v}{\omega\rho_f} \tag{2.10}$$

which can be substituted in the second one in order to calculate the interfacial viscosity η_2.

The coefficient η_2 quantifies the viscous interfacial friction, but usually in nanotribology another parameter is more often used. This is the so called slipping time τ_s which represents the time required for the adsorbed film speed to decay to $\frac{1}{e}$ of its initial value after that the oscillating substrate has been put to rest in the absence of a bulk vapor, can be calculated from the ratio:

$$\tau_s = \frac{\rho_f d}{\eta_2} \tag{2.11}$$

and replacing η_2 and d from 2.9 and 2.10:

$$\tau_s = -\frac{\Delta\left(\frac{1}{Q}\right)}{4\pi\Delta f} \tag{2.12}$$

Let us see a simple justification of this interpretation. Suppose the film, having mass m, is moving with velocity v_0 along the surface which does not move. If there is no vapour, the only force acting on the atom is the frictional one, and therefore, if we express F_{sf} in terms of slipping time, the motion equation is:

$$m\frac{\partial v}{\partial t} = F_{sf} = -m\frac{v}{\tau_s}$$

whose solution, taken into account the boundary condition, is: $v(t) = v_0 e^{-t/\tau_s}$[29].

2.3 Electric behaviour of the QCM

From an electric point of view the quartz crystal, when driven near one of its own resonant frequencies, can be viewed as a LCR series circuit with very high quality factor ($Q_s \approx 10^5$); it then presents a maximum in the transfer function in correspondence to its own resonance frequency, which we call "series" resonance ω_s. Our direct measurements try to determine its value and the corresponding output voltage. A small correction is necessary if we consider that another capacity is present in parallel with them, due to the presence of the electrodes. We call it C_0 (a couple of pF), and draw the system as in figure 2.2. The presence of C_0 gives rise to a second resonant frequency, which we call "parallel" (ω_p), characterized by a minimum in the output signal. Since $\omega_s - \omega_p \approx 1 \div 2kHz$ it is not always simple to find the first one, because the curve is not a simple Lorentzian as it would be in the case $C_0 = 0$. In this chapter we will see how to determine ω_s starting from the directly measured frequency value of the transfer function maximum.

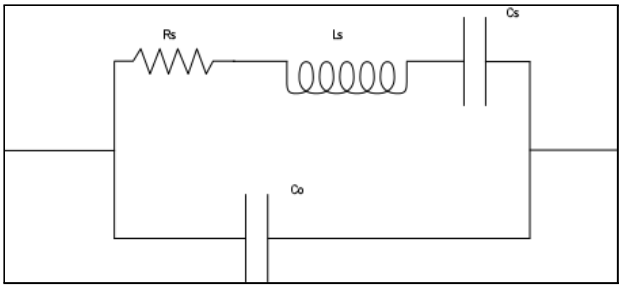

Figure 2.2: Electric analogue of the quartz disc.

Here, we call L_s, C_s, and R_s respectively the inductive, capacitive and resistive components of the LCR serie, and C_0 the parallel capacity; at resonance, the total impedance is resistive, with R_s typically of the order of 50Ω.

We define:

$$\text{Resonance frequency "series"} = \omega_s = \frac{1}{\sqrt{L_s C_s}}$$
$$\text{Resonance frequency "parallel"} = \omega_p = \frac{1}{\sqrt{L_s C_p}}$$
$$\text{with } \frac{1}{C_p} = \frac{1}{C_s} + \frac{1}{C_0}$$
$$\text{Quality factor} = Q_s = \frac{1}{R_s}\sqrt{\frac{L_s}{C_s}}$$
$$\text{Antiresonance quality factor} = Q_d = \frac{\omega_s}{\omega_p - \omega_s}$$

This last parameter quantifies the effect of the second resonance, which can be very close to the first one, causing asymmetries in the resonance curve. Usually, when the quality factor decreases, for example when the crystal is driven to higher overtones (typically 3^{rd} or 5^{th}) ω_p tends to become very close to ω_s: this effect can be drastically reduced using quarzes with [33]:

$$\frac{\omega_p}{\omega_s} = \sqrt{1 + \frac{C_s}{C_0}} \geqslant 1.005$$

because in this case the distance between the two resonances is not so sensitive to Q changes; for example suppose we are working with a crystal having a fundamental mode around $5MHz$ and whose ratio $\frac{\omega_p}{\omega_s} = 1.0005$. If the quality factor changes from 40000 to 1000, then ω_s has a shift of $770Hz$, but the same variation of Q causes a change of $2.5Hz$ if $\frac{\omega_p}{\omega_s} = 1.005$ [33]. Since the maximum in the resonance curve we measure is not the ω_s we are searching for, we need to find the right correction to determine it.

If the system is in stationary sinusoidal regime, the electric impedance across the quartz is, expressing it as a function of ω_s, ω_p, Q_s e Q_d:

$$Z_{AB} = \frac{\omega_s R_s}{j\omega} \frac{Q_s\left(1-\frac{\omega^2}{\omega_s^2}\right)+j\frac{\omega}{\omega_s}}{1+\frac{\omega_s}{\left(\omega_p^2-\omega_s^2\right)}\left(1-\frac{\omega^2}{\omega_s^2}\right)+j\frac{1}{Q_s}\frac{\omega}{\omega_s}\frac{\omega_s^2}{\left(\omega_p^2-\omega_s^2\right)}}$$

Now we make the assumption that $\omega \approx \omega_s \approx \omega_p$, because we are working in resonance conditions and experimentally we verify that $\frac{\omega_p-\omega_s}{\omega_s} \lesssim 10^{-3}$. Calling $x = \left(1-\frac{\omega}{\omega_s}\right)$, we find:

$$Z_{AB} = R_s \frac{1-2jQ_s x}{1+Q_d x + j\frac{Q_d}{2Q_s}} \tag{2.13}$$

If we search for the minimum of $|Z_{AB}|^2$ with respect to x and return to the variable ω, we arrive to the expression:

$$\omega_s = \frac{\omega}{1-\frac{a}{Q_d}} \tag{2.14}$$

where $a = \frac{1}{2}\left(\sqrt{1+\frac{Q_d^2}{Q_s^2}}-1\right)$.

In corriespondence to ω we have the minimum value of $|Z_{AB}|$, which is the minimum electric impedance of the quartz:

$$|Z_{AB}| = \frac{R_s}{(a+1)} \tag{2.15}$$

As expected, $|Z_{AB}| \to R_s$ as $a \to 0$, which means $\frac{Q_d}{Q_s} \to 0$.

From equation (2.13) we directly derive the expression:

$$y = \frac{1}{R_s^2} \frac{\left((Q_d x+1)^2 + (\frac{Q_d}{2Q_s})^2\right)}{1+(2Q_s x)^2} \tag{2.16}$$

in which y is the related to the inverse of $|Z_{AB}|^2$. This function is experimentally used to calculate the Q-factor from frequency and voltage data.

In the limit of very low vapor density, this approach yields identical results with the formulas introduced heuristically by other authors[28], according to which the vapor impedance is in series with the parallel of the film impedance and the interfacial viscosity.

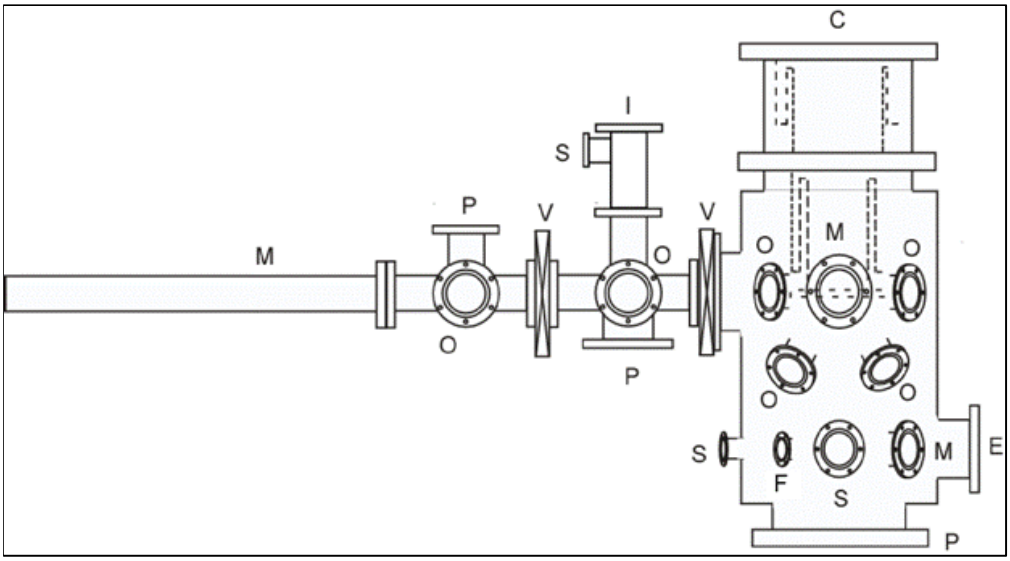

Figure 2.3: Schematic drawing of the UHV system. The jacket is indicated using dash lines. The flanges utilization is described using symbols: M manipulators, P pumps, C cooler, O optic flanges, V valves, S pressure sensors, E electrical feedthrougs, F messier coils feedthrough[34].

2.4 UHV system

Figure 2.3[34] shows a simple scheme of the UHV system: it is made up of three chambers which communicate through UHV valves.

The main one contains the sample holder and the cryogenic inserts, while two other smaller chambers (UHV suitcase and fast entry lock) are used to charge new samples without breaking the ultra high vacuum in the principal section of the apparatus. Moreover, the UHV suitcase can be detached from the rest of the apparatus and used to bring the sample to other UHV systems. In the fast entry lock, instead, is mounted an ion gun to sputter and clean the sample surface.

2.4.1 Main chamber

The main chamber is schematically drawn in the right part of figure 2.3. It is completely made up of stainless steel and many flanges of different size are present on it. On the top flange a jacket is inserted to guarantee the possibility to decouple or remove the cooling unit without breaking the UHV in the chamber.

The main group of flanges points to the centre of the chamber, where the sample holder is located. In particular, two manipulators are used (see figure) to change the sample without opening any flange. This is possible using a wobble stick, a sort of clamp able to freely rotate around its principal axis, and to move about 10°

around it. Thank to this device it is possible to pick up the sample and to put it on a translator. The latter one is a magnetically coupled manipulator which moves the sample to the other chambers.

Four optical flanges are used to directly see the sample, in order to correctly move the manipulators. Just near the valve separating the main chamber from the fast entry lock there is a sapphire valve connected to the gas system, used to dose with high precision the selected gas in the sample direction. To better focus the particles flux, a stainless steel small tube ($4mm$ diameter) is used. In this way the admitted gas exits from the gas system just a few centimeters from the adsorption surface of our QCM.

The electrical signals which are necessary to heat the sample, to drive it to resonance (and to detect its own resonance parameters) and to measure the temperature arrive to an internal cavity through a stainless steel tube. This internal cavity is completely sealed with respect to the UHV ambient and is maintained in low vacuum using a rotary pump. It houses a calibrated Germanium diode and a heater. Their good thermal coupling to the copper body is guaranteed by the use of epoxy.

Two other flanges are used for electrical feedthroughs connecting the two coils used to detect the superconducting transition. They are separated from other cables principally because the superconductive transition detection technique works properly only if the mutual inductance between the pick ups is due to the coils themselves and not to their own cables. So locating the latter close together in the low vacuum tube would compromise the correct detection of the transition.

In the lowest part of the main chamber there are many sensors; pressure is detected by a Baratron capacitive transducer and an ion-gauge. The first one is used for pressures comprised between atmosphere and 10^{-2} Torr. The second one is used in High and ultra-high vacuum conditions and works from 10^{-4} to $10^{-11}Torr$. A residual gas analyzer (RGA) is connected to another flange, and permits a precise detection of the partial pressure of single gases. In this way we can use it both as leak detector and also to understand what may cause an insufficient vacuum level in the chamber.

Finally, a manual valve is located in the lowest part of the system to vent the system if necessary and a very large flange at the bottom of the cylinder (about $25cm$ diameter) is used to open the chamber and to work in it.

2.4.2 Jacket

One of the main problems to solve in order to work in UHV at low temperature with a cryocooler is due to the necessity to perform high temperature bakings to reach low pressures ($10^{-11}Torr$) without damaging the cryocooler head, not heatable at more than $70°C$ because of the presence of plastic components.

The problem has been solved using a non conventional jacket. This device is

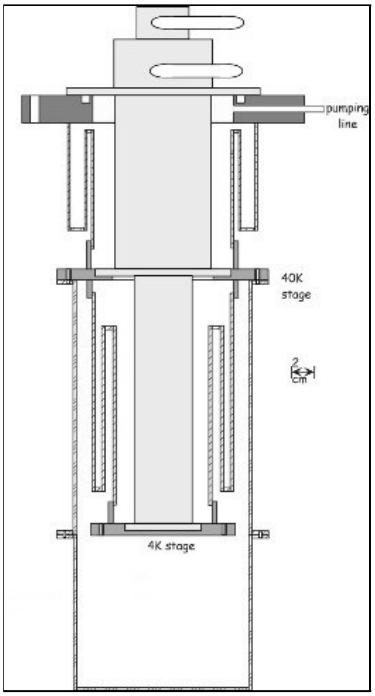

Figure 2.4: Schematic rappresentation of the jacket: to note the two onion-like structures that screen the stages at 40k and 4K. In light gray is pictured the cryocooler head.

inserted in the flange occuping the top side of the main chamber, and appears as shown in figure 2.4. The main idea is to maximize the geometrical path from points at different temperature, in order to decouple from each other. For this reason an onion-like structure of concentric stainless steel cylinders connects the external flange, at about $300K$, to the $40K$ stade of the cryocooler. The low conductivity of stainless steel, together with the small thickness of the tubes, guarantees a small heat flow through the jacket walls. Moreover, the self-shielding geometrical shape greatly reduces the radiative thermal exchange. In correspondence to the first stage of the cryocooler, at about $40K$, our jacket presents a copper flange, whose contact with the cryocooler itself is guaranteed by an indium foil pressed at the contact interface. The same system we just described is used to connect the $40K$ stage to the $4K$ head of the cryocooler. Again three concentric stainless steel tubes thermally decouple the two stages, while the $4K$ copper flange of the jacket is pressed together with the cryocooler head using indium to optimize the conduction. This device completely seals off the UHV ambient from the low-vacuum room, evacuated by a rotary pump, where the cryocooler head is usually inserted. The sample-holder is crewed to the $4K$ copper flange of the jacket.

2.4.3 Fast entry lock

The main body of this device is a six-ways cross flanged connected to the main chamber described above and to the suitcase through two UHV valves (see fig 2.3). The translator located in the suitcase allows a very rapid change of the sample using a fast-open optical port, sealed by a viton o-ring rather than copper one which can be not used more than two or three times. The largest flanges of this chamber are used for the turbomolecular pump allowing a very rapid evacuation of the very small volume and for an ion-gun which is necessary to clean the sample surface just before every data acquisition series. An ion gauge is used to detect the vacuum level indipendently from the main chamber.

2.4.4 Cryocooler

We mostly work around the lead superconductive transition temperature ($7.2K$) and then we need a system that cool our samples at temperatures lower than this one. We use a cryocooler, which in figure 2.4 is schematically drawn when installed into the jacket. It is a two-stages Sumitomo cryocooler working with helium whose cooling power is $1.5W$ when working at $4.2K$, which is the lowest temperature reached by the cold finger when totally screened by the $40K$ stage and without any thermal charge. Of course in our setup this is not the case, because the thermal mass is very large, the $40K$ screen doesn't cover all the solid angle since some windows are necessary to let the passage of manipulators, and also because many thermal short-circuits are present in the system. In fact the sample holder is connected through a stainless steel tube to the external wall of the chamber ($300K$) in order to seal the electric wires from the UHV environment. Moreover the structure of the jacket directly short circuits the different cooling stages ($40K - 4K$) and the intermediate stage to the external temperature ($300K - 40K$). Anyway, thanks to the self-shielding onion structure of the jacket the system reaches a sufficiently low temperature ($5.5K$) in a reasonable amount of time. The cryocooler works performing closed cycles of helium. It is first compressed and cooled using cold water, then expanded inside the head in a process involving a positive work made from the gas on the system. During this thermodynamical transformation helium cools off, so cooling the finger. The cryocooler works in two stages, and this means that a first cycle is used to pre-cool the helium used in a second cycle, in order to reach lower temperatures.

A rotative pump is used to evacuate the jacket down to $10^{-3}Torr$ and indium foils are used in order to guarantee low thermal impedances in the crucial contact between surfaces.

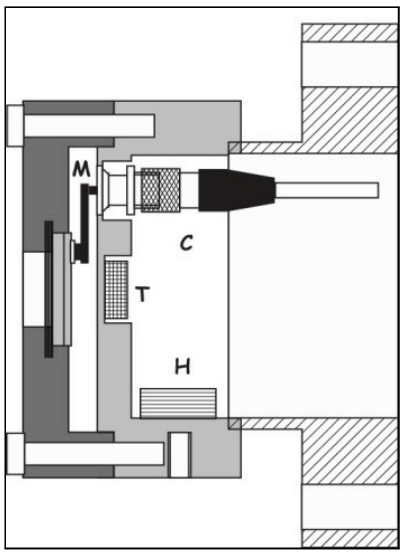

Figure 2.5: Sample holder scheme: M metallic bridge, C coassial cable, T thermometer and H heater. The last three are into the stailess steel tube maintained in low vacuum and separated from main chamber.

2.5 The sample holder

The sample holder is schematically drawn in figure 2.5. It is almost completely made up of copper in order to minimize thermal gradients and to guarantee a good thermal link between the sample and the cold head. For the same reason, every interface between different parts and between the cold head and the sample holder itself is filled with thin indium foils.

Its position allows us to change the sample by just using the wobble stick, and to carry it out from the principal chamber through the magnetically coupled translator. When the quartz is inserted, it is almost completely shielded from the room temperature radiation by a $40K$ Aluminum screen, and by the sample holder body at $4K$. Moreover, to guarantee a good metal-metal thermal coupling four small spheres, pushed by springs, have the function of pressing the sample on the internal wall of the sample holder; in this way also a good electrical contact is guaranteed.

The electrical signal arrives to one of the quartz electrodes through a metallic bridge, while the other one is directly connected to the electrical mass. Both this electrical connection and the spheres described above are specifically designed to permit an easy insertion of the sample with the wobble stick. To better screen the sample from thermal radiation at $300K$ arriving from the wobble stick side a rotatable copper protection anchored to the $4K$ can be moved to cover all the solid angle in this direction.

Just a few millimeters away from the QCM electrodes, two Meissner coils (pick-

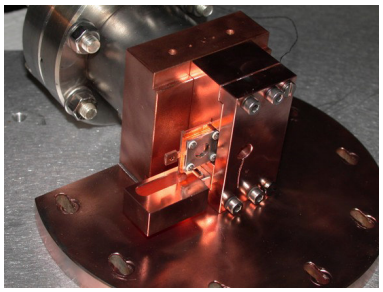

Figure 2.6: Picture of the sample holder. It is possible to observe the rotable copper window, the stainless steel cilinder that contain electrical wires and how sample can be inserted and removed.

ups) are locked into two cilindrical holes. They are made up of stainless steel (about $4mm$ internal diameter and 30 turns), covered with Kapton, completely compatible with UHV even at baking temperature ($200K$). When one of these coils is excited by using an high frequency current ($50KHz$, $\approx 10^{-3}A$), another current is generated in the other one because of their mutual inductance. Once the lead electrode of the quartz becomes superconductive, it completely screens out the magnetic flux, and this can be detected by analyzing the intensity of the signal in the second coil which drastically decreases.

The sample holder is soldered to a stainless steel flange, which is close together with another identical flange; from here a flexible tube exits from the UHV chamber. This part contains the electrical wires that bring signals to QCM, resistive and diode thermometers and a heater. It is also completely sealed from the UHV volume.

2.5.1 Mechanical mounting of the crystal

The quartz crystals are usually mounted on a small clip. The signal is transmitted to the two electrodes through the clip itself, which also guarantees mechanical stability. In most cases the crystal is glued to the clip using some kind of conductive epoxy. Of course this configuration is not at all compatible with UHV standards because of the presence of epoxy, and is not practical if we need to manipulate our samples in vacuum by using wobble-sticks and translators. For these reasons we designed a new set-up for the quartz mounting. The schematical drawing and the photo of this device are shown in figures 2.7. It consists of a copper plate, which perfectly matches with the rectangular receptacle in the sample holder, with a small appendix compatible with the Omicron-standard, used to manipulate it with wobble sticks. In fact the terminal part of the manipulator is expressely shaped to match with it.

The central part of the plate has a round cavity to house the QCM and a smaller hole. This allows surface deposition and every surface analysis through AFM/STM in Genova labs without keeping off the crystal from its support.

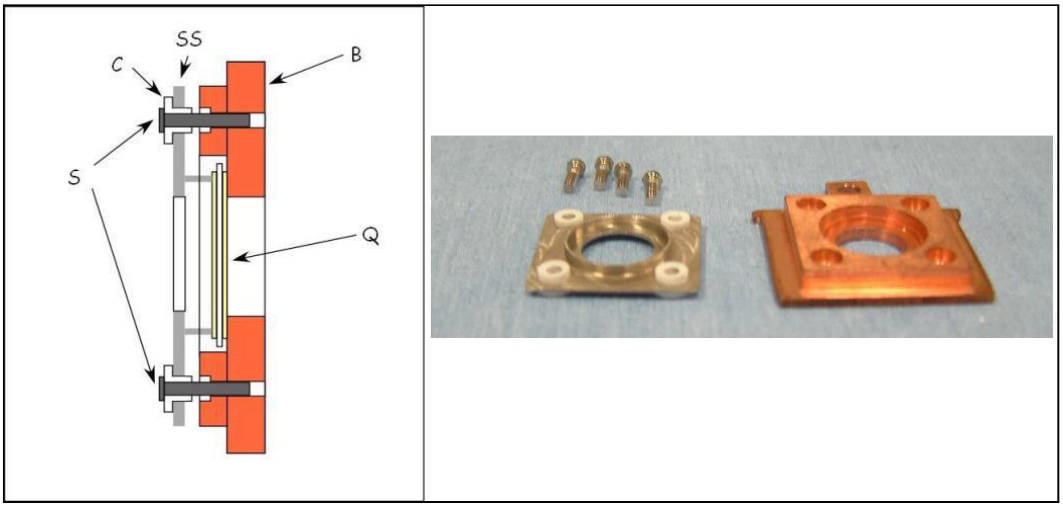

Figure 2.7: Left: simplified scheme of the QCM mounting set-up: Q quartz, B copper base, SS stainless steel cover, C ceramic sleeves, S screws. Right: picture of the QCM mounting.

On the other side of the sample, a thin ($0.2mm$) stainless steel plate is fixed to maintain the quartz in its position. It has a round ring of the same thickness with a diameter smaller than that of the QCM that directly contacts the quartz. This guarantees a good electrical and thermal contact and an excellent Q-factor. Like the other plate, a round hole is present for the same reasons described above. The two metallic plates do not touch each other, since both of them electrically connect one of the electrodes to the contact located on the sample holder. In fact, the copper plate is in contact with the body of the sample holder (electrical mass), while the stainless steel one touches the small elastic contact we described in the chapter above. The two parts are kept together by four small screws ($M1.2$) electrically insulated by using ceramic sleeves.

This set-up has been tested and we found that a very good mechanical stability is guaranteed, together with an high Q-factor (10^5, comparable with the ones reached using the standard mounting) and a perfect electrical contact despite of the absence of any glue.

2.6 Gas system

The system used to admit the selected gas in the chamber in order to condensate it on the sample surface is drawn in figure 2.8. It is very simple, with four different gas cylinders connected to the main capillary. Every part of this circuit can be isolated from the other using manual valves, while a very precise sapphire valve is mounted just before the uhv ambient. In this way we are able to admit very small quantities

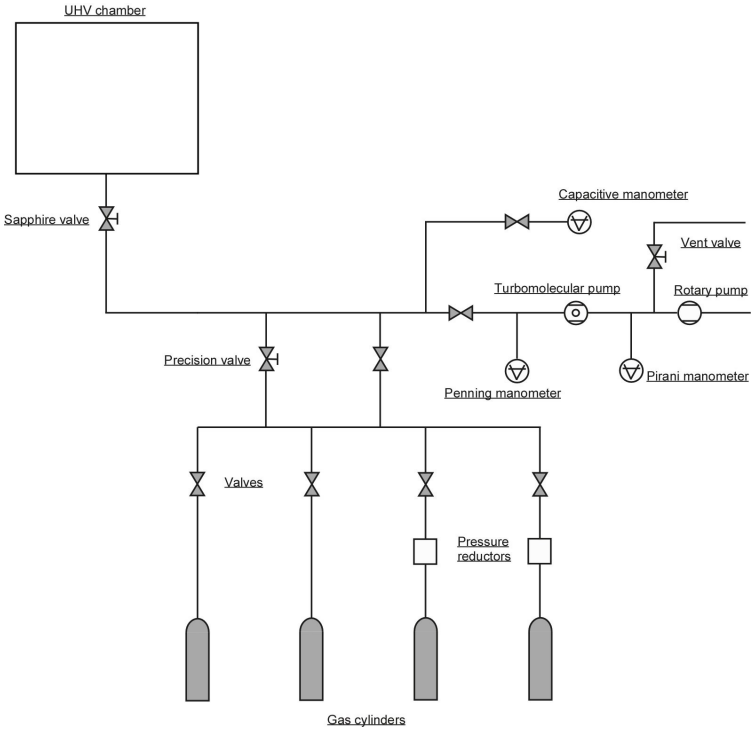

Figure 2.8: Scheme of the gas system.

of gas in our chamber, and to perfectly control the deposition on the sample surface with a resolution better than 0.1 monolayer. A capacitive manometer is used to measure the pressure just before the sapphire valve, and acting both on the valve opening and on the pressure in this region we can change the deposition rate. To rapidly evacuate the capillary circuit from any gas, a rotary and a turbomolecular pumps connected in serie are used. This system has been baked out at about 200°C with some heat guns and has been pumped by the turbomolecular pump for many months.

2.7 QCM electronics

The quartz disk is excited by an external electric field obtained by applying a sinusoidally variable voltage to the quartz electrodes. A manual search of the resonant frequency is neither precise nor rapid, so it is necessary to use a device able to automatically measure the resonant frequency.

We obtained an excellent stability of the signal by using a circuit which is based on the frequency modulation technique [35], [33]. A simple scheme is plotted in figure 2.9.

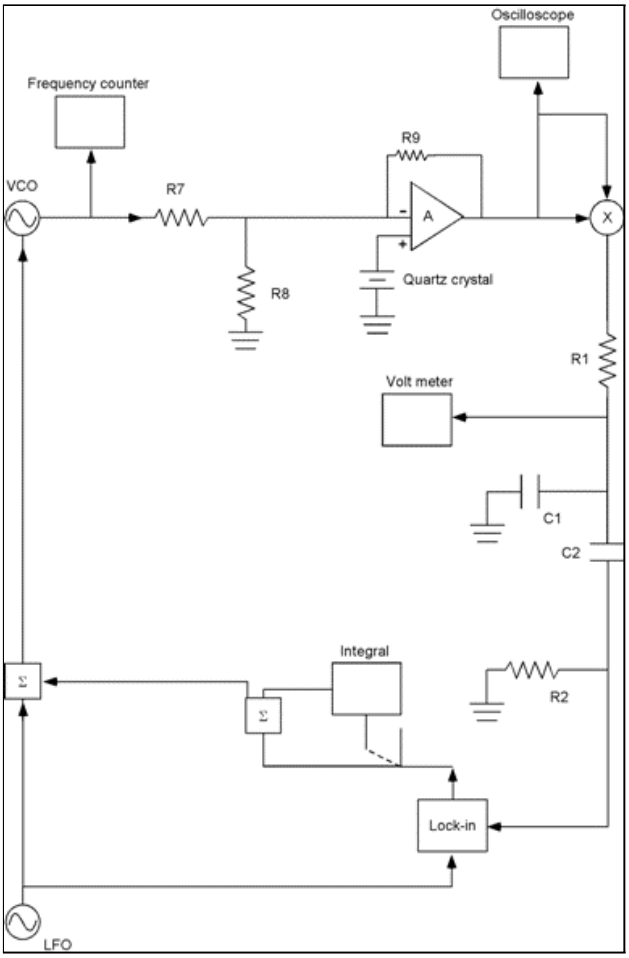

Figure 2.9: Scheme of the circuit that drive QCM to its mechanical resonance.

The radiofrequency signal is guaranteed by a RF generator ($HP8648B$, $f_{por} \approx 5MHz$), and a low frequency signal is added (LFO, $\Delta f_m = 30Hz$) in order to modulate it. Working at very low modulation frequencies makes errors due to phase shifts induced by the circuit negligible. The total signal can be written as:

$$f(t) = f_{por} + \Delta f_m \ (sin(2\pi f_{\mathrm{mod}} t) + KV_{lock-in} \tag{2.17}$$

where together with the carrier frequency f_{por} and the modulation Δf_m we introduced a third term proportional to the output tension of the lock-in $V_{lock-in}$, whose meaning will be clear very soon.

This signal reaches the quartz and then is amplified (A), squared using a multiplier (X), and finally filtered to keep only the DC component. This process is

necessary to obtain a signal easy to measure with high precision; in fact it is not possible to measure with high accuracy voltages at frequencies of the order of MHz.

Two filters (R1-C1 and C2-R2) are necessary to give to the PSD a rectified signal (whose frequency is the modulation one f_{mod}) so that the latter, driven by the LFO, gives as output a voltage proportional to the derivative (with respect to the frequency) of the input.

To quantify what we just said, if in the PSD the input signal is:

$$V(f) \approx A(f_{por} + KV_{lock-in}) + \frac{\partial A(f_{por} + KV_{lock-in})}{\partial f} \Delta f_m \sin(2\pi f_{\mathrm{mod}} t) \tag{2.18}$$

then the output is proportional to the derivative, with a multiplicative factor λ:

$$V^{out}_{lock-in} = \lambda \frac{\partial V(f)}{\partial f} \tag{2.19}$$

Another device adds to the signal 2.19 its own integral function in order to find the real resonance with higher precision in a reasonable time:

$$V_{lock-in} = \alpha V^{out}_{lock-in} + \beta \int V^{out}_{lock-in} dt \tag{2.20}$$

In fact if the carrier frequency is different from the resonance one (and this is almost always true), this system tends to supply the difference, but if the gain of the feedback is not infinite the exact resonant frequency is never reached. This problem is overcome by introducing the last term in equation 2.20, since the integral tends to diverge with time (so simulating an infinite gain) until the frequency is equal to the resonant one.

At last the loop ends with the result that the signal provided to the quartz is given by 2.17, and now the meaning of the last term $V_{lock-in}$ is clear. When the system reaches the equilibrium regime, the QCM works at the resonant frequency $f_{ris} = f_{por} + kV_{lock-in}$, which can be read by using a frequency counter with the resolution of $0.1Hz$. In our case this precision is sufficient, since the complete adsorption of one layer of the different gases used gives rise to a frequency shift in the order of a few Hz working at a resonant frequency of about $5MHz$ given by:

$$-\Delta f = \frac{4}{nZ_q} \frac{m}{A} f^2_{ris} \tag{2.21}$$

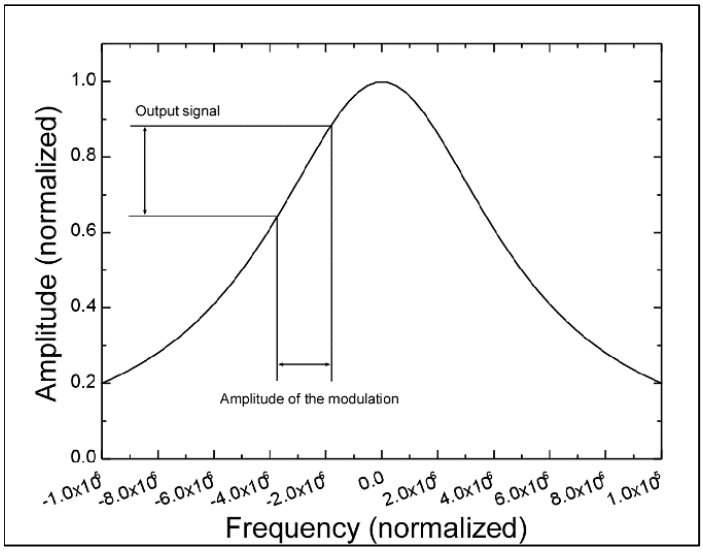

Figure 2.10: Response function of the quartz: modulation gives rise to a signal whose phase depends on the sign of the difference between actual frequency and resonance one.

where $\frac{m}{A}$ indicates the two-dimensional adsorbate density and can be found in literature. At the same time, the output voltage of the resonator is measured using a multimeter just before the lock-in.

Now let us see in a more qualitative way what happens; figure 2.10 represents the resonance of the quartz crystal. Since a modulation is present, the output voltage varies sinusoidally at the frequency of about $30Hz$; as we learn from the figure, this signal shifts its phase by π if the actual frequency moves from above to below the resonant one. The lock-in amplifier, comparing it to the LFO reference signal gives a positive or negative voltage as feedback in order to reach the correct frequency.

Chapter 3

Microfabrication

Microfabrication involves the realizzation of micrometric size structures. It is an indispensable contributor for modern technology and science: it supports information technology through its role in microelectronics and optoelectronics for which small size is correlated with cheaper, high performance and low power. The most powerful technique is *photolithography*, and essentially all integrated circuits are fabricated using this technology. Despite the industrial role covered by this technique, it is not the best to pattern plastic materials. Very recently a most flexible and very cheap technology has been developed to produce micro and nano structures.

Soft lithography represents a non-photolithographic strategy based on the elastic properties of soft materials (polymers and plastic) for carrying out micro- and nanofabrication. It provides a convenient, effective, and low-cost method for the formation and manufacturing of micro- and nanostructures. In soft lithography, an elastomeric stamp with patterned relief structures on its surface is used to generate patterns and structures with feature sizes ranging from $100nm$ to $100\mu m$.

In the first section of this chapter I will describe the photolithographic steps we used to produce micropatterned silicon masters. The other sections offer a brief general overview of the two soft-lithographic tecnique involved in this thesis work.

3.1 Photolithography

In the past few decades, photolithography has been the best technique in microfabrication [36]. For example, all the integrated circuits in microelectronics are essentially realized with this technique. Silicon masters employed in this work have been carried out with photolithography.

For our purpose, we employed silicon wafers (100) producted by SILTRONIX. The principal lithographic steps we used are:

1. Sample cleaning;

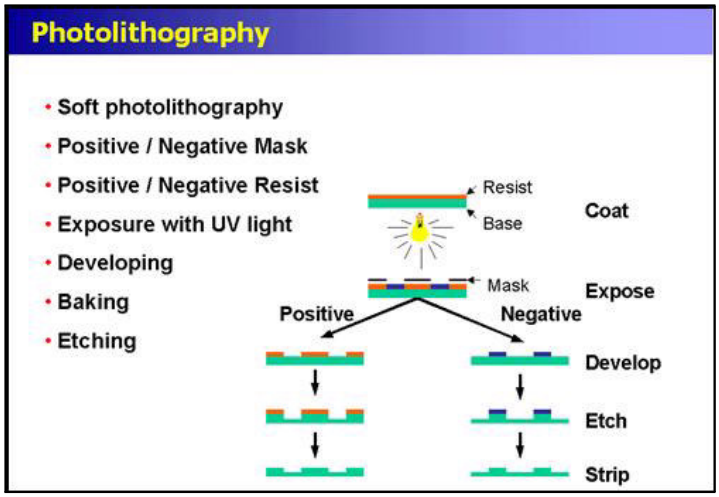

Figure 3.1: Positive and negative resist use in photolithographic processes.

2. Chrome deposition;
3. Photoresist deposition;
4. UV exposure;
5. Photoresist development;
6. Chrome wet etching;
7. Silicon dry etching.

Lithographic processes require high degrees of sample cleanness to avoid poor and inadequate results. Generally, they are done in a *clean room*, an area in wich environmental parameters like suspended particles, pressure, humidity, vibrations and absence of UV light are fixed and monitored. Silicon surfaces are cleaned with the so called *Piranha solution*, a mix of *Sulfuric acid* (H_2SO_4) *96%* and *Hidrogen Peroxide* (H_2O_2) *33%* in a ratio of 7:3 V/V. Samples are immersed in the solution and heated at temperature of $90°C$ for 30-40 minutes. This process not only oxidizes all organic contaminants possibly present on the surface but also produces a thin silicon oxide layer; if a silicon chemical etching is necessary this layer must be removed. It can be done by diping samples in a *1%* in volume water solution of *Hidrofluoridic Acid* (HF) for brief time.

The two dimensional picture one wants to transfer on silicon is contained in a mask, that in our case was a thin chromium layer deposited on glass or quartz. Chromium absorbs UV light while glass and quartz are transparent. This allow to reproduce the original picture on a *photo-resist* layer. Photoresist is a photosensible

polymer that modifies its chemical structure when irradiated with UV light. It is essentially made of a polymer, its solvent and a catalyst. The resist named *positive* when irradiated with UV light breaks polymer chains bringing a higher solubility of the broken chains. The most used one component photoresist is the *polimethilmetacrilate* ($PMMA$). It is characterized by a good resistance in acid and basic ambient and to oxidant attack.

Before photoresist deposition, a thin chromium layer of $\sim 100nm$ is evaporated on the clean Si surface. Photoresist layer is created via spin coating: a few drops of it are deposited on the surface and the sample is spinned at ≈ 3000 rpm. Final treatment is to heat photoresist at temperatures from 110° to 150°C for 1-2 minutes (*soft bake*). This is necessary to remove solvent traces: they can cause film stress and non-homogeneity and a bad adhesion between photoresist and chrome layers that could compromise development.

The quartz mask is put in contact with the resist layer below a Mercury Lamp that generates UV radiation. UV light is collimated by lenses. Time exposure ranges from a few seconds to some minutes and depends on, for example, resist layer thickness, soft-baking time, light intensity and pattern geometry. For the sake of explanation, we can say that exposure time increases with:

- increasing resist thickness;
- increasing soft-baking time;
- decreasing UV radiation lamp intensity.

With a development solution it is possible to remove the irradiated part of the resist layer, creating a pattern identical to that of the quartz mask. This resist mask is heated at 140°C for 1 minute to improve resist adhesion. By a solution composed of *Cerium Ammonium Nitrate* ($Ce(NH_4)_2(NO_3)_6$), *Acetic acid (glacial)* (CH_3COOH) and *Deionized Water* , called *Chrome Etch*, Chromium layer portions not protected by resist are removed. Pattern is then reproduced in the chromium mask. The remaining resist is removed from the metallic layer by *Acetone*. At the end of these processes the silicon surface is covered by a pattern of chromium and is now ready for the etching process.

Isotropic crystalline silicon attack is not possible with wet etching. Etch solution erodes different crystalline planes with different rates. For example, a dilute solution of *Potassium Hydroxide* (KOH) etches a (100) silicon surface creating rectangular wells while a (110) surface produces triangular wells. Nevertheless, to realize rectangular profiles with dimensions of a few micrometers one would also consider the underetching, that is the erosion of silicon under the chromium mask. This phenomenon changes the starting horizzontal dimensions of the structures. To preserve horizontal dimensions we used a dry etching via physical erosion.

Different physical methods can be used to erode silicon through accelerated ions. In the realizzation of our masters we used a technique called *Inductively Coupled Plasma* (ICP) available at athe TASC laboratory. The plasma is generated by coupling electromagnetic energy into the gas species. The energy, in an ICP system, is provided by an RF electric field from a coil surrounding the plasma chamber. In the plasma, electrons and ions are accelerated by the external field. Since the electrons are much lighter than the ions, they will acquire a larger speed with the same energy input, and tend to leave the plasma. The plasma cloud will therefore develop a positive electrical potential compared to the surroundings, and the ions in the plasma will thus be accelerated towards the chamber walls. The ability to form very dense plasmas and at the same time control the ion bombardment of the substrate enables high etch rates with high mask selectivities[37].

3.2 Soft-lithography

Although photolithography is the dominant technology, even for large ($\mu m-$scale) features, it is not always the best and/or the only option for all applications. For example, it is not an inexpensive technology; it is poorly suited for patterning non-planar surfaces; it provides almost no control over the chemistry of the surface and hence is not very flexible in generating patterns of specific chemical functionalities on surfaces. Than alternative set of microfabrication methods, called *Soft-Lithography*, has been developed. Its name suggest the fact that "*all its members share the common feature of using a patterned elastomer as the stamp, mold, or mask (rather than a rigid photomask) to generate micropatterns and microstructures.*"[38]. Soft lithographic tecniques examples are Microcontact Printing (μCP), Replica Molding (REM), Microtransfer Molding (μTM) and so on. In figure (3.2) advantages and disadvantages between photolithography and soft lithography are compared.

Let us start with the μCP tecnique.

All printing processes need two steps: the first is to define an accurate pattern and the second is to bring it close enough to the substrate so that a suitable ink is deposited on the surface. The key of μCP is an elastomeric block with patterned relief structures on its surface that mediates intimate contact between the ink on the elastomeric stamp and the substrate. This conformal contact comprises the macroscopic adaptation to the overall shape of the substrate and the microscopic adaptation of the polymer layer to a rough surface, leading to an intimate contact without voids. Adhesion forces mediate this elastic adaptation and, even without the application of external pressure, an elastomer can spontaneously compensate for some degrees of roughness.

The most useful elastomer for this purpose is the *poly (dimethylsiloxane)* ($PDMS$). It has a unique combination of properties resulting from the presence of an inor-

	Photolithography	Soft lithography
Definition of patterns	Rigid photomask (patterned Cr supported on a quartz plate)	Elastomeric stamp or mold (a PDMS block patterned with relief features)
Materials that can be patterned directly	Photoresists (polymers with photosensitive additives)	Photoresists[a,e]
	SAMs on Au and SiO_2	SAMs on Au, Ag, Cu, GaAs, Al, Pd, and SiO_2[a] Unsensitized polymers[b–e] (epoxy, PU, PMMA, ABS, CA, PS, PE, PVC) Precursor polymers[c,d] (to carbons and ceramics) Polymer beads[d] Conducting polymers[d] Colloidal materials[a,d] Sol-gel materials[c,d] Organic and inorganic salts[d] Biological macromolecules[d]
Surfaces and structures that can be patterned	Planar surfaces 2-D structures	Both planar and nonplanar Both 2-D and 3-D structures
Current limits to resolution	~250 nm (projection) ~100 nm (laboratory)	~30 nm[a,b], ~60 nm[e], ~1 μm[d,e] (laboratory)
Minimum feature size	~100 nm (?)	10 (?) - 100 nm

[a–e]Made by (a) μCP, (b) REM, (c) μTM, (d) MIMIC, (e) SAMIM. PU:polyurethane; PMMA: poly(methyl methacrylate); ABS: poly(acrylonitrile-butadiene-styrene); CA: cellulose acetate; PS: polystyrene; PE: polyethylene; and PVC: poly(vinyl chloride)

Figure 3.2: Comparison between standard and soft lithography.

ganic siloxane backbone and organic methyl groups attached to silicon. It is fluid at room temperature because of its low glass transition temperature and can be readily converted into solid elastomer by cross-linking. For our studies we have used Sylgard 184 produced by Dow Corning supplied as a two-part kit. The first is the $Si-H$ functionalized monomer (*H-DMS*); the other a vinylic-terminated monomer (*Vin-DMS*) mixed with a platinum catalyst. The liquid mixture becomes a solid, cross-linked elastomer in a few hours via the hydrosilylation reaction between vinyl ($SiCH = CH2$) groups and hydrosilane (SiH) groups. Final polymer properties are related to two component ratio and temperature and time curing. We operate with a ratio H-DMS : Vin-DMS 10:1 to guarantee good elasticity due to not high cross-linking. Polymerization is temperature activated: we obtain better mechanical stability heating at $60°C$ for 24 hours.

The elastomeric stamp or mold is prepared by cast molding. The master, having relief structure on its surface, is fabricated using microlithographic techniques such as photolithography. It is coated with a fluorinated separation layer to reduce adhesion to PDMS. Surface is silanized by exposure to the vapor of a *Chlorine-fluorine-silane* for ~30 min. Then, a prepolymer of the elastomer (the two components are

mixed togheter) is poured over, then cured and peeled off.

Elastomers are used because they can make conformal contact with surfaces over relatively large areas and because they can be released easily from rigid masters or from complex structures. In particular, PDMS has also other properties:

a) it provides a surface that has a low interfacial free energy ($\sim$21.6 dyn/cm) and good chemical stability;

b) it is not hydroscopic: it does not swell with humidity;

c) its membrane passes gas easily;

d) it has good thermal stability (up to $\sim 186°C$ in air);

e) it is optically transparent down to $\sim$300 nm: prepolymers being molded can also be cured by UV cross-linking;

f) it is isotropic and homogeneous;

g) its interfacial properties can be changed readily either by modifying the prepolymers or by treating the surface with plasma, followed by the formation of siloxane SAMs to give appropriate interfacial interactions with materials that themselves have a wide range of interfacial free energies.

It presents also some technical problems such as shrinking upon curing ($\sim$ 1%); swelling when in contact with a number of nonpolar organic solvents such as toluene and hexane; low accuracy in registration across large areas due to its elasticity and thermal expansion; limiting in the aspect ratio of microstructures because of its softness.

However PDMS blocks having relief patterns on their surfaces are used in a number of different processes for patterning: first of all, as stamps to print patterns of self-assembled monolayers (SAMs) on appropriate substrates. This technique is called *Micro Contact Printing* (μCP) and is better explained in the next section.

An efficient method to duplicate surface informations is the *Replica Molding* (REM). The value of replica molding is that it allows duplication of three-dimensional topologies in a single step; it also enables faithful duplication of complex structures in the master in multiple copies with nanometer resolution in a simple, reliable, and inexpensive way. UV or thermally curable prepolymers can reproduce microstructures of a PDMS stamp with a shrinkage of less than 3% on curing. The fidelity of this process is largely determined by van der Waals interactions, wetting, and kinetic factors such as filling of the mold. The procedure required to produce the replica is the same described above. The relief structures on the replica are complementary to those on the mold and very similar to those on the original master.

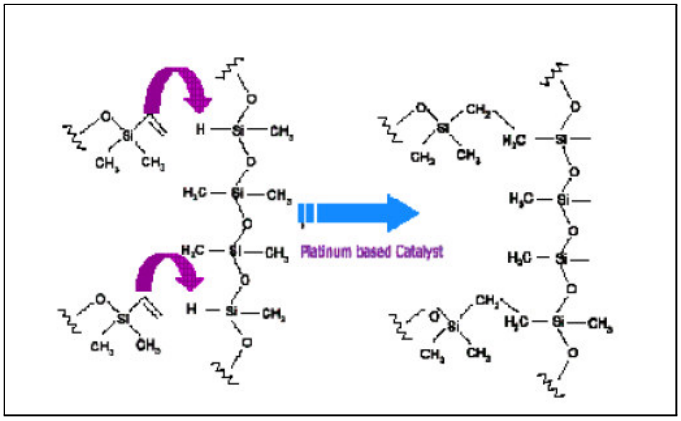

Figure 3.3: Cross-link reaction of the PDMS.

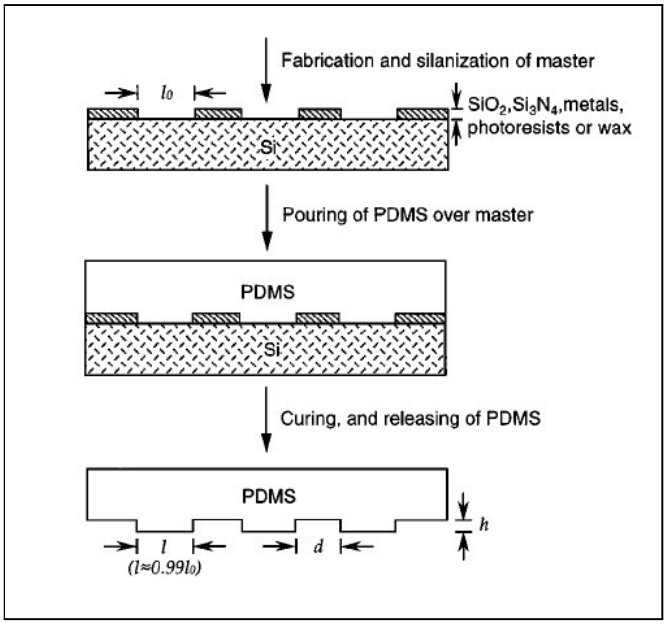

Figure 3.4: Example of PDMS stamp preparation.

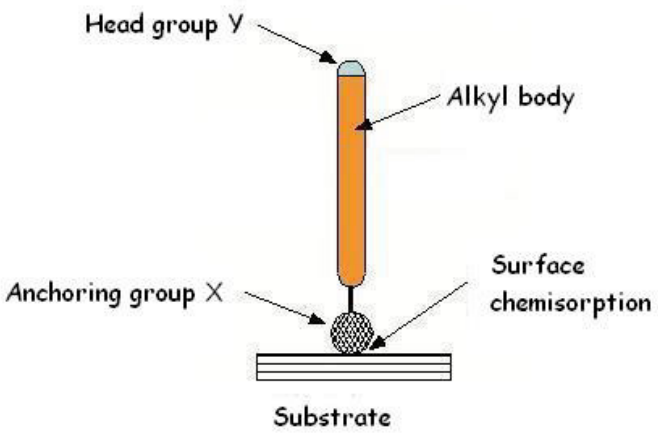

Figure 3.5: Schematic picture of a molecule giving a SAM: anchoring group X is responsible for the chemisorption on the surface; alkyl body for the packaging and head group Y for monolayer physical and chemical properties.

Thermoplastic polymers can be used to reply hard stamp: for example silicon master. After master surface silanization, a plate of thermoplastic polymer is put in contact on microstructured area. They are heated at temperatures higher than the glass transition temperature T_g of the polymer and then pressed together for a few minutes. Master and polymer are cooled maintaining pressure in between. One of the most useful thermoplatic polymer used is the *Poly-methilmetacrylate* ($PMMA$).

3.3 Self Assembled Monolayer (SAM)

Self-assembly is the spontaneous aggregation and organization of subunits (molecules or meso-scale objects) into a stable, well defined structure via noncovalent interactions[38]. The information that guides the assembly is coded in the properties (e.g. topologies, shapes, and surface functionalities) of the subunits; the individual subunits will reach the final structure simply by equilibrating to the lowest energy form.

From an energetic point of view, molecules characterized by creation of these ordered structures are composed by three parts ($Y(CH_2)_nX$): an *anchoring group* X, the *alkyl body* and the *head group* Y. The anchoring group is responsable for esothermic processes giving chemisorption of the molecule on substrate surface. Covalent or polar chemical bonds are formed between head groups and specific surface sites. Chemisorption energies are on the order of tens of kJ/mol. Alkyl bodies, instead, interact via Van der Waals forces with a bond energy of a few kJ/mol. It

is clear that self assembling is not due only to this interaction. Finally, head groups have interaction energy of about $0.017\,\mathrm{kJ/mol}$ and this explains why these groups are strongly disordered at room temperature[39].

SAMs can be easily prepared by immersion of a substrate in the solution containing a ligand reactive toward the surface, or by exposure of the substrate to the vapor of a reactive species. The thickness of a SAM can be controlled by changing the number (n) of methyl groups in the alkyl chain. Surface properties can be easily modified by changing the head group, X. SAMs exhibit many attractive characteristics: ease of preparation, good stability under ambient laboratory conditions, relatively low densities of defects in the final structures, and amenability to application in controlling interfacial (physical, chemical, electrochemical, and biochemical) properties[40].

The most common systems of SAMs are those of alkanethiolates on Au and Ag, and alkylsiloxanes and alkylsilane on hydroxyl-terminated surfaces such as Si/SiO_2, Al/Al_2O_3 and glass.

3.4 Micro-Contact Printing (μCP)

μ contact rrinting is a technique based on contact and pattern replication that rely on onefold magnification ($1\times$) masks. Thermal and chemical shrinkages of the polymer affect the absolute accuracy of molded stamps, but these effects are predictable and can be compensated in the design of the master.

Alkanethiols self-assemble on noble metal surfaces to form dense, ordered monolayers. These monolayers allow control in wettability, adhesion, chemical reactivity and so on. Accurate reproduction of small patterns can be compromised by the diffusion of ink molecules away from the zones of contact. The width of the diffusion scales with the mobility of the molecules: in general, increasing molecular weight decreases both the vapor-fase transport and the surface diffusion of the ink during printing.

Ink solution for noble metal surfaces such as Au, Ag and Cu is a few mM ethanol solution of alkanethiols. Ink solution for Si/SiO_2 or glass is a few mM toluene or normal-exane solution of alkyl or fluoroalkyl silane. Immersion inking was done by placing a drop of ink solution onto a stamp for a duration of $30s$. The ink solution was then removed under a stream of nitrogen, leaving a reproducible amount of ink on and in the stamp. This method allowed control only over the average amount of ink transferred. Contact inking selectively helps direct the ink where it is needed on the stamp. The degree of completion of the printed monolayer becomes less dependent on the geometry of the pattern, and diffusion of the thiols during printing is minimized. The transfer of ink is mediated by a PDMS ink pad pre-impregnated with thiols.

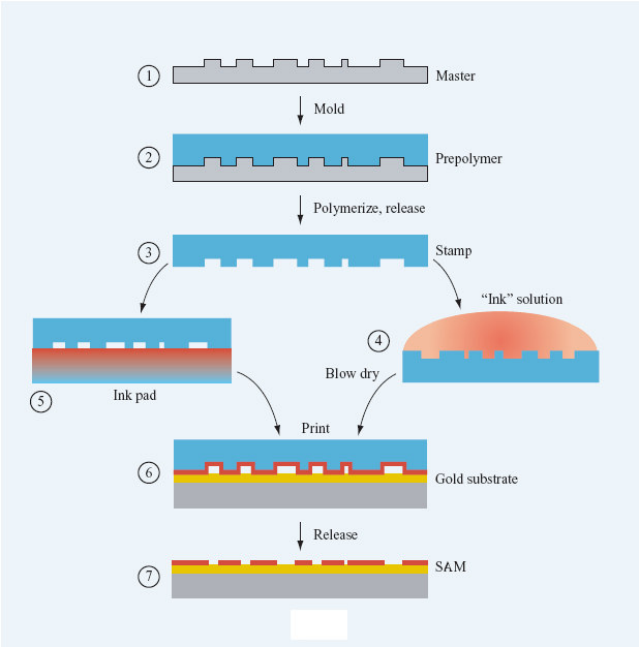

Figure 3.6: Diagram of micro contact printing process: a prepolymer (2) covering the master (1) is cured by heat or light, and demolded to form an elastomeric stamp (3). The stamp is inked by immersion (4) or contacted with an ink pad (5), and printed onto the substrate (6), forming a selfassembled monolayer (SAM).

Control over the amount of ink transferred was possible by changing the concentration of the thiol solution used for preparing the ink pad. Contrast was further optimized varying the printing time. The most challenging task in this context was to print small features or voids with high accuracy and simultaneously to print large areas with low defects counts.

In a recent experiment, patterns of 100 nm wide lines and dots have been reproduced with thiols SAM on gold. SAM patterns have a lot of application in the microfabbrication processes. They can be used like resist for wet etching, as templates in selective deposition, to change chemical reactivity of surface (see [38] and its references) or to vary wetting[42] and tribological properties[43] of a substrate. During my PhD I have done preliminary studies of the tribological properties of silicon surfaces functionalized by patterned alkylsilane SAM.

Chapter 4

Friction on homogeneous surfaces

In this chapter I show QCM studies on the frictional properties of different adsorbates on flat metallic surfaces. The electronic contribution to the total friction has been studied for systems of adsorbed gases on lead surfaces crossing the superconducting transition temperature. A study of the temperature influence in the slippage processes for these systems has been done. I also report measurements of noble gases and gold nanoparticles deposed on flat gold surfaces.

I will start from the measurements on the electronic contribution.

4.1 Experimental detection of electronic contribution

As mentioned in paragraph 1.2.1, the first report on the observation of the electronic contribution to friction was performed by Krim and co-workers[10]. They studied friction of Nitrogen ($\mathbf{N}_2$) films on a lead substrate crossing the superconducting transition using the Quartz Crystal Microbalance (QCM) and found a friction reduction by a factor ~ 2 (figure 4.1). In their experimental set-up N_2 was admitted in the cell at high temperature (room temperature or $80K$) and then cooled down to liquid He temperature, missing the control of the adsorbate deposition. This means also that the vacuum parameters of the QCM, which are absolutely necessary to quantify slippage, were taken during a different cooling run. Of course this can drastically affect the measurements. Furthermore, the sample surface was exposed to air before being inserted into the cell and no cleaning of the surface by means of ion sputtering or other was performed to guarantee the cleaness of the substrate. This fact, together with the non UHV conditions of the environment, made the surface surely not clean from oxides and impurities. Another weak aspect of the DAK work consists in the total absence of a direct detection of the superconducting transition; The transition was detected by measuring the drop in resistance across

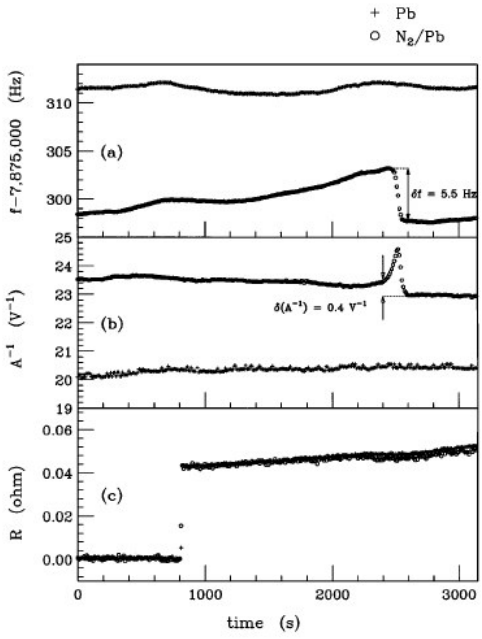

Figure 4.1: DAK data[10]: changes in frequency, Q factor and reference resistance during time for the system N_2/Pb.

a lead film evaporated on a different quartz and placed nearby the QCM. Since the quartz parameters are very sensitive to temperature, it is not automatic to indicate the transition as the responsible for the changes in energy dissipation. Observing figure 4.1 we understand how imprecise this technique may be.

The importance of the electronic channel in energy dissipation processes during sliding friction was a debated argument even before the DAK experiment. But the data obtained by Krim and coworkers in 1998 have not been exhaustively explained by any theory. Various papers have been published in which theorists gave many different possible explanations about this puzzling collapse of sliding friction across the superconductive transition. The aim of this paragraph is not to give an exaustive explanation of all the theoretical model developed to explain the DAK experiment. I refer the interested reader to look the bibliography references [44] [45] [46] [47] [48].

Taborek and collaborators [49][50] tried to repeat the same work under improved experimental conditions, but they not only did not see any jump in friction, they did not see slippage at all (fig. 4.2). Krim replied to Taborek [49] by saying that a very regular adsorption surface was necessary to observe slippage [51]. Krim and co-workers repeated the experiment under more controlled conditions after a couple of years [52]. In particular, the superconducting transition was measured directly using two coils and the evaporation of lead took place in situ. Again they found results similar to the DAK ones, but also observed that probable contamination of

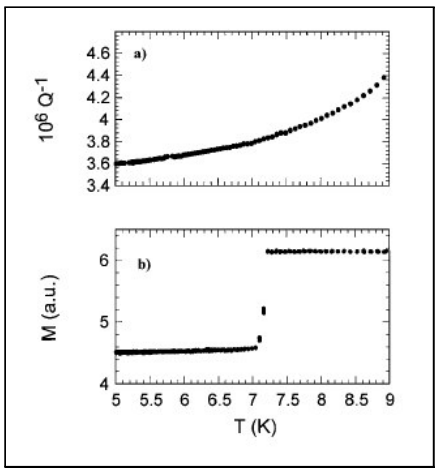

Figure 4.2: Taborek data[49]: change in Q factor crossing the superconducting transition for the system N_2/Pb.

surfaces due to the not UHV environment gave rise to non reproducibility of results. As a consequence they found slipping films, pinned one and also partially pinned layers depending on the run and on the cooling rate. In fact in this new apparatus nitrogen was still admitted in the chamber before cooling it down, leading to great uncertain about its condensation. For example a small thermal gradient in the cell would completely change the distribution of the condensate nitrogen in the cell. Furthermore in this way the uncertainties on the resonance parameters are very large. For this reason it is clear that this result is not conclusive at all.

4.2 Lead surface preparation

Lead surfaces have been prepared in the Physics department of Genoa University by the group of prof. U. Valbusa.

The Pb electrodes have been grown by physical deposition using an e-beam heated evaporation source at a rate of $0,5nm/sec$. The evaporation is performed on a blank AT-cut quartz substrate with a resonance frequency of 5 MHz polished down to an rms roughness of about $0.3nm$. Prior to Pb evaporation, the quartz substrate was annealed under UHV conditions up to $520K$ in order to remove condensed surface impurities. The deposition conditions of the lead film were carefully chosen in order to optimize the morphology of the Pb film with respect to the relevant parameters such as terrace size (step density), terrace tilt, grain size, and overall rms roughness. In order to avoid the formation of 3-dimensional clusters (Volmer-Weber growth), either elevated deposition fluxes or reduced substrate temperatures were chosen. The films used in the present QCM experiment were grown keeping the quartz substrate

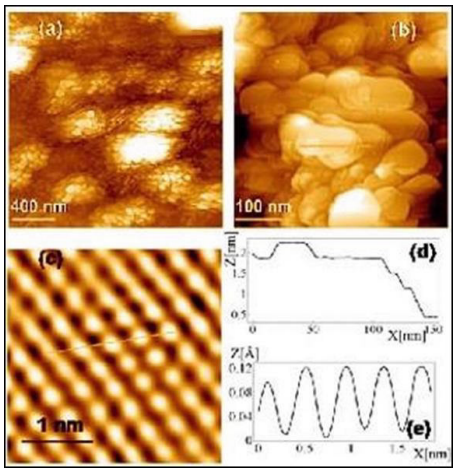

Figure 4.3: (a) Large scale ($2 \times 2\mu m^2$) STM topography of the Pb film acquired in constant tunneling current; (b) zoomed-in view ($0,46 \times 0,46\mu m^2$) of the atomic planes forming a crystalline domain separated by monoatomic steps; (c) atomically resolved image ($3 \times 3nm^2$) showing the (111) symmetry of the atomic terrace; (d) line scan across the atomic terraces of (b) evidencing the step height $0,285nm$ of Pb(111); (e) line scan across an atomic row evidencing the lattice spacing $0,35nm$ of Pb(111)[55].

temperature at $155K$, and the corresponding morphology was determined in situ within the deposition chamber by means of STM after annealing the substrate to room temperature.Figure 4.3(a) shows a large scale STM image ($2 \times 2m^2$) of a $150nm$ thick Pb electrode, which reveals a distribution of polycrystalline domains with lateral dimensions around $0,5\mu m$. The various domains can be identified by the different stacking and orientation of the platelets. The majority of them are stacked parallel to the quartz surface, with an in-plane rotational mismatch, while a minor fraction of the platelets is stacked forming a tilt angle with respect to the substrate. An inspection of one of the domains on a closer scale is shown in Fig. 4.3(b). It reveals that the platelets are formed by atomic terraces, separated by monoatomic steps with a height of $0,285nm$, corresponding to the (111) termination of Pb, as shown in a more clear way by the line scans in figure 4.3(d). A more direct identification of the (111) nature of the atomic terraces and of the degree of atomic order is obtained by atomically resolved images of the terraces as those shown in Fig. 4.3(c) and in the line scan in figure 4.3(c), which indicates a nearest neighbour distance of $0,35nm$, again corresponding to the close packed (111) surface of lead. The rms roughness of the film acquired on a large scale scan such as that in figure 4.3(a) corresponds to $4,5nm$, which is a remarkably low value compared to the total average film thickness of $150nm$. Finally, the terrace size distribution appears peaked around $20nm$, with a significant population of terraces as big as $90nm$[55].

4.3 Slip time calculation

The slip time is calculated experimentally by measuring the QCM quality factor Q and resonance frequency f variations by equation 2.12:

$$\tau_s = -\frac{\Delta\left(\frac{1}{Q}\right)}{4\pi\Delta f} \tag{4.1}$$

The quality factor is not measured in a direct way but through the oscillation amplitude, A of the electrodes (expressed in Volt) because there exists a direct proportionality between the two:

$$Q = C \cdot A = C \cdot \sqrt{V_{out}}$$

where C is a constant and V_{out} is the QCM output voltage after amplification. If Q_1 is the quality factor for the starting state and Q_2 that for the final state we can write:

$$\frac{Q_1}{Q_2} = \frac{A_1}{A_2} = \frac{\sqrt{V_1}}{\sqrt{V_2}} \tag{4.2}$$

The values in vacuum with no adsorbate covering the QCM are usually assumed as a reference, therefore:

$$\tau_s = -\frac{1}{Q_0}\frac{\left(\frac{\sqrt{V_0}-\sqrt{V}}{\sqrt{V}}\right)}{4\pi\left(f - f_0\right)} \tag{4.3}$$

where 0 indicates measurements taken in vacuum conditions and V and f values acquired with an adsorbate on the electrode surface. The slip time deduced from 4.3 is however an overstimate because the interfacial viscosity η_2 in 2.11 is refered to the total electrode surface. We need to normalize τ_s to obtain a correct estimate for the slippage:

$$\tau = \tau_s\frac{\Delta f}{\Delta f_1} \quad \text{if } \theta \leq 1 \tag{4.4}$$

$$\tau = \tau_s\frac{\Delta f_1}{\Delta f} \quad \text{if } \theta > 1 \tag{4.5}$$

where Δf is the resonance frequency shift due to the adsorption of one monolayer of adsorbate and θ is the fraction of surface covered by the adsorbate.

We can provide to estimate the error in the calculation of τ_s. Using the error propagation and after some algebra:

$$\sigma_{\tau_s} = \frac{1}{4\pi Q_0}\frac{1}{\Delta f\sqrt{V}}\sqrt{\frac{1}{4}\frac{V_0}{V}\sigma_V^2 + \frac{1}{4}\frac{1}{V_0}\sigma_{V_0}^2 + \left(\frac{\left(\frac{\sqrt{V_0}}{\sqrt{V}}-1\right)}{\Delta f}\right)^2\sigma_f^2 + \left(\frac{\left(\frac{\sqrt{V_0}}{\sqrt{V}}-1\right)}{\Delta f}\right)^2\sigma_{f_0}^2}$$

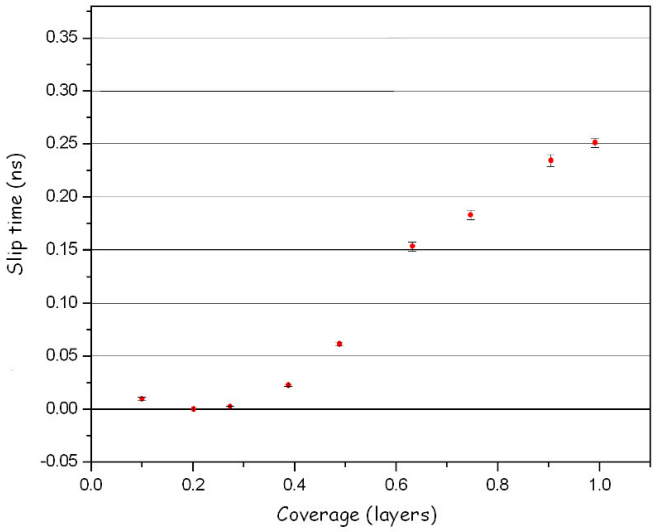

Figure 4.4: Calculated slip time for an isothermal adsorption of Ne on Pb(111) at 5,5K. Error bars have the same size of depicted points indicating vary small errors.

The interpolation fit to calculate Q_0 gives a negligible statistical error, lower than $0,5\%$. The error for τ is:

$$\sigma_\tau = \sqrt{\left(\frac{\Delta f}{\Delta f_1}\right)^2 \sigma_{\tau_s}^2 + \left(\frac{\tau_s}{\Delta f_1}\right)^2 \sigma_f^2 + \left(\frac{\tau_s}{\Delta f_1}\right)^2 \sigma_{f_0}^2}$$

in which we cannot estimate the error for Δf_1 because in literature is not reported any error for the areal density.

The error in the measured frequency is $\pm 0,1\,\mathrm{Hz}$ while the error for the readed amplitude is $\pm 1mV$. Considering an oscillation amplitude $V \sim 1V$ and a resonance frequency $f \sim 15MHz$ we can estimate σ_τ. Figure 4.4 shows the calculated slip time for an isotermal adsorption of Ne on Pb(111) at $5,5K$, for more details see section 4.5. In the graph I have also reported the error bars: we can see that error bars have the same size of the depicted points. Errors for the calculated slip time are very small, lower than a few percent. For this reason in the next data analysis I neglect to indicate error bars for the calculated slip time in the remaining graphs.

4.4 Friction of nitrogen films on lead

The first step in the experiment consists in the observation of slippage at low temperature, which is a necessary condition in order to estimate electronic contribution. In particular we need to have measurable slipping times ($\sim 1nsec$ at least) in

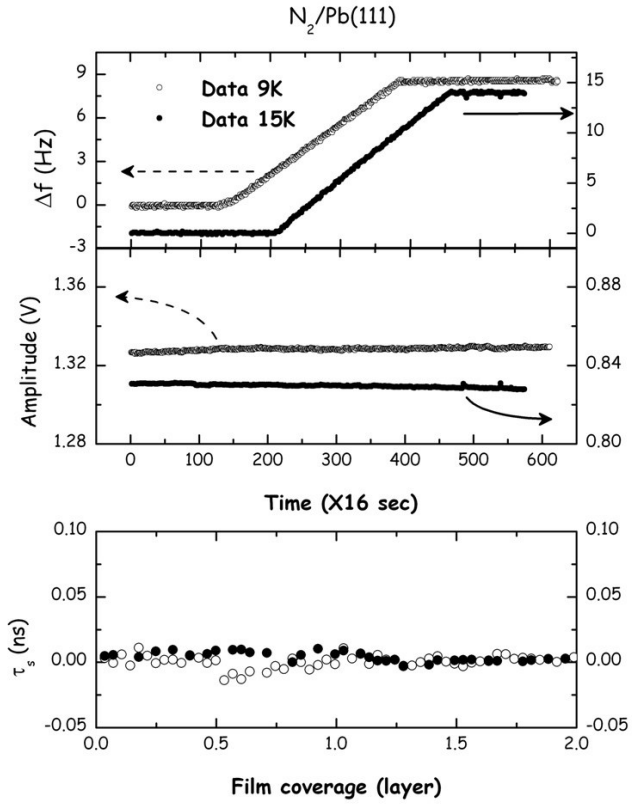

Figure 4.5: Raw data of the resonance frequency shift (top) and oscillation amplitude (middle) during an isothermal deposition of N_2 on Pb. Bottom: calculated slip time as a function of N_2 film coverage. Full circles refer to data taken at $9K$, empty circles to data at $15K$[53].

correspondence to temperatures around $7,1K$, which is the transition temperature of lead. The presence of nonzero slipping times under these conditions is not obvious, since there are only two experiments in literature about it, and their results are very different[10][49]. A major difference between our experiment and theirs is that we deposit the adsorbate directly onto the QCM in a controlled way, while Krim and coworkers introduce a certain amount of gas to the QCM cell at $85K$and then cool it down to $4,2K$[10].

The chamber was baked out for several days and the residual pressure was $\sim 10^{-10}Torr$; the sample, which was exposed to air, was cleaned using the ion gun to remove the superficial layers before to start measurements. High-purity N_2 was evaporated directly on one QCM electrode through a stainless steel capillary attached to a sapphire leak valve.

First data have been acquired at a temperature of $5,5K$ but no change in oscillation amplitude of the quartz was detected. Measurements were repeated over

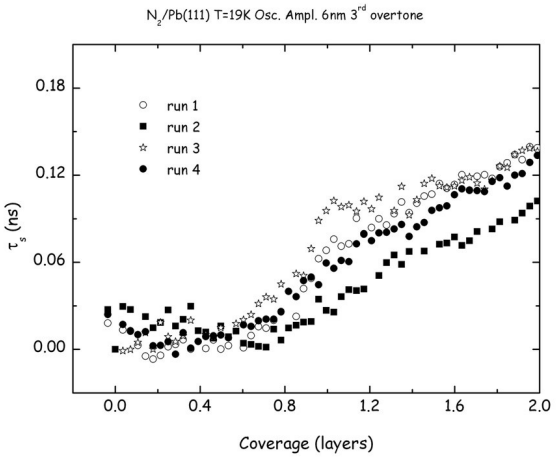

Figure 4.6: Normalized slip times of N_2 films deposed on Pb(111) at $19K$.

one week. After each acquisition, the adsorbed film layer was desorbed from the surface by heating QCM at temperature slightly above $30K$ achieved by tunning off the cryocooler. We repeated the measurements at different T. Figure 4.5 shows the resonance frequency shifts and the amplitude variations measured while dosing nitrogen on the Pb(111) electrode at temperatures of 9 and $15K$. The data have been acquired at the third overtone of a $5MHz$ quartz plate characterized by a Q-factor of 300 000 at low temperature. The oscillating amplitude of the quartz plates is estimated to be $\sim 5nm$. Accordingly, the lateral force F experienced by a N2 molecule is $\sim 0.002fN$. The resonance frequency stability of the QCM is $\sim \pm 0.1Hz$, essentially caused by the finite resolution of the digital counter, while that of the oscillation amplitude is $\sim \pm 1mV$. The frequency shift corresponding to the adsorption of a monolayer of N_2 on one QCM electrode is calculated to be equal to $2,8Hz$[10].

It is evident that no change in amplitude is observed while dosing. This is more clearly seen in the bottom graph of figure 4.5, which displays the normalized slip time τ_s as a function of film coverage. We have repeated the data acquisition at each temperature a few times over a period of a week without finding any particular difference from the data of figure 4.5. We have taken similar measurements at a temperature of $19K$, and a representative data set is displayed in figure 4.6. As before, no change in dissipation is observed until the film coverage reaches a value near $0.8layers$, beyond which dissipation starts, and the film slides. The data reproducibility is a key aspect in these studies. We have then acquired numerous isotherms by slightly changing the acquisition procedure: (i) dosing the nitrogen film continuously or in steps; (ii) changing the dosing rate; (iii) cleaning the Pb surface by heating up the QCM at different temperatures. Figure 4.6 shows four of

these runs, which indicate the data reproducibility in this experiment[53].

Although the data present some scatter, it is clear that beyond $0,8 layers$ dissipation starts at tempearature of $19K$. The observed no-slippage of nitrogen at low temperature may be due to defects and/or contaminants of the Pb surface that act as pinning centres. Although our Pb surface is not an ideal crystalline surface, we do not think that this is the explanation for our results. Atomic terraces have a characteristic size of $50nm$, while the QCM oscillating amplitude is of the order of $5nm$ and the molecular size is $\sim 0.4nm$. Accordingly, in the isothermal scan most of the molecules will experience the surface as being essentially flat. During the experiment, these surfaces were sputtered at room temperature in order to recover the clean pristine state by removing a few layers of the Pb film. Due to the high mobility of Pb, recovery of surface damage induced by ion irradiation is very efficient already at temperatures around $300K$.

In our opinion, these observations suggest that the static friction of nitrogen at low temperature is not a direct consequence of the Pb surface quality but, more likely, reflects a strong corrugation in the resulting surface potential experienced by the film atoms/molecules. The weak force of inertia exerted by the QCM is not sufficient to move the atoms/molecules from their equilibrium positions and it is necessary to increase the temperature to activate the sliding process.

This interpretation is also consistent with very recent molecular dynamics simulations of the static friction of a N_2 slab on a crystalline Pb(111) substrate[61]. In the temperature range 0 to $20K$, the kinetic energy of the N_2 molecules is much lower than the corrugation of the surface potential, and the static friction force per molecule remains temperature independent and very large. At slightly higher temperatures, a misplacing of planes occurs at the interface, altering the N_2 fcc structure. Above $25K$, this misplacing moves into the bulk of the N_2 slab, and a sharp drop in the static friction is observed.

4.5 Neon monolayers on lead: structural depinning

The second system studied is neon films adsorbed on Pb(111) surfaces. The data have been acquired at the third overtone of a $5MHz$ quartz plate characterized by a quality factor of 380 000 at low temperatures. The oscillating amplitude of the quartz electrodes is estimated to be $1nm$. The stability of the resonance frequency is better than $0,1Hz$, while that of the amplitude is $1mV$. For the determination of the film thickness, we have assumed an areal density for the completion of one Ne monolayer of $0,123\ atoms/A^2$[1]. Accordingly, the frequency shift for the deposition

[1]Private comunication of prof. F. Ancilotto.

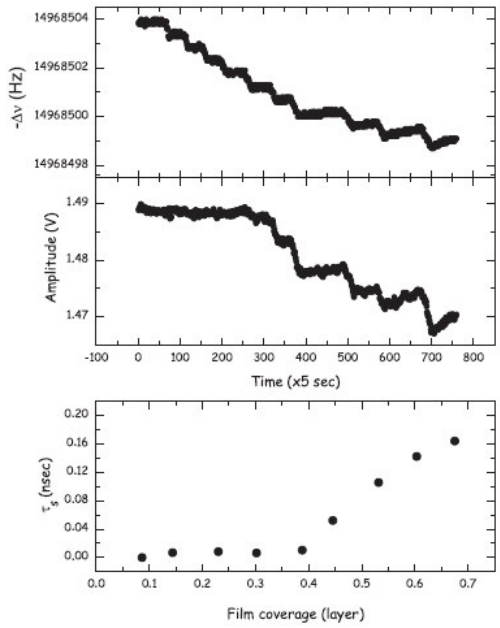

Figure 4.7: Raw data of the resonance frequency shift (top) and amplitude (middle) during an adsorption isotherm of Ne on lead at 6.5 K. Bottom: Calculated slip time as a function of Ne film coverage.

on one QCM electrode of a Ne layer is calculated to be equal to $7Hz$. By acting on the leak valve, the film is grown both in steps of about 0.1 *layers* and continuosly at different dosage rates. After each acquisition, the adsorbed film layer was desorbed from the surface by heating QCM at temperature slightly above $30K$, at this temperature Ne has vapor pressure of some mbar guaranteeing a total desorption from the substrate in UHV environment.

The two top graphs in Fig. 4.7 show the raw QCM data corresponding to the deposition of Ne on Pb(111) at a temperature of 6.5 K. In the top graph, steps variation of resonance frequency is plotted in fuction of elapsed time. Corresponding resonance amplitude variation is plotted in the middle graph. At low coverages, there is no change in the quartz amplitude, and only above $\approx 0,4$ layers does dissipation start to appear. This behavior is better expressed in terms of slip time τ_s. The bottom graph shows a slip time of practically zero at low coverages, while above $\approx 0,4 - 0,5$ layers τ_s is distinctly different from zero and reaches a value of $0,3$ *nsec* at monolayer completion, a typical value for rare gases adsorbed on metal surfaces[54]. At higher coverages, the resonance parameters are not stable over time. We believe that this behavior is due to a progressive desorption of the Ne atoms evacuated by the turbomolecular pump attached to the UHV chamber[55].

As said before, reproducibility is a fondamental aspect for these studies. Figure

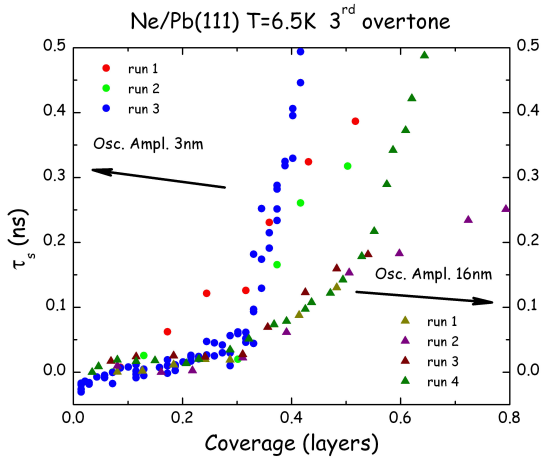

Figure 4.8: Calculated slip time of Ne monolayers on Pb(111) at $T = 6,5K$ at two different excitation powers.

4.8 shows calculated slip time for measurements taken at the same temperature $T = 6,5K$ but with different excitation power. The corresponding oscillation amplitudes are $3nm$ for the lower excitation and $16nm$ for the higher. Data has been acquired over a few days for each fixed excitation. We can see a very good agreement in the data: starting point for slippage at the two amplitudes is close to about $0,4$ layers and slip time has about the same values for equivalent surface coverage.

Figure 4.9 shows the slip times measured at the same temperature T $6,5K$ and excitation power but in different acquisition runs. More precisely, the measurements of runs (a) were taken over a two-day period, while those of set (b) were acquired within a week. In figure 4.9 calculated slip times of Ne measured at T $5,4K$, the minimum temperature that it was possible to control during this experiment, are also compared with those taken at $6,5K$. Also for this temperature measurements was repeated in different days and with different adsorption rate but the same excitation power.

Although there are no data available in the literature on the 2D phase diagram of Ne adsorbed on Pb(111), it is tempting to interpret our data in terms of a structural depinning of the film. Let us consider, for example, data at $6,5K$. At small coverages, the Ne film is in a fluid phase that at such low temperatures is practically locked to the substrate. Close to about $0,4$ layers, some incommensurate solid islands, which are weakly bound to the surface, start to slide. For data at $5,5K$ slippage starts below above $0,5$ layers. This interpretation is consistent with the structural phase diagrams of heavy rare gases adsorbed on Ag(111) [7][56], systems that are likely not too dissimilar to Ne/Pb(111). Our measurements are also in very good qualitative agreement with the results of extensive classical molecular-

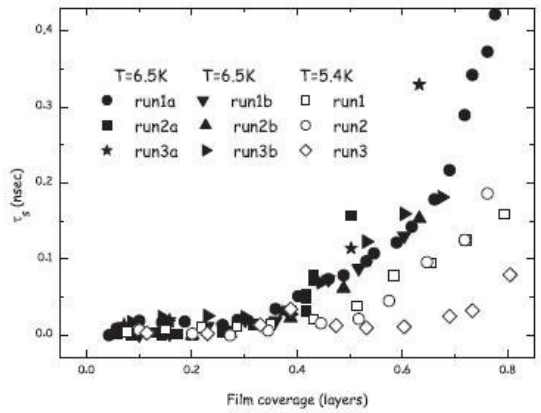

Figure 4.9: Normalized slip times of Ne monolayers on lead taken at $5,4$ and $6,5K$ in different days[55].

dynamics simulations of a model system carried out by Persson[1] in the case of a low corrugated substrate In figure 4.10 experimental data at the two temperatures (a) are compared with Persson simulations (b). Differences are present in starting slip time between experiments and simulations: for the former it is pratically zero, for the latter it is different from zero. Drawn curves in Persson simulations refer to higher temperatures than that of our measurements. Energetic factor for our set up at temperature T $6K$ is $k_BT/\varepsilon = 1/7 \approx 0.14$. Extrapolating the corrispondent curve, it would be in the bottom part of the graph and the slip time at very low coverage with value near zero.

Although the two temperatures are not too widely separated, the data at lower T suggest a depinning at $0,5$ layers, slightly above that found at higher T, indicating that this process is thermally activated.

With the same experimental set up a second lead film has been evaporated on a new blank 5MHz quartz in Genova laboratory. Data for this new QCM have been acquired at its third overtone at a frequency of about 15MHz with a Q-factor $\sim$ 250000 and an oscillation amplitude of $\approx 6nm$. Stability in frequency and amplitude signals is of the same order of magnitude of the former sample.

Measurements have been repeated depositing Neon films on the lead electrode at a temperature $T = 5,5K$. Figure 4.11 shows the calculated slip time for different runs acquired over a period of a few days. As we can see, data show good reproducibility. Figure 4.11 also compare the calculated slip time for the two samples: the starting point for the slippage is pratically the same for both samples and the curves behaviour reflects that of the first sample: for low coverages the slip time has a value pratically zero and increasing coverage, below above $0,5$ layers, the slip time increases.

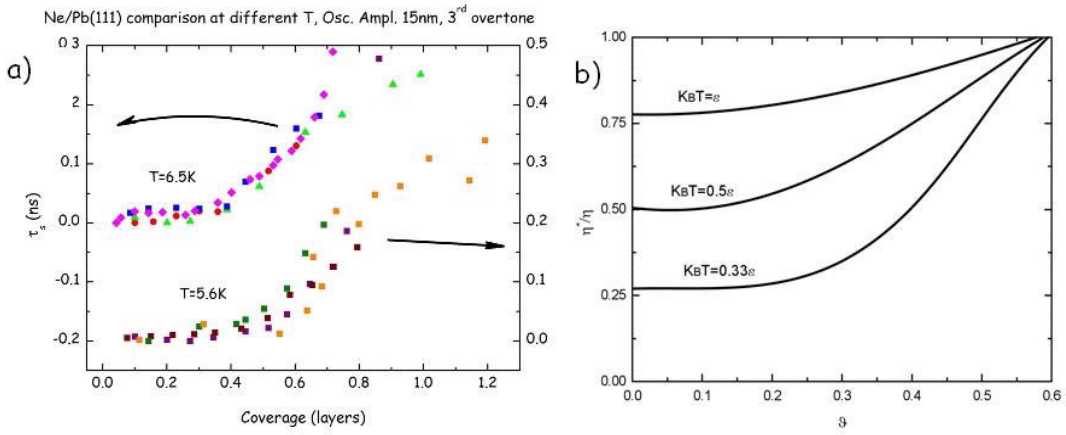

Figure 4.10: Comparison between our experimental data and the Persson's simulations: figure a) shows the calculated slip time at different coverages and at two different temperatures for Neon films adsorbed on lead; figure b) shows calculated friction coefficient η at different coverages and different temperatures for adatoms on a flat surface with a low corrugation[1].

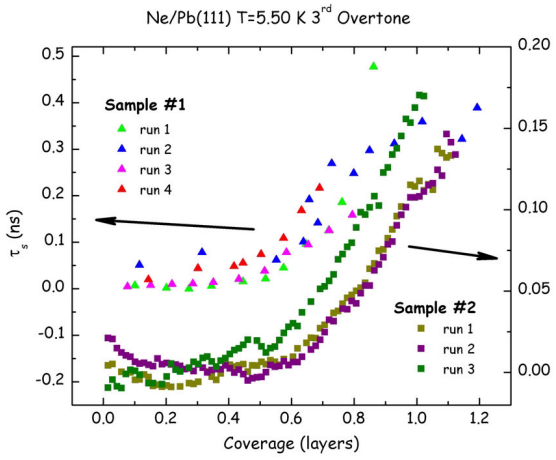

Figure 4.11: Comparison between calculated slip time τ for the first and the second QCM samples at the temperature $5,50K$: data have the same behaviour, suggesting a structural depinning of Ne monolayers on Pb(111).

We believe that such a good reproducibility is the result of two concurrent factors. First of all, the UHV system guarantees a very clean environment. However, we have found a progressive decrease in the dissipation and, accordingly, in the slip time, over extended measurement time periods longer than about 3 weeks. In such cases, we could effectively regenerate the Pb electrode by removing surface contaminants via ion sputtering, since the substrate damage induced by ion collisions is rapidly healed by thermally activated diffusion already at room temperature. Thanks to the large diffusion coefficient of a lead surface, this process likely removes the contaminants deposited over time on the electrode without significantly altering the initial morphology.

The numerical results of Persson's simulations show a pronounced temperature dependence of τ_s in the submonolayer region. Our data are consistent with these findings. We think slippage observed of Ne monolayers over a lead surface at temperatures below 7 K are suggestive of a structural depinning in agreement with Persson molecular-dynamics simulations.

Data acquired for the second sample confirm this behaviour. Unfortunately a problem with the degradation of lead surface did not permit us to take measurements also at a higher temperature.

4.6 Neon monolayers on lead: electronic contribution

A direct way to measure the electronic contribution is to study the friction variation when the metal crosses the superconducting transition as anticipated in section 1.2.1. First of all we need a gas that shows slippage under the transition temperature T_c. We studied the behaviour of Ne films adsorbed on a lead surface, a sysem that has already been described in the previous section. We tried to quantify the electronic contribution to slippage by measuring the oscillation amplitude variations while crossing the lead superconducting transition temperature.

A fraction of $\sim 0,7 - 0,8$ layers of Neon was adsorbed on the lead surface at a temperature $T = 6,7K$ and the QCM responce was monitored while increasing the temperature. Figure 4.12 shows a typical temperature scan. Data was acquired at the third overtone of the sample #1 described in the previous section and at an oscillation amplitude for the electrodes of $\sim 16nm$. Starting from $T = 6,7K$ we have increased temperature in steps of $0,03K$, waited for the system to equilibrate, acquired data and then increased again temperature until the total transition to a normal conductor occured. The first graph in the top shows the oscillation amplitude acquired for each temperature step; the second shows the corresponding variation in the resonance frequency; the third shows the temperature at each acquisition and the last graph shows the pick-up signal. The QCM was mounted between two

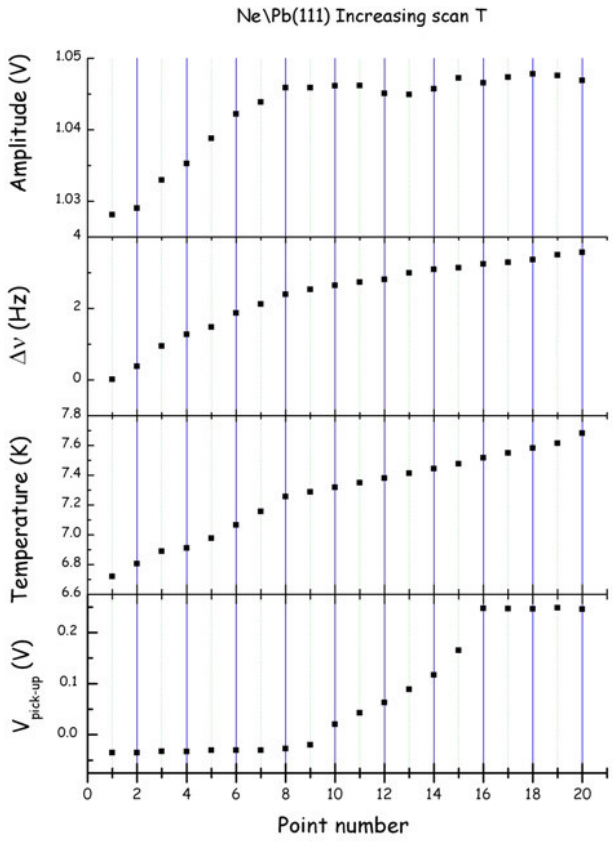

Figure 4.12: Typical increasing temperature scan. From top to bottom: oscillation amplitude acquired at each step; corresponding frequency variation; fixed temperature of each step; pick-up signal to detect the superconducting transition.

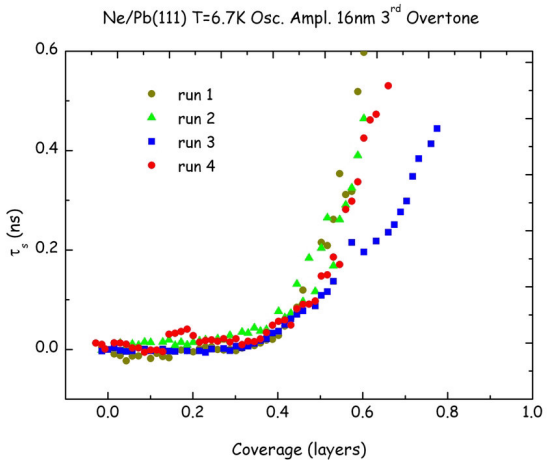

Figure 4.13: Calculated slip time τ for Ne adsorbed on Pb(111). Data refer to dosages perfomed before starting the increasing temperature scans.

Meissner coils (pick-ups) used to detect the superconducting transition as can be seen in section 2.5.

In figure 4.13 the calculated slip time for the Neon deposition on lead at $T = 6,7K$ is plotted against the surface coverage. Data were taken in different days, before starting with the temperature scans. They are in very good agreement with the data discussed in the previous section.

Let us consider a film adsorbed on the surface and dissipation occuring at the interface. Starting from a temperature lower than T_c, increasing T we expect an increase in the dissipation crossing T_c. The predicted total friction variation could have different trends depending on the theoretical models considered. Figure 4.14 shows three different behaviours: a discontinuos drop (fig. 4.14 a); a linear variation (fig. 4.14 b) and a power low decrease (fig. 4.14 c).

If the electronic contribution to slippage is 1/2 of the total slippage -as reported by Krim and coworkers[10]- crossing T_c we espect to detect a decrease of a few percent in the oscillation amplitude. The pick up signal did not show a sharp transition from normal conductor to superconductor. The transition started to a temperature of $7,2K$ and finished at T $7,5K$. Figure 4.15 summarized data acquired during the increasing temperature scans. The oscillation amplitude of the QCM is plotted as a function of the temperature. In the picture the grey lines limit the temperature window in which superconducting transition occur. A preliminary temperature scan was done with the bare lead, without any adsorbate. Red points in figure 4.15 refers to a no coverage scan. Anomalous signals for the QCM oscillation amplitude were not observed crossing the superconducting transition rather the amplitude curves

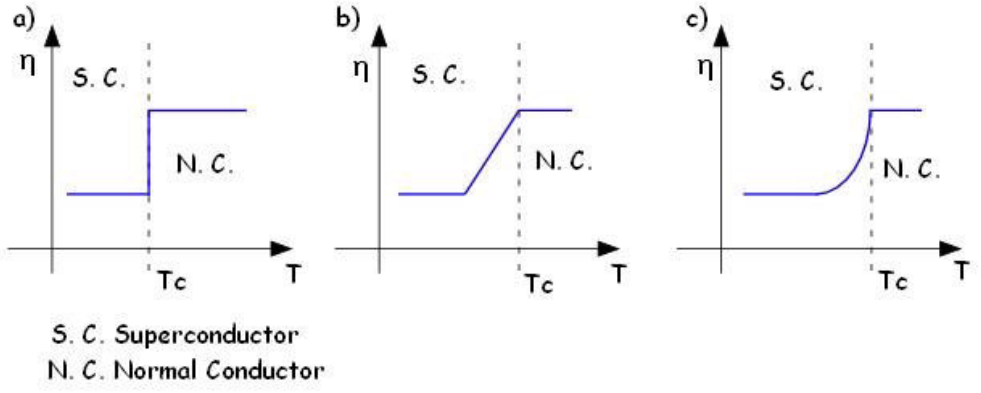

Figure 4.14: Different scenarios for the friction coefficient η variations crossing T_c: (a) a discontinuous jump ; (b)a linear change; (c) a power low decrease.

showed a behavior similar to the bare QCM. These data were taken over a two weeks period.

The same procedure has been repeated decreasing the temperature: we have dosed a fraction of Ne monolayer of $\sim 0,6 - 0,7$ layers at temperature $T = 7,6K$ higher than T_c, decreased temperature in steps of $0,03K$, waited for a stable signal and so on.

Figure 4.16 refers to Ne film depositions before starting the decreasing temperature scans. The calculated slip time at different coverages is plotted. Data show very good reproducibility, the calculated slip times have values comparable with the former runs and the data trend is the same discussed before.

In figure 4.17 the oscillation amplitude as a function of incresing T is plotted. The grey lines limit the temperature window in which superconducting transition occurs. Also for these measurements, a preliminary temperature scan was done with the bare lead. Purple points in figure 4.17 refers to the no coverage scan. Only the blue data points show a change in the trend of oscillation amplitude suggesting a total friction increase while crossing the superconducting transition. Unfortunately these data have not been reproducted and other runs did not confirm this behaviour.

For the sample #2 we have acquired data for increasing temperature scans as described above. Measurements were taken over a two-week period. Data are shown in figure 4.18. Red points refer to the no coverage scan and the orange line depicts the pick-up signal indicating the superconducting transition. The superconducting transition occurred between $6,75K$ and $6,90K$. We think the desagreement with the standard value of $7,2K$ is simply due to a not perfect thermal anchoring of the QCM. The measured temperature is that of the calibrate diode glued in the holder. Accordingly the superconducting transition was detected at an apparently lower temperature.

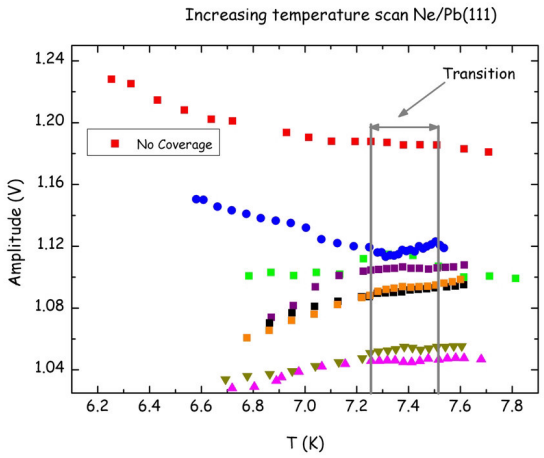

Figure 4.15: Increasing temperature scans acquired for Ne films on Pb(111) for sample #1. The oscillation amplitude is plotted respect to the temperature. Red points refer to the no coverage scan. Data do not show significative variations in the oscillation amplitude imputable to variations in the total friction.

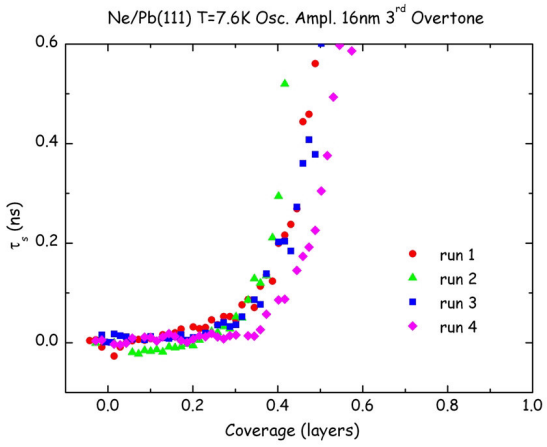

Figure 4.16: Calculated slip time τ for Ne adsorbed on Pb(111). Data refer to dosages perfomed before starting the decreasing temperature scans.

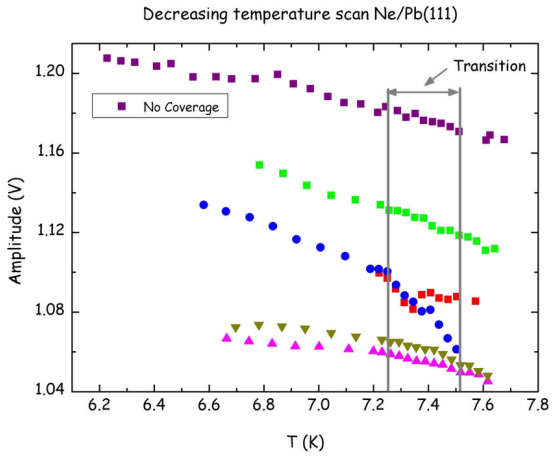

Figure 4.17: Decreasing temperature scans acquired for Ne films on Pb(111) for sample #1. The oscillation amplitude is plotted respect to the temperature. Purple points refer to the no coverage scan. Only the blue data show a incline variation that could suggest an increase in the total friction, but it was not reproducted.

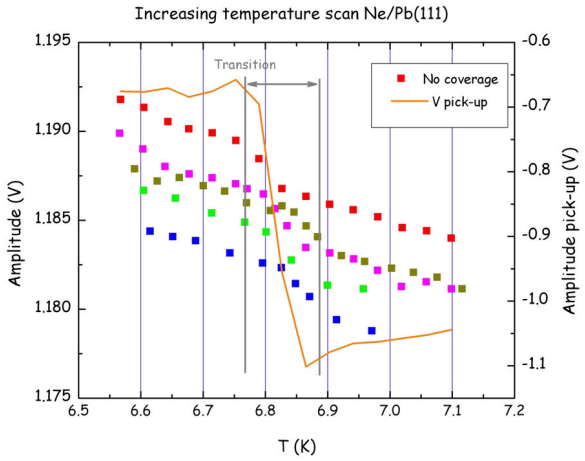

Figure 4.18: Increasing temperature scans of Ne films on Pb(111) acquired with sample #2. The oscillation amplitude is plotted with respect to the temperature. Red points refer to bare Pb surface. Orange line is the pick-up signal showing the superconducting transition. Data do not show significative variations in the oscillation amplitude imputable to variations in the total friction.

Again these data did not show any anomalous behavior in the oscillation amplitude signal across T_c. Unfortunately the degradation of the lead surface for the sample #2 did not allow us to acquire decreasing temperature scans.

Data acquired with the two different samples did not show any clear evidence of the electronic contribution to the total dissipation. This negative result does not necessarily exclude the existence of electronic friction. Indeed the coupling between Ne atoms and the lead surface electrons may be very weak because of two factors: 1) Neon small polarizzability; 2) Neon lacks of a quadrupole moment. Actually, theoretical calculations by Bruch[57] show a very small electrostatic effect Ne on Pb(111) at temperature $T \sim 10K$.

In all these measurements the superconducting transition was induced thermally, by means of changing the system temperature. This could influence the interaction mechanisms involved in dissipation. In future measurements the superconducting transition will be induce applying an external magnetic field in order to reduce the system perturbation.

4.7 Friction of heavy noble gases on lead

Measurements done by our group with heavy noble gases on gold substrate at the liquid nitrogen temperature showed a dynamical depinning transition[54]. We have then decided to study the sliding behavior of heavy noble gases on lead at $T \leq 20K$.

4.7.1 Argon

Measurements were done at the third overtone of the QCM at a frequency of 15 MHz and an oscillation amplitude of ~ 13 nm. First data were acquired at $5,5K$ growing Ar film on surface with a continuous low rate deposition. No changes in the oscillation amplitude was detected indicating the pinning of the film on the lead substrate. The surface was cleaned by heating the QCM at temperature $\sim 35K$ to desorbe the adsorbed Ar atoms. We have then repeated measurements at this temperature slightly changing the acquisition procedure: changing the dosing rate and heating the sample at different temperatures. A dissipation was not detected for this system at this temperature.

Figure 4.19 shows tipical runs acquired at temperature of $9K$ and $15K$. A change in oscillation amplitude (middle plot) was not detected in correspondance of changes in resonance frequency (top plot) due to adsorption of Ar films. The calculated slip time (bottom plot) at different coverages summarized this behaviour: no rilevant changes from zero are visible. Repeated measurements at the two temperatures did not show slippage for Ar films.

Increasing temperature at $20K$ a decrease in oscillation amplitude was detected beyond the $\sim 0,8 layers$. Figure 4.20 summarized the calculated slip times for

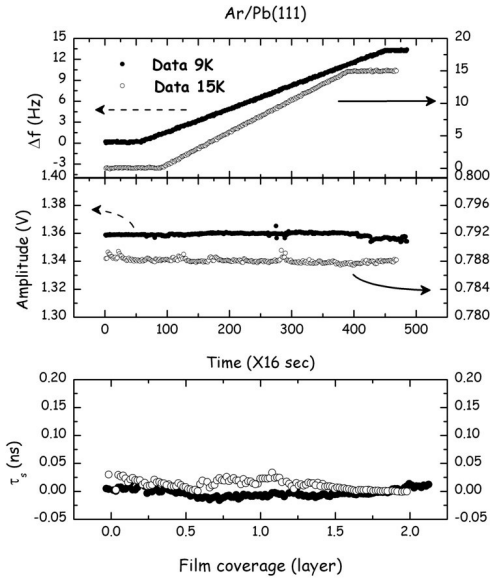

Figure 4.19: Raw data of the resonance frequency shift (top) and oscillation amplitude (middle) during an isothermal deposition of Ar on Pb. Bottom: calculated slip time as a function of Ar film coverage. Full circles refer to data taken at $9K$, empty circles to data at $15K$

measurements taken at this temperature. Despite the data show a slip time nearly zero at low coverages, while close to $0,8 layers$ τ_s is found to increase. In other words for low coverages film is pinned to the surface and near one monolayer deposed the slippage starts.

The no slippage observed at low temperature could be ascribed to the surface quality or to the presence of contaminants on the surface. Measurements taken for other adsorbates and shown in previous sections suggest this picture is not exhaustive. As I said the lead surface had terraces with characteristic dimensions of $50nm$ while the oscillation amplitude was $\sim 12nm$. Accordingly, most of the Ar atoms will experience the surface as being essentially flat.

In my opinion, these observations suggest that the static friction of Argon at low temperature is not a direct consequence of the Pb surface quality but, more likely, reflects a strong corrugation in the resulting surface potential experienced by the film atoms. The weak force of inertia exerted by the QCM is not sufficient to move the atoms from their equilibrium positions and it is necessary to increase the temperature to activate the sliding process.

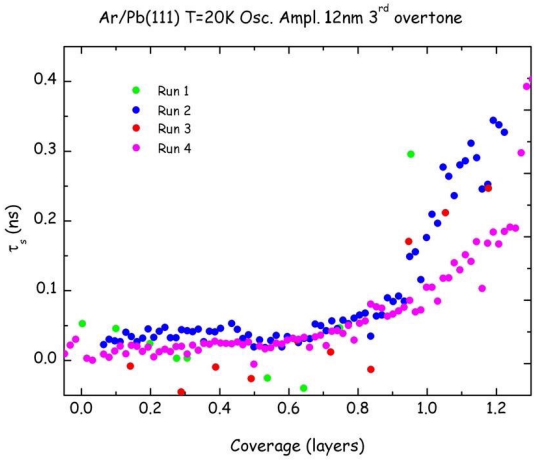

Figure 4.20: Normalized slip times of Ar films deposed on Pb(111) at $20K$.

4.7.2 Krypton

Krypton mass is twice the Argon mass. We should expect a similar behaviour for the two noble gases. Slippage measurements has been taken in the same conditions for both gases. Repeated acquistions at $5,5K$, $9K$, $15K$ and $20K$ did not show dissipation any evidence for this system.

Again, w e think the thermal energy involved at these temperatures is not enough to activate the sliding process. Measurements at higher temperature will be taken in the next future as soon as a new lead substrate will be prepared.

4.8 Friction of neon monolayers on gold

The second metallic substrate studied was gold. Gold substrate guarantees the absence of oxide on the surface and could be easly cleaned from organic contaminants with an UVO cleaner. QCM coated with optically polished gold electrodes has been purchased by Lap-Tech Inc.

A typical commercial gold substrate has been analyzed using STM.Figure 4.21 shows a $2\times2\,\mu\mathrm{m}^2$ topographic scan. We clearly distinguish many differently oriented grains, whose size is of the order of $100\div200\,\mathrm{nm}$. Usually gold atoms tend to organize themselves in a fcc structure, and a similar substrate tipically shows a superficial re-organization which is a mix of (111) faces (about 85%) and (100) ones[58].

The data have been acquired at the third overtone of a 5 MHz quartz plate characterized by a Q-factor of ~ 400000 at low temperature. The oscillating amplitude of the quartz plates is estimated to be $\sim 8nm$. The resonance frequency stability of the QCM is $\sim \pm0.1\,\mathrm{Hz}$ while that of the oscillation amplitude is better than $\pm1\,\mathrm{mV}$.

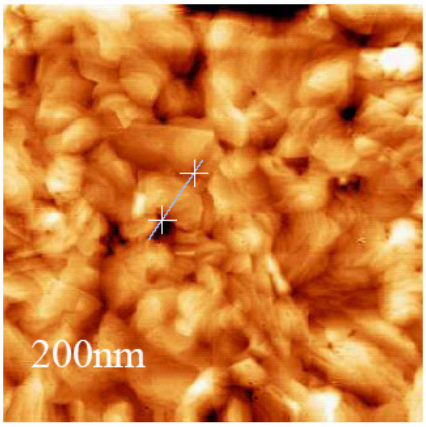

Figure 4.21: STM image of a commercial QCM gold electrode.

Figure 4.22 show a typical isothermal dosage of Ne on the gold electrode taken at a temperature $T = 6K$. In the top graph the resonance frequency is plotted while in the middle graph the corrispondent oscillation amplitude variation is presented. Before starting the deposition, we can note the amplitude stability having a scatter around the everage value of $\pm 0,2\,\mathrm{mV}$. A pronounced shift in the amplitude has been measured increasing the surface coverage. The bottom graph shows the calculated slip time: the slippage starts beyond a coverage of $\sim 0,5 - 0,6 layers$. The gold surface was cleaned by heating the system at a temperature of 30 K to desorbe the Ne film. Measurements have then been repeated over a three-day period.

Figure 4.23 summarized the normalized slip time calculated for data acquired at two different temperatures: 6 K and $7,5$ K. Data have some scatter but the behavior at the two temperatures suggests a good reproducibility.

Neon on the two metallic substrates analized shows slippage. The calculated slip time for the gold surface has values of one order of magnitude lower than that for the lead substrate. The interaction potential for Ne on gold and on lead is again not well clear. We think it should be analogous for the two systems. The surface roughness plays obviously an importante role. The lead substrate was characterized by atomic terraces parallel to the quartz surface presenting a (111) orientation. Gold instead has a policristalline surface with big grains. The average roughness for gold is higher than for lead. This reduces the slippage on a surface. Another possible explanation is that the electronic contribution to the total friction is significant for gold at these temperatures.

By depositing an insulating overlayer on the gold surface it is possible to modulate the distance from adatoms and the surface electrones. In this way the electronic coupling could be reduced. The next section shows measurements of Neon adsorbed on increasing insulating overlayers.

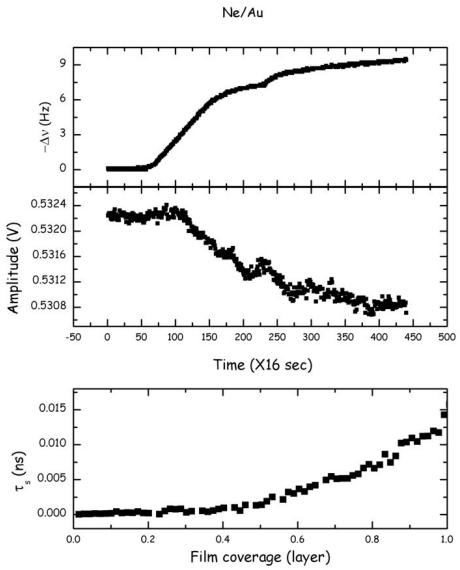

Figure 4.22: Raw data of the resonance frequency shift (top) and oscillation amplitude (middle) during an isothermal deposition of Ne on Au. Bottom: calculated slip time as a function of Ne film coverage.

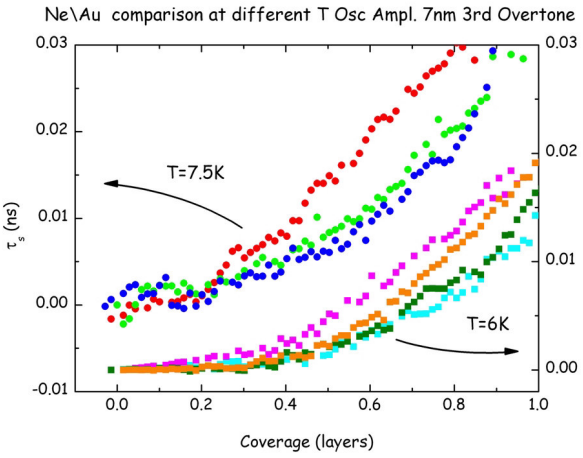

Figure 4.23: Calculated slip time for Ne films adsorbed on Au substrate at two different temperatures.

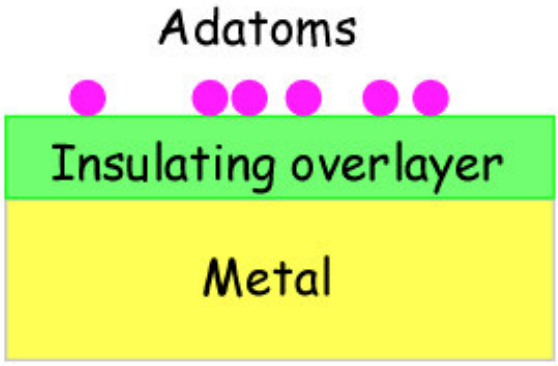

Figure 4.24: Schematic rapresentation of the experiment: an insulating overlayer is adsorbed on a metallic to increase distance from adatoms and surface electrones.

4.9 Friction of neon monolayers on krypton multilayers

Krypton monolayer adsorbed on gold substrate do not show slippage at temperatures below 10 K[59]. It is a perfect electrical insulator and with our experimental set up it is possible to deposit films with a precision of a fraction of monolayers. In other word it is possible to modulate the insulating thickness layer by layer. The aim of these measurements is to study changes in the slippage increasing the insulator thickness. i. e. reducing the adatoms-superficial electroneic coupling.

Preliminary scans were done adsorbing Ne on gold at a temperature $T = 6K$. One monolayer of Krypton was then adsorbed on the gold substrate. In agreement with previous measurements[59] it did not show dissipation and appeared pinned to the surface.

On the Krypton layer a Ne film was grown continuously and resonance frequency and oscillation amplitude variations were detected. Signals showed dissipation occurring at the interface due to the Ne deposition. The Ne film was then removed by heating sample at $T = 30K$: at this temperature Ne desorbes from the surface while Kr remains pinned. The resonance frequency after desorption returned to the starting value according to a few tenth of Hz. Scans were repeated a few times showing a good reproducibility.

Figure 4.25 shows the calculated slip time at different coverages for the bare gold (red data), for Ne films adsorbed on one Kr overlayer (blue and green data) and for Ne films adsorbed on two Kr overlayers (pink and purple data). At a fixed a film coverage, measurements showed a general increase in the slip time with increasing the

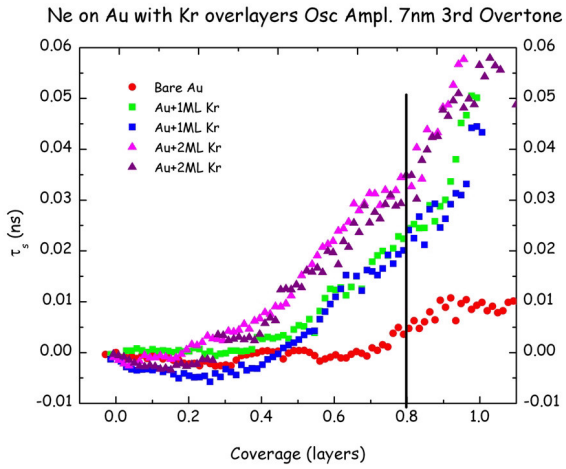

Figure 4.25: Calculated slip time for Ne adsorbed on bara gold (red points), on one monolayer (ML) of Kr (square points) and two ML of Kr (triangular points). An increase in the slip time increasing the Kr overlayer was observed.

insulating overlayer. This data trend suggested a total friction decrease increasing the Kr thickness. This behavior is consistent with a decrease in electronic friction on thick Kr overlayers caused by a shielding of the coupling between Ne adatoms and Pb surface electrones.

Kr layers were then adsorbed on the electrode and measurements on three and four Kr overlayers were acquired. Figure 4.26 summarized all data acquired for each Kr overlayer adsorbed. A reentrant behavior of the slip time at high Kr coverage was observed. To better show this behavior, fixed a surface coverage of $0,8 layers$ we have estrapolated the τ_s refers to the different Kr layers. Figure 4.27 summarized these data. The error bars refer to the maximum scatter for the related curves at this coverage. For two Kr overlayers τ_s reachs a value six times higher than that for the bare gold, decreasing slowly for the increase of the insulating overlayer to three and four monolayers.

The decrease of the slip time at high Kr coverages is not related to the electronic coupling with Ne atoms. I think that increasing Kr overlayers the local morphology changes reducing the atomic terraces over which Ne adatoms slip. Then, a reduction in the slip time accours.

These data are only preliminary and other measurements will be taken over new gold surfaces to better understand the interaction mechanisms involved between adatoms and gold substrate. In the future the coating with other insulators as Xe or N_2 will be studied, molecules with an higher polarizabilty than Kr. The aim is to evaluate different screaning systems.

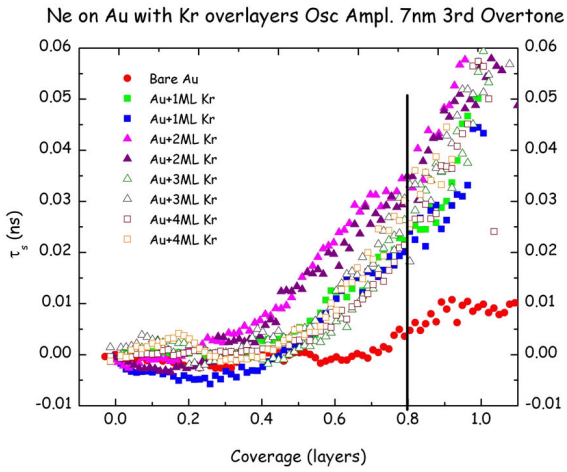

Figure 4.26: Calculated slip time for Ne adsorbe on 1, 2, 3 and monolayers of Kr.

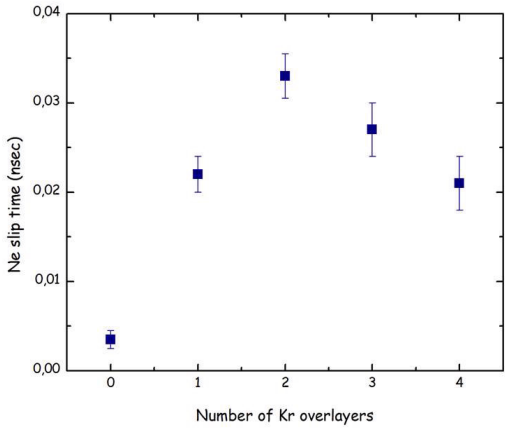

Figure 4.27: Calculated slip time for a $0,8 layers$ Ne film grown on increasing Kr overlayers.

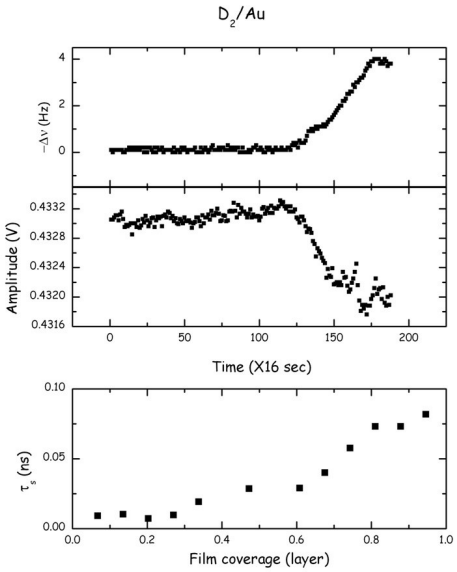

Figure 4.28: Raw data of the resonance frequency shift (top) and oscillation amplitude (middle) during an isothermal deposition of D_2 on Au. Bottom: calculated slip time as a function of D_2 film coverage.

4.10 Friction of deuterium monolayers on gold

Deuterium could be a good system to evaluate the electronic contribution across lead T_c because it has a critical temperature around the Ne critical temperature and it has a high polarizzability. On the other hands, makes it difficult for QCM measurements.

Our experimental set up coupled with the stability of the QCM used for the measurements allowed us to obtain a frequency stability of $0,1Hz$ on $15MHz$ and amplitude measurements with an accuracy better than $0,04\%$. The challenge was to take measurements with deuterium (D_2) films. To give an idea of the accuracy required with a $5MHz$ QCM the adsorption of one monolayer of D_2 causes the shift of $0,3Hz$ at the fundamental overtone, $0,9Hz$ at the third overtone ($15MHz$) and $1,3Hz$ at the fifth overtone ($25MHz$).

Data was taken at the fifth overtone of a $5MHz$ gold plated QCM at a frequency of $25MHz$, a quality factor of 500000 and an oscillation amplitude of 8 nm. Figure 4.28 show a run acquired at a $T = 5,80K$: it could be observed the very stable amplitude signal for the bare electrode with data scatter around the everage value of $\pm 0,2mV$. The amplitude total shift was $1,4mV$ on $430mV$. The calculated slip time plotted in the bottom graph show a slip time lower than $0,1ns$. Figure 4.29 summarized the calculated slip time for runs acquired in different days. Data were

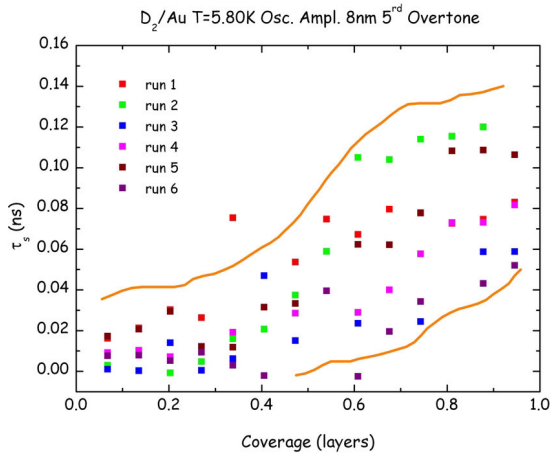

Figure 4.29: Calculated slip time for D_2 adsorbed on Au surface at $T = 5,80K$.

very noisy and a high scatter of data was visible. Nevertheless, there was a general increasing trend for slip time values suggesting that dissipation is taking place at the interface.

4.11 Diffusion of gold nanoparticles: preliminary studies

Recently, different experimental methods have been applied to study the diffusion of gold nanoparticles on graphite. AFM and TEM are the most useful[14] techniques to measure nanoparticles movements on a flat substrate. Very recently Pisov *et al*[18] proposed a QCM experiment to study this system.

In this section I show, preliminary data of the sliding friction of gold nanoparticles with a QCM technique. Gold nanoparticles were synthetized by Karine Mougin at the Institut de Chimie des Surfaces et Interface (ICSI-CNRS) of Mulhouse (France).

In the first sub-section, I show how we can estimate the diffusion coefficient D from slip time measurements; in the second I briefly describe the nanoparticles synthesis; in the last subsection I show some preliminary experimental measurements.

4.11.1 Estimate of the diffusion coefficient D by the slip time τ

Let us consider a gold cluster adsorbed on a flat substrate undergoing Brownian motion. When an adsorbate island or a cluster is forced to slide on a substrate, the

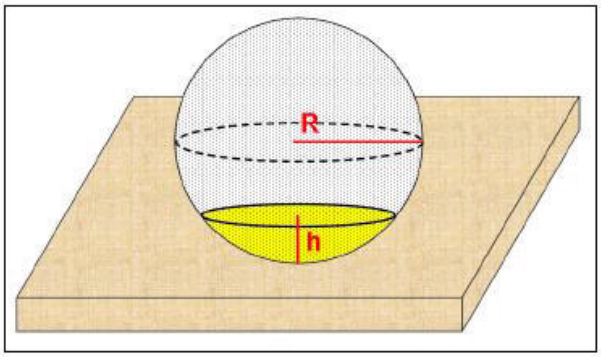

Figure 4.30: Simple model to describe a spheric nanoparticle on a flat substrate. h is the first neighbours interaction distance

dissipation of energy due to kinetic friction can be characterized by the slip time τ. This is a relaxation time associated with the cluster-momentum fluctuation and is connected to the interfacial friction coefficient η through the relation $\eta = \rho/\tau$, where ρ is the mass per unit area of the cluster. Thus, defining $\rho = m_{Au}N/A$ (N denotes here the number of gold atoms of the cluster in direct contact with the substrate over an area A), the interfacial friction coefficient can be rewritten as

$$\eta = \frac{m_{Au}N}{A\tau} \tag{4.6}$$

We can apply the fluctuation–dissipation theorem, which in turn causes the force-free diffusion and the friction under a sliding force to be connected through Einstein's relation,

$$D\eta A = k_B T \tag{4.7}$$

where T is the system temperature. By substituting expression 4.6 for the interfacial friction coefficient in 4.7, we obtain for the slip time

$$\tau = \frac{Dm_{Au}N}{k_B T} \tag{4.8}$$

We can then estimate the diffusion coefficient D by measuring the slip time for the clusters dissipation process. Assuming approximately $N = 50$ atoms directly touching the graphite substrate and, from the experimental data of Bardotti *et al* [14], a diffusion coefficient $D \sim 10^{-5} cm^2 s^{-1}$ for Au_{250} nanoclusters at $300K$, we get a rough estimate of the room temperature slip time, $\tau \sim 10^{-12} s$. While this value is at least two orders of magnitude too small to be observed by QCM, the situation, as discussed below, can change drastically upon heating[18].

With our experimental apparatus we can measure the slip time, but to calculate the diffusion coefficient D we need to know the number of atoms N in direct contact

with the substrate. There are various methods to estimate N. Being a feasibility study, we are only interested in the order of magnitude for N. Let us then consider clusters like perfect spheres. We assume that the cluster atoms in direct contact with the surface are those located on a spherical shell of height h, where h is the first neighbours interaction distance. A second approximation is to consider also gold atoms like perfect rigid spheres so the distance between two atoms is $2R_0$, with R_0 atomic radius. With these assumptions, for a sphere of radius R the spherical shell surface, S_c, with height h is:

$$S_c = 2\pi Rh$$

The number of atom in direct contact is then:

$$N' = \frac{S_c}{S_{atom}} = \frac{2\pi Rh}{\pi R_0^2} \tag{4.9}$$

For our experiment, we used gold nanoparticles of diameter $15nm$. Substituing in 4.9 the gold parameters, $h = 0,27nm$ and $R_0 = 0,179nm$ we obtain: $N' \simeq 130$. Known N' and measuring τ it is therefore possible to estimate the diffusion coefficient D.

4.11.2 Gold nanoparticles synthesis

The colloidal suspension used was an aqueous solution of tetrachloroauric(III)acid hydrate ([HAuCl4]·H2O), stabilized with citric acid trisodium. The concentrations of [HAuCl4]·H2O and citric acid trisodium in the final suspension were, respectively, $0,03$ and $0,02$ $wt.\%$, for a pH of $6,5$[62]. By reducing HAuCl4 with trisodium citrate, stabilized Au nanoparticles, which bear the negative charge of the citrate ions, are obtained. The average size of these particles, as determined from TEM images, was $12 \pm 5nm$ (see figure 4.31).

4.11.3 Friction measurements of gold nanoparticles on gold

The diffusion coefficient for gold on graphite estimated by recent simulations suggests an energy dissipation detectable with our apparatus. Actually, with our experimental set up it is impossible to deposit nanoparticles (NPs) in situ under UHV conditions because, as I said in the former section, gold NPs form a colloidal suspension in water. In this preliminary study, our goal was to evaluate the order of magnitude of the gold NPs friction on a gold flat surface. The study consisted in the measurements of the Q-factor variation of the QCM after the deposition of the gold nanoparticles on the metallic electrode. Influence of temperature and surface roughness are further studied.

Gold NPs were deposited on the QCM gold plate by simply putting a drop of solution on the Au plate and waiting for solvent evaporation. QCM must be

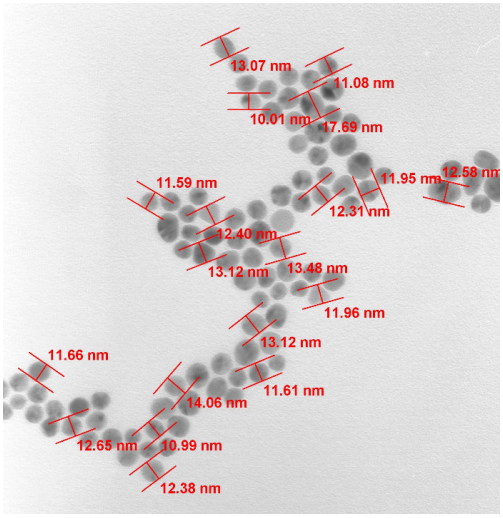

Figure 4.31: TEM image of gold nanoparticles suspended in water solution used in our measurements. The image shows a size distribution around the value of $12nm$.

extracted by UVH environment to deposite the NPs on the electrode. In this phase the gold surface is exposed to ambient air and surface cleaness is not guaranteed. Furthemore, this procedure may significantly affects the QCM measurement sin the sense that the extraction and the reinsertion of the QCM in the sample holder could change the electrical contact conditions. Then, we have repeated the Q-factor measurements extracting and reinserting the QCM from the sample holder to evaluate the reproducibility of data.

Figure 4.32 shows a typical resonance curve: the oscillation amplitude at different frequencies and at a fixed excitation amplitude is plotted. The Q-factor of the microbalance could be calculated interpolating the resonance curve data with:

$$y = \frac{\left(1 + (1 - \frac{x}{f_0})Q_p\right)^2 + \left(\frac{Qp}{2Q_s}\right)^2}{R_s^2\left(1 + (2Q_s(1 - \frac{x}{f_0})^2\right)}$$

where Q_s is the quality factor, Q_p is the antiresonance quality factor, R_s is the resistive component of the quartz impedance and f_0 is the resonance frequency of QCM. Q_s, Q_p and R_s are free parameters for the interpolation.

Data have been acquired at the first and third overtone of a $5MHz$ quartz plate with gold electrodes. The quartz was inserted in the sample holder and then we acquired a resonance curve at the first and third overtones. We then extracted the QCM from the sample holder and reinserted to acquire two new frequency scans. We repeated a few times this proceedure to evaluate the data reproducibility.

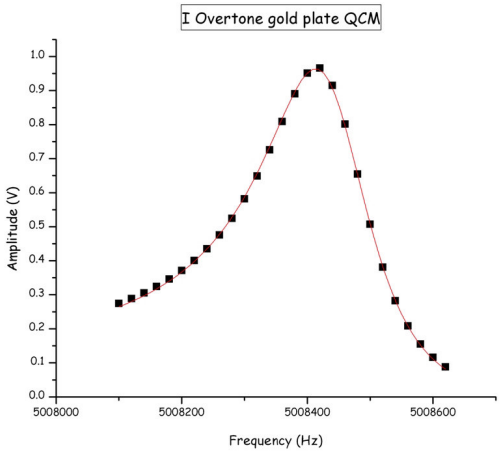

Figure 4.32: Fundamental resonance of a quartz microbalance with gold electrodes located around $5MHz$.

T (K)	Overtone	V_{exc} (mV)	Resonance frequency (Hz)	Q_s
Room	I	14	5008425	16000
Room	I	14	5008415	14000
Room	I	14	5008460	15000
Room	I	14	5008480	14000
Room	I	14	5008480	16000
Room	III	7	14978625	80000
Room	III	7	14978616	81000
Room	III	7	14978891	85000
Room	III	7	14978934	84000

Table 4.1: Data acquired at room temperature for the bare gold QCM.

The table 4.1 shows data acquired at room temperature. Changes in the resonance frequency value were detected of $\sim 60Hz$ at the first overtone and of $\sim 300Hz$ at the third overtone. These variations are a few percent of the estimated shift for the deposition of one monolayer of nanoparticles, corrections that can be negleted remembering that this is a feasibility study. The calculated Q-factors are in good agreement both for measurements taken at the first overtone and for those taken at the third.

We also took measurements at temperature T $\sim 5,5K$. At this temoerature to extract QCM from sample holder, means to heat the sample at room temperature in a few minutes. Quartz was submitted to thermical stresses, and it was necessary to better evaluate data reproducibility.

T (K)	Overtone	V_{exc} (mV)	Resonance frequency (Hz)	Q_s
5,4	I	6	5003013	50000
5,4	I	4	5003009	55000
5,4	I	5	5002993	50000
5,4	I	5	5002987	52000
5,4	III	5	14960510	140000
5,4	III	3	14960449	247000
5,4	III	3	14960401	210000

Table 4.2: Data acquired at cryogenic temperature for the bare gold.

T (K)	Overtone	V_{exc} (mV)	Resonance frequency (Hz)	Q_s
Room	I	40	5008149	9000
Room	I	32	5008142	11000
Room	I	26	5008194	10000
Room	III	14	14977981	19000
Room	III	14	14977946	17000
Room	III	14	14977714	24000

Table 4.3: Data acquired at room temperature for gold nanoparticles deposited on gold.

Data are shown in table 4.2: also for these data the resonance frequency values measured after each reinsertion show differences of a few tens of Hz at both overtones. The quality factors, instead, are increased by a factor of 3 for both the overtones. This is due to temperature: at cryogenic temperatures, QCM usually has a high quality factor.

The QCM was extracted from the UHV chamber and a drop of colloidal suspension of $\sim 15nm$ gold nanoparticles on water was put on the gold electrode. The QCM was reinserted in the chamber.

The table 4.3 shows data acquired at room temperature for the frequency scans acquired as explained before. The comparison with data taken with the bare QCM reveals a decrease in the resonance frequency due to the increase of the system total mass. The quality factor is also decreased for both the overtones, indicating that dissipation occurs between the nanoparticles and the gold surface.

Similar behavior was unexpectedly observed also at $5,5K$ (see table 4.4).

The figure 4.33 summarizes data acquired at room temperature at the first and the third overtone. Changes due to the presence of nanoparticles on the surface are underlined by the arrows. A total shift in the resonance frequency of $\Delta f \sim 300Hz$ is detected after the nanoparticles deposition at the fundamental resonance. A correspondent shift in the quality factor of $\Delta Q \sim 5000$ is found. At the third overtone we have measured a shift in the frequency of $\Delta f \sim 700Hz$ and in the

T (K)	Overtone	V_{exc} (mV)	Resonance frequency (Hz)	Q_s
5,4	I	10	5002619,7	30000
5,4	I	10	5002734,4	34000
5,4	III	10	14959281,5	90000
5,4	III	13	14959766,9	26000

Table 4.4: Data acquired at cryogenic temperature for gold nanoparticles deposited on gold.

quality factor $\Delta Q \sim 60000$. With these data we can estimate the slip time of the nanoparticles on the gold surface. By using the formula:

$$\tau_s = -\frac{\Delta\left(\frac{1}{Q}\right)}{\Delta f} = -\frac{\frac{1}{Q_0} - \frac{1}{Q}}{f_0 - f} \tag{4.10}$$

where the 0 indicates data for the QCM without deposited nanoparticles.

The averaged values for resonance frequency and Q-factor at room temperature are summarized in the following table:

Overtone	Resonance frequency (Hz)	Q
No nanoparticles		
I	5008452	15000
III	14978767	83000
With nanoparticles		
I	5008162	10000
III	14977880	20000

Substituting these values in the 4.10 we obtain:

$$\begin{aligned} \tau_{s\ I-RT} &\sim 120ns \\ \tau_{s\ III-RT} &\sim 36ns \end{aligned}$$

Figure 4.34 shows data acquired at $T = 5,5K$, and again, the vertical arrows indicate the frequency shift of $\Delta f \sim 400Hz$ and the corresponding Q-factor variation $\Delta Q \sim 20000$ at the first overtone due to the nanoparticles deposition. At the third overtone the shifts are $\Delta f \sim 800Hz$ and $\Delta Q \sim 140000$. The averaged values for resonance frequency and Q-factor at $5,5K$ are:

Overtone	Resonance frequency (Hz)	Q
No nanoparticles		
I	5003039	55000
III	14960453	199000
With nanoparticles		
I	5002677	32000
III	14959524	58000

The calculated slip times at the low temperature are:

$$\begin{aligned} \tau_{s\ I-LT} &\sim 42ns \\ \tau_{s\ III-LT} &\sim 14ns \end{aligned}$$

Decreasing the temperature there is a reduction of the slip time by a factor ~ 3 both at the fundamental and at the third overtone. The dissipation observed at low temperature was unexpected: at such low T: we originally believed that the clusters were locked at the surface. Of course, further experiments are necessary to better elucidate this point.

To estimate the influence of surface roughness on the friction we have taken some measurements with a QCM with rough gold electrodes. The same colloidal suspension of gold nanoparticle described above has been used to deposit the gold nanoparticles. The table 4.5 summarizes data for the frequency scans acquired at room and cryogenic temperatures of a $3MHz$ quartz plate at its fundamental overtone. The Q-factor values have some scatter but they are of the same order of magnitude at the two temperatures.

The QCM was then extracted, a drop of the nanoparticles water suspension was deposited on the gold electrode, and then the QCM was reinserted in the UHV chamber. The table 4.6 show all measurements taken at room temperature and at the first QCM overtone.

A few scans were characterized by a small Q-factor, but in general the calculated quality factor had values of the same order of magnitude of those calculated for the bare gold electrode. Figure 4.35 shows a summary of these data. We can see that the nanoparticles deposition involves a decrease of the resonance frequency but the quality factor is a bit smaller than that observed for bare gold. This means a low dissipation at the interface. Only three scans show quality factors $\sim$3 times smaller than the others.

Table 4.6 reports the quality factor measured with $3MHz$ QCM with rough gold electrodes covered by gold nanoparticles. Data incicates an increased dissipation at higher amplitudes. To check whether there exists a threshold amplitude below which

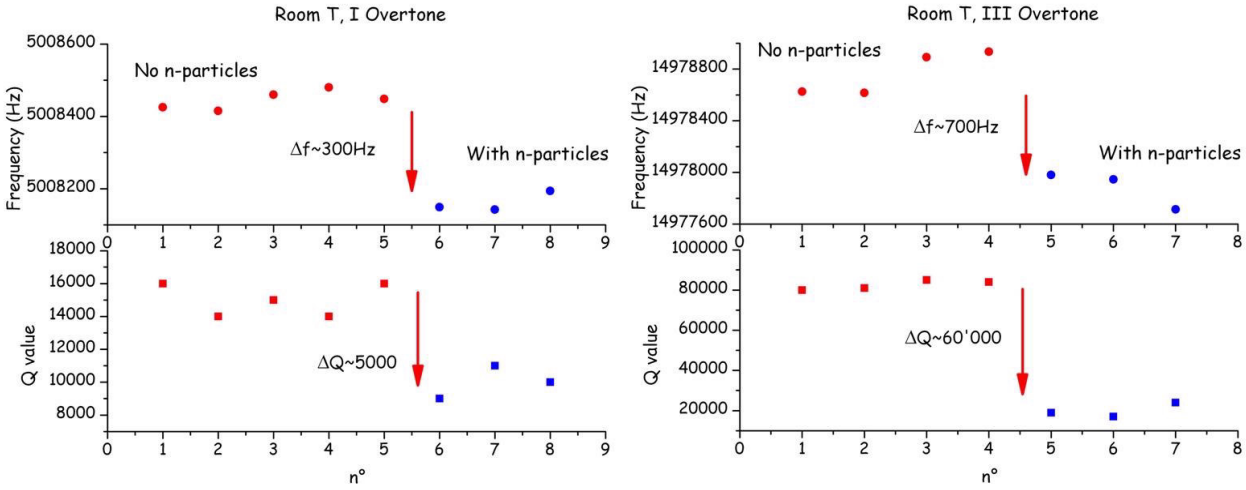

Figure 4.33: Measurements taken at room temperature at the first (left) and third (right) overtone of a QCM with flat gold electrodes. Measured resonance frequency and calculated quality factor are ploted for the bare gold (red points) and the gold coated with nanoparticles.

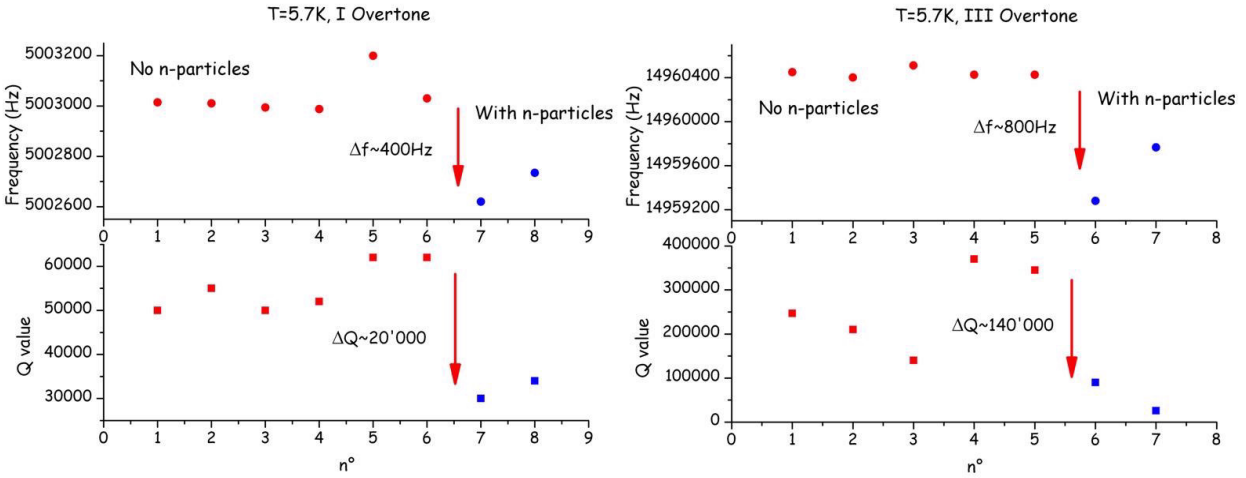

Figure 4.34: Measurements taken at cryogenic ($T = 5,5K$) temperature at the first (left) and third (right) overtone of a QCM with flat gold electrodes. Measured resonance frequency and calculated quality factor are ploted for the bare gold (red points) and the gold coated with nanoparticles.

T (K)	Overtone	V_{exc} (mV)	Resonance frequency (Hz)	Q_s
Room	I	4	2999793	320000
Room	I	4	2999795	320000
Room	I	4	2999795	330000
Room	I	4	2999784	270000
Room	I	4	2999789	250000
Room	I	4	2999787	300000
Room	I	4	2999786	270000
5,4	I	3	2996657	380000
5,4	I	4	2996620	200000
5,4	I	3	2996661	290000
5,4	I	4	2996663	270000
5,4	I	2	2996657	590000

Table 4.5: Data acquired at room and cryogenic (T=5,4K) temperature at the fundamental overtone of a 3MHz quartz with rough gold electrodes.

the nanoparticles are stark to the gold surface, we took an isothermal amplitude scan by changing the excitation voltage from $100mV$ to $1000mV$ by steps of $100mV$. Figure 4.36 shows the measured oscillation amplitude, related to the Q value, as a function of the driving applied voltage. We can see a quite perfect linearity in the data without any change due to jumps or changes in the slope. Data suggest that if an amplitude threshold exists it is below the $100mV$ of excitation. Unfortunaely, a scan in the range $30 - 100mV$ was not possible for limits in the amplifier used for measurements.

Although this is a very preliminary work, I summarize the main results of the study of nanoparticles on a rough gold substrate in the next table:

T (K)	Overtone	V_{exc} (mV)	Resonance frequency (Hz)	Q_s
Room	I	4	2999257	280000
Room	I	4	2999258	280000
Room	I	1000	2999269	71000
Room	I	5	2999255	200000
Room	I	5	2999257	200000
Room	I	32	2999258	210000
Room	I	28	2999259	240000
Room	I	600	2999265	98000
Room	I	800	2999265	90000

Table 4.6: Data acquired at room temperature at the fundamental overtone of a 3MHz quartz with rough gold electrodes coated by gold nanoparticles.

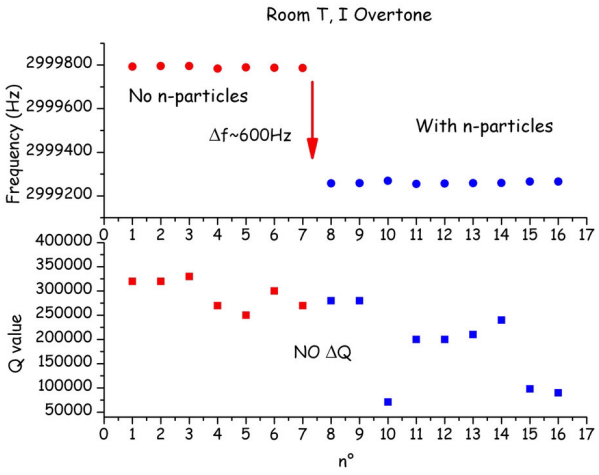

Figure 4.35: Measurements taken at room temperature at thefundamental overtone of a QCM with rough gold electrodes. Measured resonance frequency and calculated quality factor are ploted for the bare gold (red points) and the gold coated with nanoparticles.

System	Resonance frequency (Hz)	Q
Low excitation		
No nPs	2999795	295000
With nPs	2999257	235000
High excitation		
No nPs	2999795	295000
With nPs	2999265	85000

The calculated slip times for rough substrate are:

$$\tau_{s\ I-LV} \sim 1,6ns$$
$$\tau_{s\ I-HV} \sim 15ns$$

The everage roughness of the electrodes surface was measured with the Atomic Force Microscope (AFM)[2]. In contact regime, topographic scans were acquired in different points of the electrode. In figure 4.37 a 3D picture of a $10 \times 10\mu m^2$ is shown. Images have been analized with the software $IP2.1$ of ThermoMicroscopes©. Topography reveals average roughnesses ranging from 60 to $350nm$ depends on the

[2]For measurements an in air AFM *Autoprobe CP-I* purchased from Park Scientific Instruments was used with an Ultrasharp *CSC* 21/50 tip purchased from Silicon-MDT.

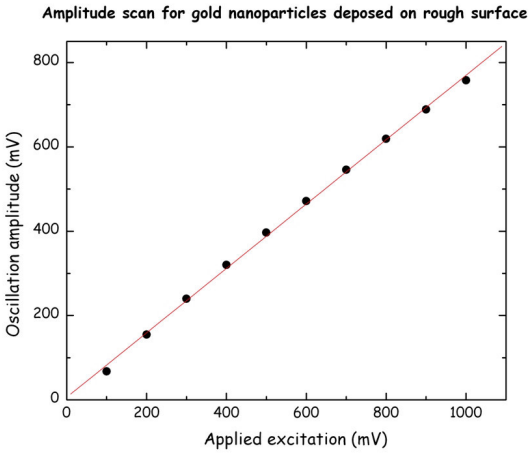

Figure 4.36: Amplitude scan for gold nanoparticles deposed on rough gold surface.

region analized, with a few small regions characterized by an average roughness of $\sim 25nm$. The software calculates the everage roughness by the formula:

$$R_{rms} = \sqrt{\sum_{n=1}^{N} \frac{(z_n - \overline{z})^2}{N-1}}$$

where N is the total pixel number and $\overline{z}$ is the average height.

To better understand mechanisms involved in this process a deep study of the surface morphology is necessary combined with theoretical calculations.

4.11.4 Diffusion coefficient

We can provide an estimate of the slip times deduced from our experimental data.

First of all let us calculate the number of gold atoms per nanoparticle. We need some constant for the calculus:

$\rho_{Au} = 19300\,\mathrm{kg/\,m^3}$	*Gold density*
$P_a = 196,96\,\mathrm{g/\,mol}$	*Gold molar mass*
$R = 7,5\,\mathrm{nm}$	*Average radius of nanoparticles*
$S = 1,963 \cdot 10^{-5}\,\mathrm{m^2}$	*Electrode surface*
$Z_q = 8,862 \cdot 10^6\,\mathrm{kg/\,m^2 \cdot\,s}$	*Quartz acoustic impedance*

In the approximation of spherical nanoparticles, the mass could be easily calculated:

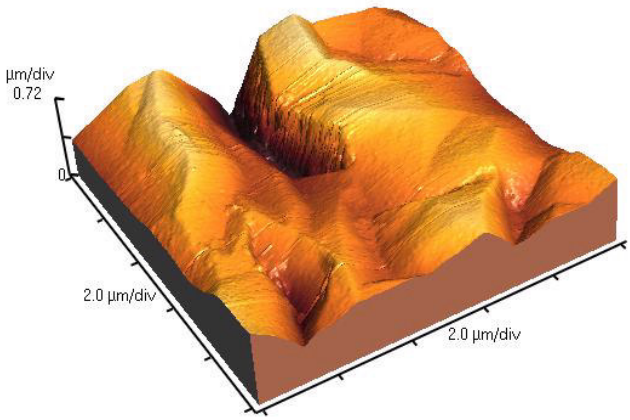

Figure 4.37: 3-D picture of a contact AFM scan taken on the rough gold surface.

$$M = \rho_{Au}\frac{4}{3}\pi R^3 \cong 3,41 \cdot 10^{-20}\,\mathrm{kg} \tag{4.11}$$

and the number of atoms per particle:

$$n = M\frac{A}{P_a} \simeq 10^5 atoms \tag{4.12}$$

where A is the Avogadro number.

We could also give an estimation of the nanoparticles deposited on the surface. Let us consider the first overtone with a resonance frequency of 5 MHz. The frequency shift due to the adsorption of one gold nanoparticle is:

$$\Delta f_{np} = \frac{4f_0^2 M}{Z_q S} \simeq 2 \cdot 10^{-8}\,\mathrm{Hz}$$

where f_0 is the resonance frequency. Considering an everage total resonance frequency shift due to the adsorption of nanoparticles $\Delta f_{tot} = 300\,\mathrm{Hz}$, the total number of nanoparticles deposited N_{NPs} on surface is:

$$N_{NPs} = \frac{\Delta f_{tot}}{\Delta f_{np}} \simeq 1,5 \cdot 10^{10}$$

All these data are necessary to calculate the interfacial friction coefficient η from 4.6:

$$\eta = \frac{m_{Au}N}{S\tau} \simeq 0,66\frac{\mathrm{kg}}{\mathrm{m^2\,s}}$$

where N denotes the number of gold atoms of the cluster in direct contact with the substrate over an area S, $m_{Au} = 3,3 \cdot 10^{-25}\,\mathrm{kg}$ is the gold atomic mass and $N = N_{NPs} \cdot N' = 1,95 \cdot 10^{12} atoms$ (see 4.9). From 4.8 it is easy now to calculate the diffusion coefficient:

$$D = \frac{k_B T \tau}{m_{Au} N} \simeq 4,8 \cdot 10^{-6} \frac{\mathrm{m}^2}{\mathrm{s}} = 4,8 \cdot 10^{-2} \frac{\mathrm{cm}^2}{\mathrm{s}}$$

The diffusion coefficient is three orders of magnitude higher than that measured by Bardotti *et al.*[14]. Clusters studied by Bardotti *et al.* had about 250 atoms while our nanoparticles have about 10^5 atoms and substrate was graphite. Our work is a preliminary study and data are only indicative. For a better comparison with theory, further experiments and calculations are necessary.

Measurements taken on a flat surface show very interesting results. At cryogenic temperature the detection of slippage was unexpected. Calculated slip times at T of $5,4K$ are only three times lower than those at room temperature. If the external excitation is the same for the two temperatures, the force applied to each nanoparticle is the same. Contaminants are not present on the surface at low temperature because QCM are housed in a UHV environment. This results is in stark contrast with the prediction of a thermally activated process[18]. If thiese preliminary studies will be confirmed by further measurements, they may suggest that the cluster is incommensurate with the surface.

Data acquired on the rough surface at room temperature show two different regimes: at low voltage a very small dissipation occurs and at high voltage a slippage was detected. The calculated slip time at high external excitation is one order of magnituder lower than for the flat surface and the amplitude scan did not reveal any critical oscillation amplitude for starting slippage. The everage surface roughness is higher than nanoparticle dimension.

In any case, it is worth to stress that all these data on nanoparticles are preliminary. Other measurements are necessary to better understand the temperature influence on the nanoparticles sliding on flat substrate. Furthemore, it would very interesting to investigate the dependence of nanoparticles friction oh the lateral force and on substrate roughness.

An up-grade of our experimental set up is in progress to allow dosing nanoparticles directly in UHV chamber to better control the surface cleaness and nanoparticles deposition without the need to extract the QCM. Systematic study is planned for the near future.

Chapter 5

Friction on micropatterned surfaces

In this chapter I show preliminary studies on the frictional properties of silicon surfaces coated with Self Assembled Monolayers of alkylsilane. Samples have been prepared by Micro Contact Printing μCP and the frictional properties studied with the Atomic Force Microscope, AFM. Unfortunately the breaking of the AFM did not allow us to do a sistematic study. In the first section I will describe the sample preparation procedure developed to prepare samples working "in air". The characterization with AFM and the water contact angle will be also shown. In the last section preliminary data of the tribological properties will be presented.

5.1 Microcontact printing of alkylsilane on silicon

Silicon masters used for these studies have been realized at the TASC laboratory[1] in Trieste with photolitographic tecniques described in the section 3.1. The patterns obtained were characterized by rectangular wells and cylindrical pillars with different sizes and steps. The patterned area was $2 \times 2\,\mathrm{cm}^2$.

Silicon masters were cleaned in *Piranha* solution and then silanized evaporating *Octadecyltrichlorosilane* ($C_{18}H_{37}SiCl_3$, OTS) directly on the silicon surface for 30 minutes. 160μl of OTS were put on a aluminum plate inside an evaporator. The silicon master were suspended about 2 cm over the OTS and a vacuum of $\sim 10^{-1}$ atm was done by a rotary pump. The first reaction is the completely hydrolysis of the OTS molecule, resulting in the formation of 3 HCl and the trisilanol form of OTS. Subsequently, water elimination reactions result in Si–O–Si linkages between adjacent OTS molecules and/or the oxidized substrate (figure 5.1). HCl produced in the reaction was prevent to damage the pump by a liquid nitrogen trap.

[1] I thank Alessandro Pozzato and Simone dal Zilio for the help in the masters realization.

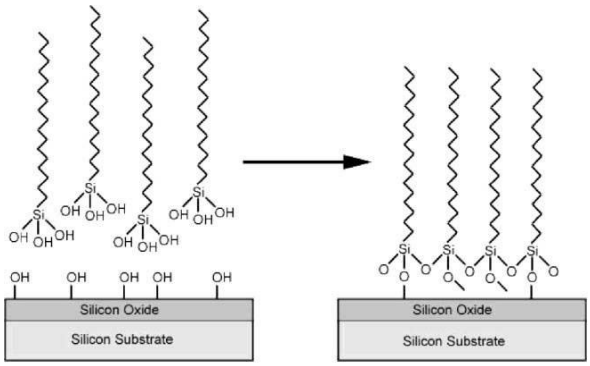

Figure 5.1: A simplified diagram of the formation of an OTS monolayer.

PDMS patterns were fabricated by Replica Molding (ReM). A prepolymer of the elastomer (the monomer mixed with the catalyst) is poured over, then cured and peeled off. In this way we obtained a negative of the original pattern. We also needed a PDMS microstructure identical to the silicon master. We then replicated the silicon microstructure on a thermoplastic polymer, the *Poly(methyl methacrylate)* (*PMMA*), via Hot Embossing. The glass transition temperature for PMMA is $120°C$. On the plate of a manual hydraulic press with heated plates (Specac) I put the silicon master with a PMMA square of side $\sim 1,5$ cm on the patterned area (see figure 5.2). A silanized flat silicon wafer is put between PMMA and the other plate to prevent the polymer adhesion. Two spacers guarantee the parallelism of the press plates. The imprinting is performed at a pressure of $\sim 1 ton/cm^2$ and a temperature of $T = 130°C$ for 15 minutes while the demolding is performed at room temperature. The microstructured PMMA forms a negative pattern with respect to the silicon master. Replicating the PMMA master with PDMS we obtain the starting silicon pattern.

Figure 5.3 shows the Scanning Electron Microscope (SEM) images of two silicon masters used for this work. To name the different masters I will use a label in the following form: a letter indicating the pattern type, l for the rectangular wells, p for cilindrical pillars and d for cilindrical dots; a number indicating the microstructures width, expressed in μm, and a second number indicating the microstructures periodicity, againg in μm. For example the label $p4/8$ indicates a pattern of pillars with diameter $4\mu m$ and periodicity $8\mu m$. Sizes are refered to the photolithographic mask. All the silicon structures have an height of $\sim 3\mu m$. Table 5.1 summarized patterns employed:

Samples have been prepared by μCP of alkylsilane on silicon surfaces. Two different alkylsilane were used: the OTS described above and the *eptadecafluorine 1,1,2,2 tetrahydro decyldimethilchlorosilane* ($SIH_{5840,4}$), a silane with seventeen fluorines in its chain. A SAM of fluorinated molecules has usually an high hydro-

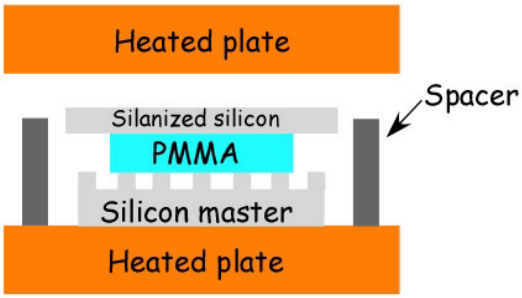

Figure 5.2: Schematic picture of the hot embossing procedure.

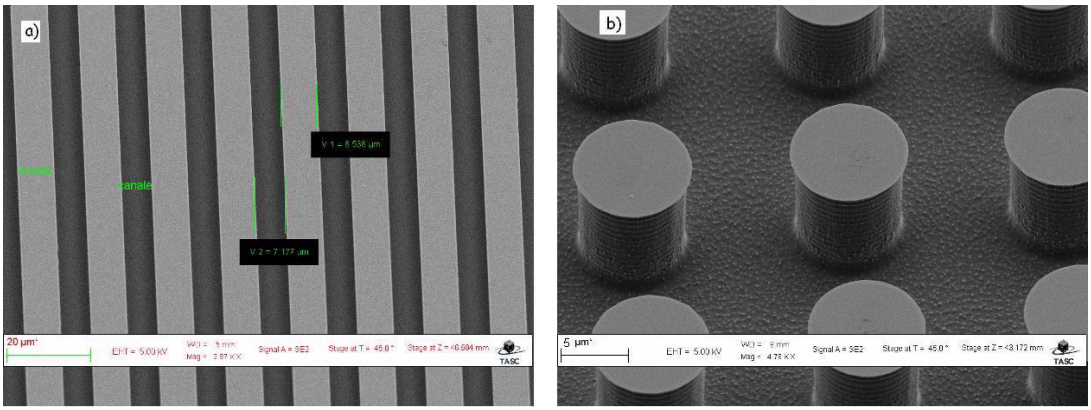

Figure 5.3: SEM images of a $l8/16$ (a) and a $p8/16$ (b) silicon masters.

$l3/6$	$l3/11$	$l4/8$
$l8/10$	$l16/20$	$p4/8$
$p8/16$	$d4/8$	$d8/16$

Table 5.1: Silicon patterns used for the PDMS replica molding.

phobicity. Alkylsilanes are very reactive with water hydrolysing together; the air humidity is enough to form oligomers that could prevent a perfect SAM formation. All glasses have been heated at $T > 100°C$ to remove water and solutions were maintained in Schlenk tubes. A Schlenk tube is a reaction vessel with a cap and a side arm fitted with a teflon stopcock which allows the vessel to be evacuated or filled with gases. The cap has an hole and a separator to withdraw the solution through a siringe. Solutions were used over a few hours from their preparation.

$5mM$ solutions in toluene and normal-exane of both alkylsilane have been used like ink. A drop of ink solution was placed onto a PDMS stamp for a duration of $30s$. The ink solution was then removed under a stream of nitrogen and the stamp pressed by fingers on the silicon surface for $25 - 30\,\mathrm{s}$. Silicon was previously cleaned in the piranha solution to oxidized the substrate. The resulting patterned silicon was finally cleaned with the solvent and dry with nitrogen.

Samples were analized with the AFM working both in topography and in lateral force. For measurements in air, an AFM *Autoprobe CP-I* purchased from Park Scientific Instruments was used with an Ultrasharp CSC 21/50 tip purchased from Silicon-MDT. The tip has a curvature radius $\leq 10nm$, a height of $15 \div 20\mu m$, a cone angle lower than 20° and an elastic constant $\simeq 0,12\,\mathrm{N/m}$. Figure 5.4 shows a 3D topographic picture of the three kinds of microstructures realized: lines, pillars and dots. The clear areas are coated by the SAM.

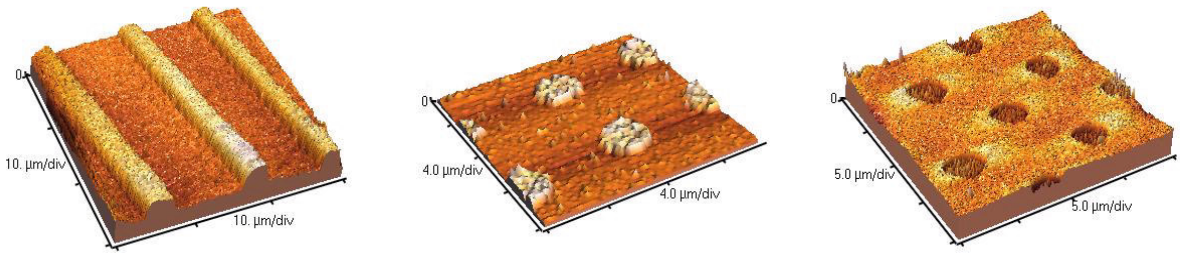

Figure 5.4: AFM topographical pictures of the printed structures: lines, pilars and dots.

The AFM analysis help us to understand problems related to sample preparation and characterization. The pattern reproduced on the silicon surface can be different from the nominal one. A long wet ecthing of the chromium mask on the silicon, during the silicon master preparation, broadens the width of microstructures. A

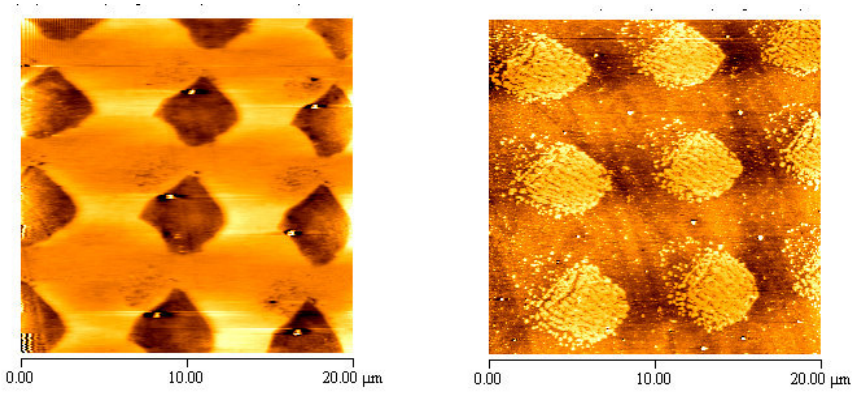

Figure 5.5: AFM topographical images of deformed PDMS stamp: left, patterned dots and right pillars.

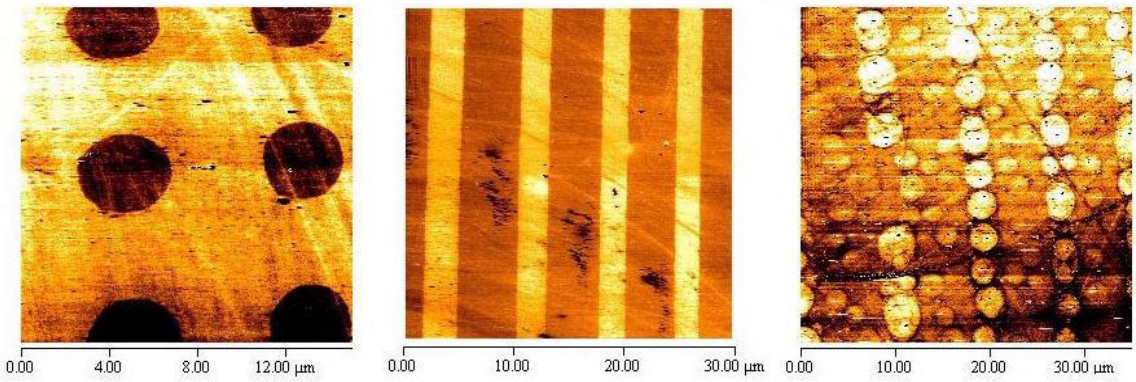

Figure 5.6: Microstructures produced with μCP of a solution of SIH in n-exane: left and middle, two well defined structures; right, diffusion of silane.

non perfect silanization of the silicon master could produce a deformation of the structures detaching the PMMA stamp. Figure 5.5 shows the topography images of silicon printed with a PDMS stamp structured with dots (left) and pillars (right). Reproduced structures show a well defined orientation caused by to an invalid separation between the structured silicon and the molded PMMA.

The picture on the right in fig. 5.5 shows also a no well defined border. Small islands of SAM diffused outside the printed area. Molecules evaporate from the PDMS stamp, react with humidity forming oligomers that attach on the substrate. The OTS, having three chlorines in its molecule, is more reactive than the SIH. In fact SIH patterns showed more defined borders than OTS. Nevertheless SIH is more volatile than OTS and the solution drop should be placed on the PDMS stamp for a small time. Figure 5.6 shows samples realized printing a SIH solution in n-exane: from left to right, two well defined structures and a pattern with big SAM aggregate,

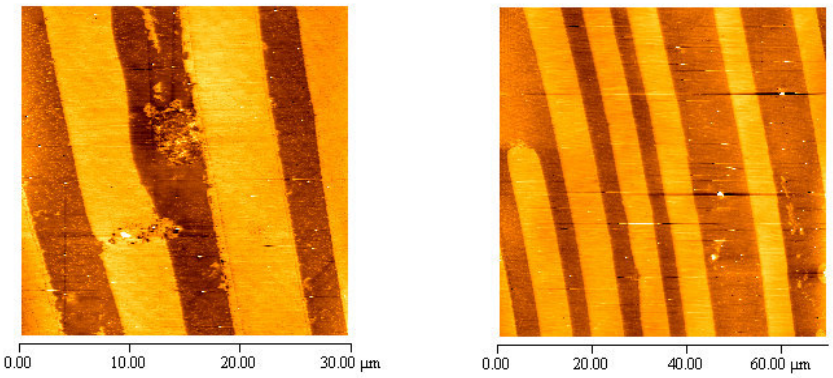

Figure 5.7: Patterns defects due to a non uniform PDMS stamp.

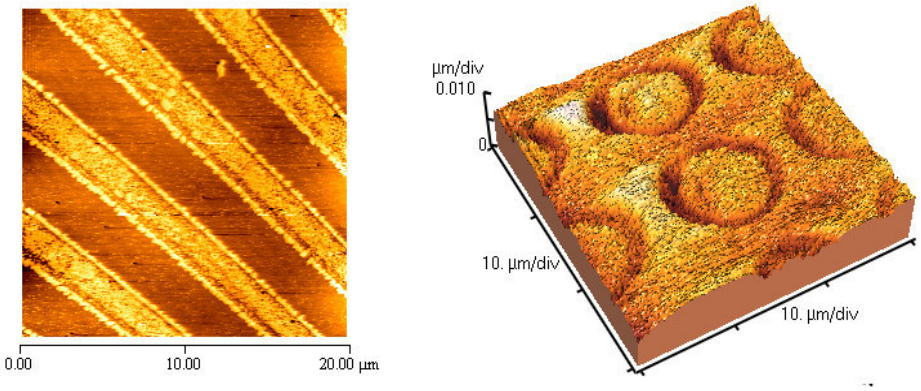

Figure 5.8: Pattern defects due to an high pressure on the stamp.

the printed pattern was $l4/8$.

Other problems were related to a bad PDMS stamp realization. Figure 5.7 shows two AFM images of patterns having different periodicity in the same pattern, an imperfect borders linearity and lines ending suddenly.

A high pressure on the PDMS stamp can cause the bottom collapse of the microstructure. This is most evident for large structures. Figure 5.8 shows on the left a line structure with two borders, an high pressure has caused the wall bending; the image on the right shows the bottom collapse of a dot microstructure, the dot diameter is $\sim 10\mu m$ while the depth is $\sim 3\mu m$.

The sample roughness has been estimated with contact AFM. Figure 5.9 shows a topographic image for an OTS patterned surface with a line scan underlines. The patterned area has an average roughness $\leq 1nm$, comparable with the silicon surface.

Patterned samples has been analyzed macroscopically by water contact angle

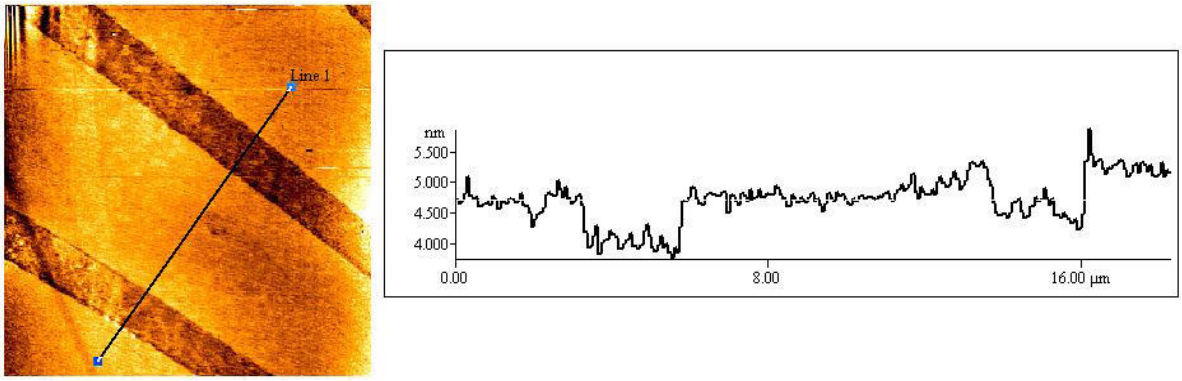

Figure 5.9: A topographical AFM image with underlined a line scan: we can see the low roughness of the patterned area.

measurements.

Let us consider a liquid drop put on a flat homogeneous surface. Its shape depends on the superficial tensions exerted at interfaces. The equilibrium state is well described by the Young equation: $\gamma_{sl} = \gamma_{sg} + \gamma_{\mathrm{lg}} \cos\theta$, where γ is the superficial tension, s, l and g indicate respectively solid, liquid and gas and θ is the contact angle between the solid substrate and the liquid. If the surface is chemically heterogeneous the Young equation does not give a well description of the system. Let f_i be the fractional area covered by the i-th domain with a contact angle θ_i. The average surface contact angle θ_m is:

$$\cos\theta_m = \sum_i f_i \cos\theta_i$$

named *Cassie law*. Our systems were formed by 2D patterns of two different chemical species: the silicon and the silane SAM. Tha Cassie law becomes: $\cos\theta = f_1 \cos\theta_1 + (1 - f_1)\cos\theta_2$, being θ_1 the contact angle for the silicon flat surface and θ_2 the contact angle for the silicon covered by a silane SAM. The Cassie model[63] describes exaustively surfaces chemically heterogeneous formed by domains chemically different.

Contact angles of water drops were measured with a home-built apparatus consisting of a motorized syringe pump, a video camera and motorized sample and camera stages controlled by a PC using a program written in Labview$^{\mathrm{TM}}$. Ultrapure water (Millipore) was used. The surface fraction coated by the SAM was deduced by the LFM images.

The homogeneous surface contact angles has been taken on bare silicon, cleaned by the piranha solution, and silicon coated by a uniform SAM. A silicon square was put in a $5mM$ solution of the silane for 24 hours. Table 5.2 shows the measured contact angles for homogeneous surfaces. The bare cleaned silicon showed immediately a very low contact angle due to the presence of $-OH$ groups on the surface.

Surface	$\boldsymbol{\theta}_C(^\circ)$
SAM OTS $_{Toluene}$	107 ± 4
SAM OTS $_{n-Exane}$	110 ± 1
SAM SIH $_{n-Exane}$	109 ± 4
Silicon	45 ± 6

Table 5.2: Contact angles measured for flat homogeneous surfaces

After a few days the contact angle stabilized at the value reported in the table. For each sample analized in this work I have taken more than five measurements in five different points.

Table 5.3 shows all data acquired: in the first row are reported surface patterns, in the second the ink and the solvent used in the printing process, in the third the surface fraction occupied by the silane SAM and evaluated directly in the AFM images, f_{2EXP}; the fourth shows the difference between the f_{2EXP} and the f_2 evaluated by the nominal master size; in the fifth the measured contact angles are presented and finally contact angles predicted by Cassie law, using the f_{2EXP} and the measured θ_1 for the silicon and θ_2 for the silane SAM. The f_{2EXP} errors arise from the method involved in the area determination. To analize images I used the $IP2.1$ software that permit to select image areas with height (for the topography) or voltage (for LFM) inside two boundary values. The error ascribed for f_2 is one half the difference between the excess and the defect value estimated for f_2. Errors ascribed to θ_{EXP} refer to one half of the maximum scatter for measurements taken. Finally, errors reported for the calculated θ_{CASSIE} were abtained propagating errors for each term in the Cassie law. Some discrepancies between experimental and theoretical angles arise from the f_2 evaluation. I took only a few AFM images for each sample, then the f_2 were estimated only for small sample regions. In our evaluation we have considered the surface coated by a homogeneous pattern.

Figure 5.10 summarizes all the contact angle measurements: the black points are the measured angles while red points are predictions by the Cassie law. We can see that experimental data are in good agreement, inside the error bars, with the theoretical values. Figure 5.11 shows the LFM images of all the patterns realized.

5.2 Tribological studies

Recently there has been a rapid development of MEMS. Systems dimensions do not allow to use standard lubricants to reduce friction and wear of the mobile parts. A possible strategy could be to cover the interface between mobile parts with a suitable SAM.

The aim of these studies was to investigate tribological properties of a patterned silicon surface. Unfortunately the breaking of the AFM did not allow us to do a

Pattern	**INK/solv**	$\mathbf{f}_{2EXP}(\%)$	$\mathbf{f}_{2EXP}-\mathbf{f}_{2NOM}(\%)$	$\theta_{EXP}(^\circ)$	$\theta_{CASSIE}(^\circ)$
l 8/10	OTS/es	71±4	-9	96±4	95±2
l 4/8	OTS/tol	45±5	-5	72±2	76±4
l 4/8	OTS/tol	41±6	-9	78±5	74±3
l 3/6	OTS/tol	63±4	+13	89±3	85±3
l 3/6	OTS/es	62±5	+12	84±7	85±2
l 3/6	OTS/tol	42±10	-8	78±4	72±4
l 3/11	OTS/es	37±2	10	67±5	70±3
l 3/11	OTS/es	25±5	-2	60±3	64±4
l 3/11	OTS/es	25±5	-2	58±3	64±4
l 16/20	OTS/es	83±7	+3	96±3	99±2
l 16/20	OTS/es	73±5	-7	92±3	93±2
p 8/16	OTS/es	20±5	0	58±3	60±1
p 8/4	OTS/es	20±5	0	59±3	60±1
p 8/4	OTS/es	20±5	0	65±4	60±1
p 8/4	OTS/es	17±5	-3	57±3	58±1
d 8/16	OTS/es	81±10	+1	96±2	98±3
d 8/16	OTS/es	82±4	+2	101±2	98±1
d 8/16	OTS/es	86±3	+6	96±2	101±1
d 8/16	OTS/es	84±4	+4	101±2	100±1
d 4/8	OTS/tol	86±5	+6	95±2	99±4
d 4/8	OTS/es	80±2	0	102±3	97±
d 4/8	OTS/tol	81±10	+1	97±6	96±5
d 4/8	OTS/es	90±2	+10	101±2	103±1
d 4/8	OTS/es	90±4	+10	102±3	103±1
d 4/8	OTS/tol	89±1	+9	93±8	101±4
d 4/8	OTS/es	85±2	+5	100±3	100±5
d 4/8	OTS/tol	87±3	+7	91±7	100±3

Table 5.3: Contact angle measurements for yhe patterns produced and all the ink solutions developed.

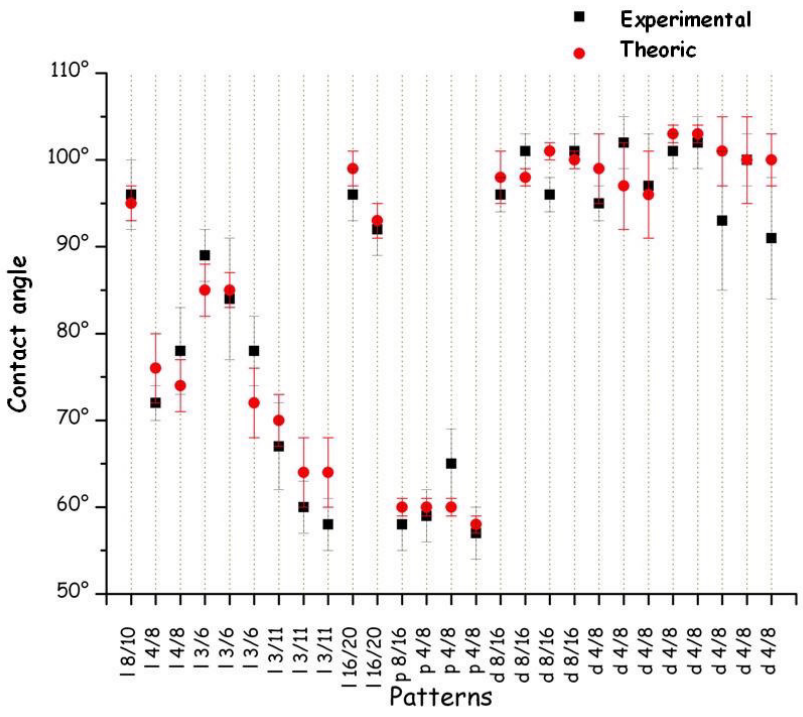

Figure 5.10: Summary of contact angles measured (red points) and calculated (black points) with the Cassie law for μCP samples of alkysilane on silicon.

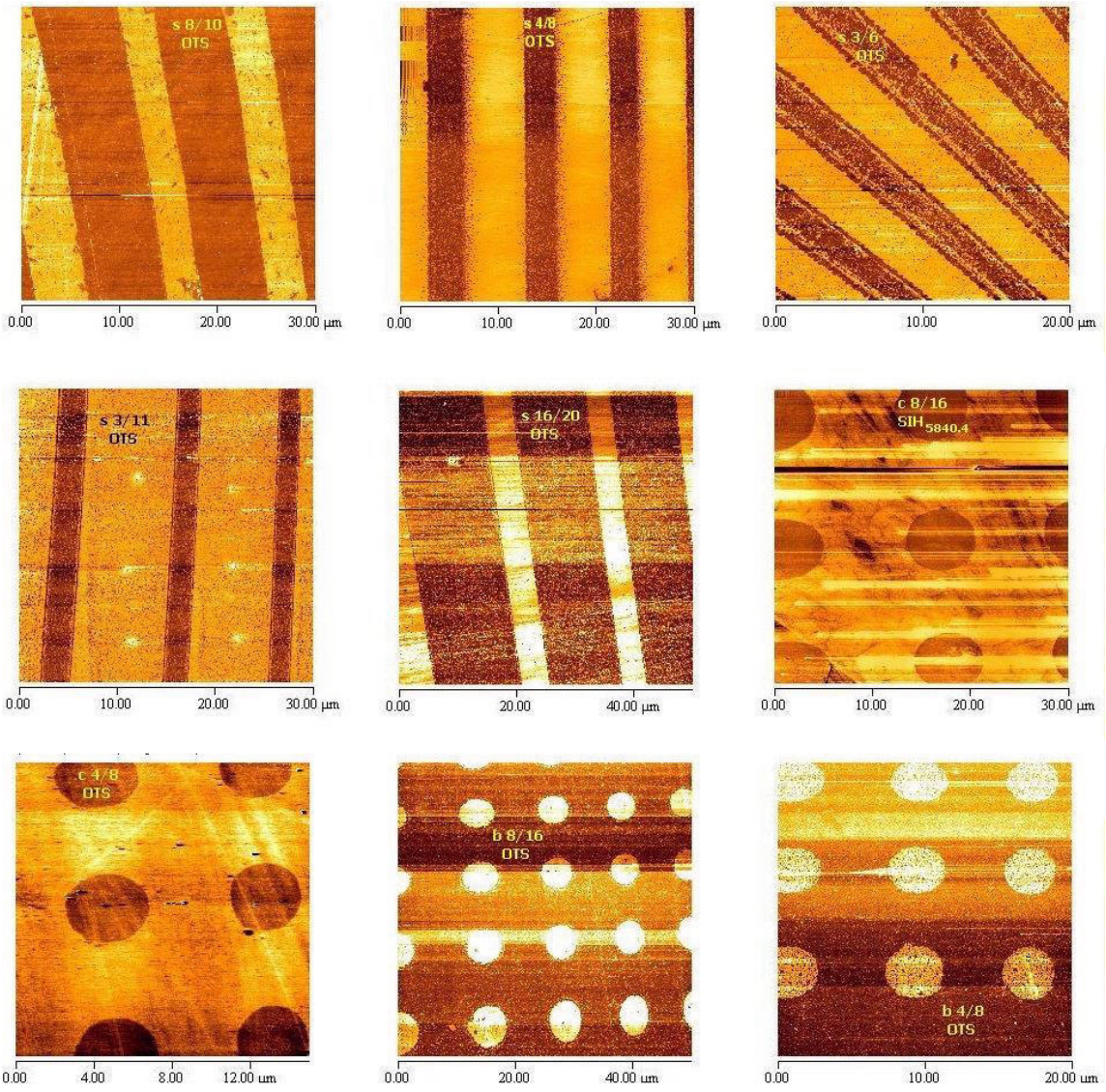

Figure 5.11: LFM images of prepared patterns.

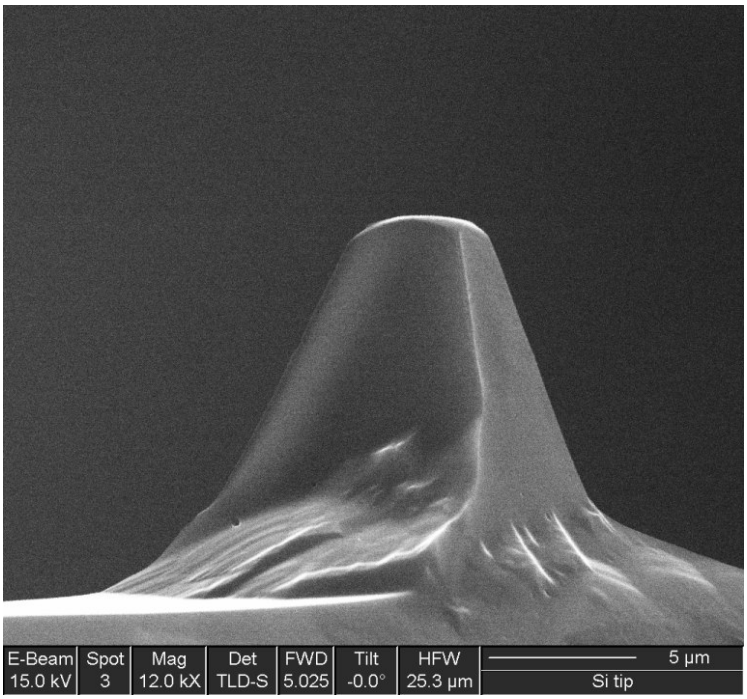

Figure 5.12: The SEM image of the scanning probe.

sistematic study. In this section I will show the preliminary measurements acquired with a modified AFM tip. The idea was to study chemical modification of silicon surface to reduce the friction. These measurements were taken in the SUP&RMAN laboratory sited at Physics department of the Modena and Reggio Emilia University[2].

A standard AFM probe has a tip with a curvature radius $\leq 10nm$ and its response gives local informations. On the other hand, a standard microtribometer acts over contact areas with diameters higher than $20\mu m$. To study the intermediate regime, in which many single parts of MEMS work, a good probe is a FIB modified AFM tip with a flat square of $\sim 2 \times 2\mu\,\mathrm{m}^2$. Figure 5.12 shows the SEM image of the square tip.

With our AFM a sample of OTS printed on silicon with a pattern $l8/16$ was initially studied. An AFM scan in topography and lateral force was done. Figure 5.13 shows the LFM scan of a $15 \times 15\mu\,\mathrm{m}^2$ area taken with an applied force of $6n\,\mathrm{N}$ and a frequency of $1\,\mathrm{Hz}$. The brown area indicates low friction and is the patterned surface with OTS while the orange area is the bare silicon. We can see a well defined patterned area but some little islands (brown spots) are present also on the non printed surface.

[2]Measurements were acquired with the help of Diego Marchetto.

Figure 5.13: $15 \times 15 \mu m^2$ LFM image acquired with our AFM on a OTS $l8/16$ pattern on silicon.

This sample has been analyzed with the AFM *Enviroscope* purchased by Digital Instruments by the Modena group. Lateral force scans were taken in different sample regions with the square tip. The scanned area was $15 \times 15 \mu\,\mathrm{m}^2$ with a frequency of $0,5\,\mathrm{Hz}$ and all images were acquired in trace (TR) and retrace (RETR). Scans were done decreasing the applied force every 25 acquired lines. The software driving the AFM did not permit us to set directly the applied load, we have set a tension and by the characteristc parameters of the cantilever we have calculated the corrispondent applied force. The applied tensions V_{app} were: 4 3 2 1 0 -0.4 -0.8 -1.2 -1.6 -2 -2.4 -2.8 -3.2 all values expressed in Volt. Positive values indicate a pressure of the tip while negative values indicate a retraction. Figure 5.14 shows the trace (a) and retrace (b) images taken during a scan. We can see that the images colors are opposite. Let α be the angle between the tip axis and the perpendicular to the surface on a trace scan. When the tip experiences a low friction region, the tip deflection is small giving a lower signal than for high friction region. When the tip comes back, the tilt tip angle changes its sign (from α to $-\alpha$). Then, for low friction regions the read signal is higher than for high friction region. LFM signal is then affects by the bending tip contribution that have opposite signs for trace and retrace scans. To obtain only the frictional contribution of the signal, we have filtered the images. The retrace signal is detracted by the trace one to reduce bending tip effects. The resulting image is shown in figure 5.15. This picture evidences a poorly defined border: the square tip, crossing the border

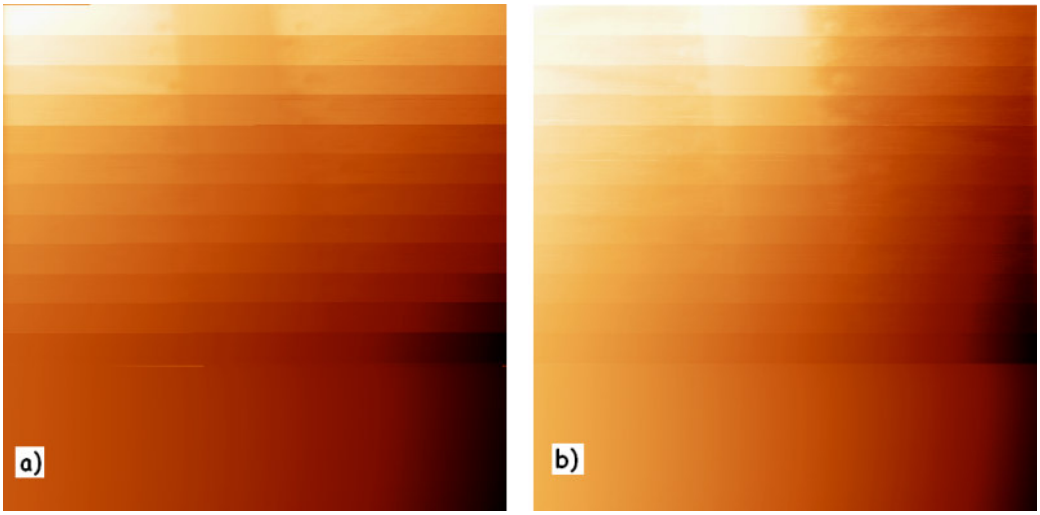

Figure 5.14: $15 \times 15 \mu m^2$ LFM scans taken in TR (a) and RETR (b) with the square tip.

between the high friction region (silicon) and the low friction pattern (OTS), give the convolution of the scanned area. Lines refer to changing in the applied load.

To better see this behavior, in figure 5.16 a linear LFM profile taken with the standard tip is compared with a line scan acquired with the square tip. We can see that the integral effect changes the border shape from a ripid jump to a round change.

The image 5.15 was then divided between the bare silicon surface and the OTS coated surface. For both areas, the lateral force signals at each applied load were acquired. The two resulting stairs graphs are shown in figure 5.17. The green line refers to the bare silicon substrate while the red line to the OTS coated surface. Each step corresponds to a different external applied force and return a frictional voltage V_{fric}. A smaller total friction for the OTS coated surface than for the bare silicon is visible for all the applied loads.

To calculate the friction coefficient from the Coulomb's law (1.29) we need to know the total external applied load. Total load is given by the applied load plus the adhesion force. To evaluate the adhesion force it is necessary to acquire a *Force vs Distance curve*, *FvsD*. A F vs D curve is a plot of the deflection of the cantilever versus the extension of the piezoelectric scanner, measured using a position-sensitive photodetector. A typical F vs D curve is shown in figure 5.18. The green line refers to the forward curve while the red one to the backward curve. The adhesion force is calculated by the pull-off tension, $V_{pulloff}$ (see section 1.5), i.e. the lower point in the red curve.

We can provide an estimate of the friction coefficient for the bare silicon and the patterned surface. We need some costants of the apparatus: $K = 41,6\,\mathrm{N/m}$ is the

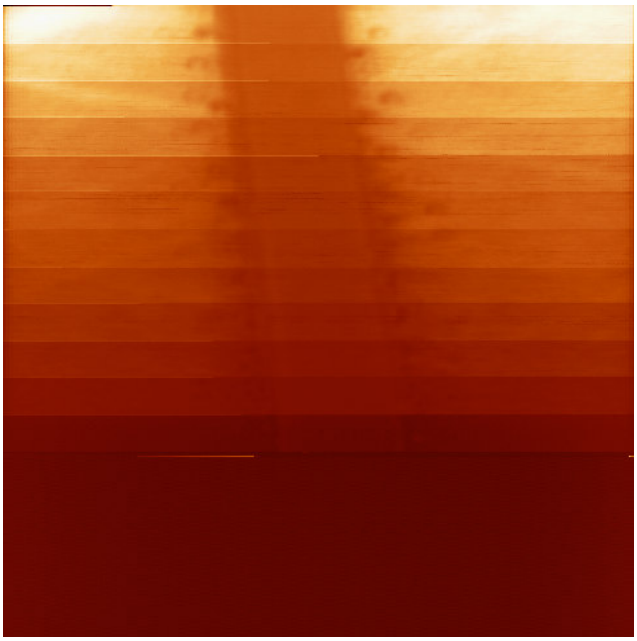

Figure 5.15: Filtered image obtained detracting the retrace signal by the trace one.

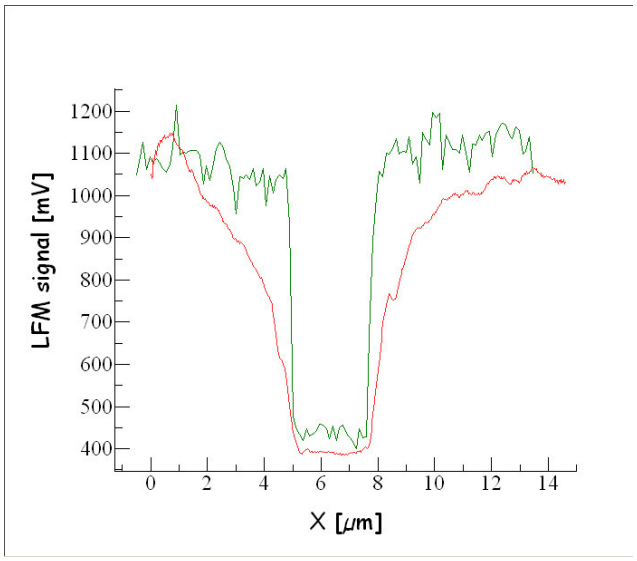

Figure 5.16: LFM line scans acquired with a standard tip (green line) and the square tip (red line) on the patterned silicon substrate.

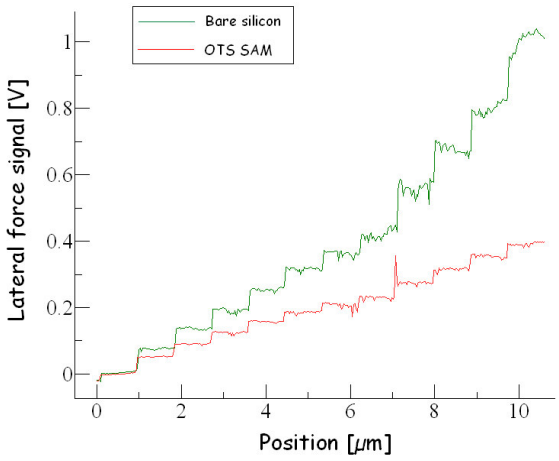

Figure 5.17: The lateral signal acquired for the bare silicon (green line) and OTS SAM (red line). Each step refers to a different applied load.

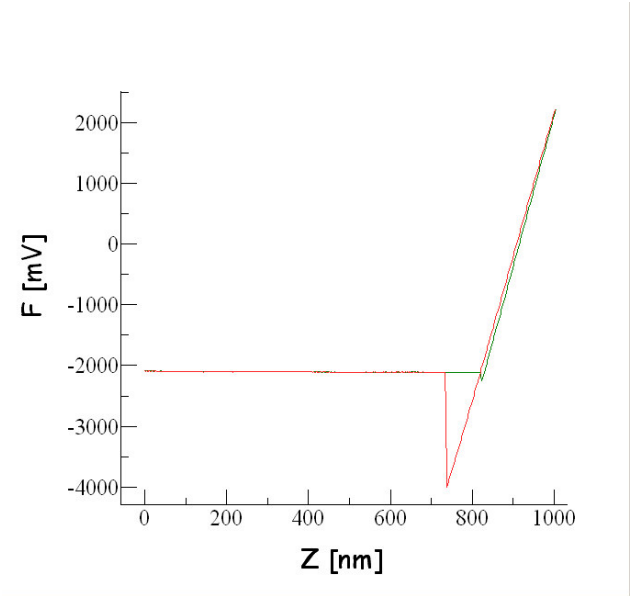

Figure 5.18: Typical force vs distance curve for our sample.

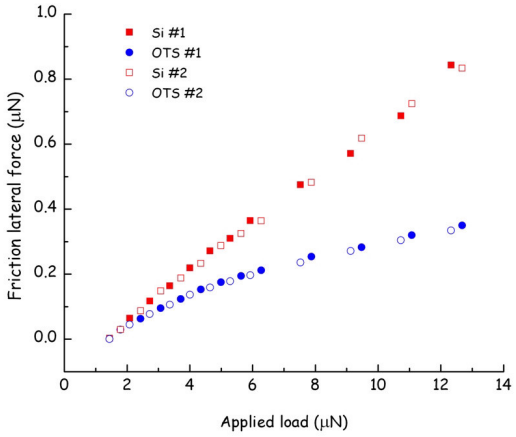

Figure 5.19: The measured frictional force at different applied load s plotted. Red points refer to the bare silicon surface while the blue points to the OTS SAM.

flection constant of the cantilever, $S = 38,484n\,\mathrm{m/V}$ the flectional sensitivity of the photodiode and $S_t = 41,55n\,\mathrm{m/V}$ is the torsional sensitivity of the photodiode. I have analized two scans in two different regions. The total applied load is calculated by: $F_{tot} = (V_{app} + V_{pulloff}) \cdot K \cdot S$. In the same way I have calculated the lateral force: $F_{lat} = V_{fric} \cdot K \cdot S_t$. Figure 5.19 summarized data acquired in two different sample regions for the bare silicon and the patterned OTS surface. Data are quite linear for silicon while OTS present a deviation from linearity for small total applied load. The friction coefficient for OTS deduced from these data is $\eta_{OTS} = 0,03$ while for silicon is $\eta_{\mathrm{Si}} = 0,07$. η_{OTS} is in good agreement with measurements taken by Carraro *et al.*[5] that give a static friction coefficient for a flat OTS SAM of $0,07$. The static friction coefficient value for the bare (100) silicon from litterature varies from $0,09$ to $0,65$[64].

The silicon surface of our sample presents spots of OTS outside the printed area as we can see in figure 5.13. The calculated value for η_{Si} is probably refered to a slightly contaminated surface. Then, our measurements give a lower value than those reported in litterature.

These measurements indicate that cover a silicon substrate with an OTS SAM is a good strategy to reduce friction by a factor of 2. Further studies will be done to evaluate the time stability of SAM submitted to different applied load and changes in the friction coefficient changing the head group of the SAM molecules.

Chapter 6

Conclusions and perspectives

In this thesis work I have investigated the frictional properties of homogeneous metal surfaces and micropatterned silicon surfaces.

- The slippage of N_2 films adsorbed on a Pb(111) substrate has been studied. The film is pinned to the surface for temperatures $< 15K$ while at $T = 19K$ sliding. This behavior is in good qualitive agreement with recent molecular dynamics simulations [61].

- Measurements done on Ne films adsorbed on different Pb(111) surfaces for $T < 7K$ are suggestive of a structural deppining: for low coverages Ne is commensurated with the surface while increasing the coverage Ne islands are incommensurated with Pb and the slippage increases. These data are consistent with molecular dynamic simulations of a model system under the assumption of weak corrugation of the surface-adatoms system [1].

- The electronic contribution to the total friction has been studied for the system Ne on Pb(111) across the superconducting transition temperature, $T_c = 7,2K$. Repeated temperature scans did not show changes in the dissipation while lead passed from normal conductor to superconductor. In all these measurements the superconducting transition was induced thermally. Future perspectives involve inducing superconducting transition by applying an external magnetic field in order to reduce the system perturbation.

- The slippage of heavy rare gases on Pb(111) has been studies for $T < 20K$. Ar films show slippage only for temperatures higher than $20K$ while Kr is pinned to the surface at these temperatures. Also for these systems the thermal activation is very important.

- Measurements acquired for the adsorption of Ne films on gold surfaces at $T \sim 7K$ show a slippage smaller than for Ne on Pb(111). The calculated slip

time τ_s is one order of magnitude smaller for gold than for lead. This is due to the different morphology of the two substrates. To study the electronic contribution to the total friction, the electronic coupling was reduced by coating the gold surface with a Kr insulating overlayer. We detected an increase in the slip time with increasing Kr layers until two monolayers. For higher Kr overlayers the slip time has a reentrant behavior. These are preliminary data and in the next future further measurements will be done to better understand this behavior. Further studies will be done changing the insulating layer: Xe and N_2 films will be used to study the influence of molecular polarizability on the friction.

- Preliminary measurements of slippage of gold nanoparticles (NPs) on gold at room and cryogenic temperatures show an unexpected behavior. NPs show slippage at $T \sim 6K$ on flat surfaces. The calculated slip time at cryogenic temperature is three times lower that that at room temperature. This is in contrast with a theramally activated diffusion of the NPs on the surface. In the next future systematically measurements will be carried out and an upgrade of the experimental apparatus is in progress to directly spray NPs in UHV chamber. Further studies will be done glueing a MICA substrate on the QCM electrodes to evaluate the frictional behavior of NPs on an atomically smooth surface.

- A procedure to produce patterned silicon surfaces via micro contact printing (μCP) of alkylsilane was perfectioned. Preliminary tribological studies were done with a modified AFM tip having a square tip wih a contatct area of $\sim 2 \times 2\mu m^2$. Measurements revealed a smaller friction coefficient for OTS patterned surface than for the bare silicon by a factor of 2. Next measurements will study the life time of the patterned surfaces submitted to an external load and the influence of the head group of SAM molecules to friction. Further studies will be done to produce with μCP patterns smaller than $2\mu m$.

Appendix A

Curriculum

A.1 Vita

Februry 09, 1980 Born, Tissi (SS), Sardinia, Italy

July 09, 1999 Certificate of Industrial Chemical Expert

July 14, 2004 Laurea degree in Physics

2008 PhD in Material Science

A.2 Pubblications

1. L. Bruschi, G. Fois, G. Mistura, K. Sklarek, R. Hillebrand, M. Steinhart and U. Gösele, *Adsorption hysteresis in higly ordered porous alumina*, submited to J. Chem. Phys. (2008);

2. D. Dattilo, L. Armelao, G. Fois, G. Mistura and M. Maggini, *Wettability modulation of flat and porous silicon surfaces coated with spyropiran*, Langmuir **23**, 12945 (2007);

3. G. Fois, L. Bruschi, L. d'Apolito, G. Mistura , B. Torre, F. Buatier de Mongeot, C. Boragno, R. Buzio and U. Valbusa, *Low temperature static friction of N_2 monolayers on Pb(111)*, J. Phys.: Condens. Matter **19,** 305013 (2007);

4. L. Bruschi, G. Fois, G. Mistura, M. Tormen, V. Garbin, E. di Fabrizio, A. Gerardino and M. Natali, *Complete wetting of curved microscopic channels*, J. Chem. Phys. **125**, 144709 (2006);

5. D. Dattilo, L. Armelao, M. Maggini, G. Fois and G. Mistura, *Wetting Behavior of Porous Silicon Surfaces Functionalized with a Fulleropyrrolidine*, Langmuir **22**, 8764 (2006);

6. L. Bruschi, G. Fois, A. Pontarollo, G. Mistura, B. Torre, F. Buatier de Mongeot, C. Boragno, R. Buzio and U. Valbusa , *Structural depinning of Ne monolayers on Pb at T<6.5K*, Phys. Rev. Lett. **96**, 216101 (2006);

7. L. Bruschi, G. Fois, A. Carlin and G. Mistura, *Observation of depinning phenomena in the nanofriction of cryogenic films*, in **Advances in contact mechanics: implications for materials science, engineering and biology**, editor R. Buzio (Transworld research network) 2006;

8. A. Pozzato, S. Dal Zilio, G. Fois, D. Vendramin, G. Mistura, M. Belotti, Y. Chen e M. Natali, *Superhydrophobic surfaces fabricated by nanoimprinting lithography*, Microelectronic Engineering **83**, 884-888 (2006).

A.3 Posters and presentations

- 09-13 September 2007, *First International Conference in Science of Friction*, Irago, Aichi, Japan. Talk titled: **Observation of depinning phenomena in the nanofriction of Ne monolayers on metallic surfaces**.

- 12-16 May 2007, *ESF-Nanotribology Workshop*, S. Margherita di Pula, Italy. Talk titled: **Observation of depinning phenomena in the nanofriction of cryogenic monolayers**.

- 3-4 November 2006, *Workshop "Nanotribologia"*, Modena, Italy. Talk titled: **Nanofriction of cryogenic monolayers on Pb and Au**.

- 19-20 December 2005, *Workshop "Nanotribologia"*, Genova, Italy. Talk titled: **Observation of intrinsic depinning in the nanofriction of Ne monolayers adsorbed on lead at T<7 K**.

- 1-6 July 2005, *VI Liquid Matter Conference*, Utrecht, Netherland. Poster titled: **Wetting of simple fluids in micropatterned surfaces.**

Appendix B

LabView^{TM} programs

In this appendix I show the programs that I have developed for contact angle measurements and to calculate automatically the slip time from data acquired during isothermal scans. Programs were developed with LabView^{TM} 7.1 sold out by National Instruments.

B.1 Contact angle measurements software

Figure B.1 shows a picture acquired by the camera mounted in our home made home-built apparatus. This program allows to apply some filters to the image to change its brightness or contrast, allows to select a square region in which it estrapolates the shape of the drop. It scans each pixel line and give coordinaes of edge points. Then automatically it performs a polinomial fit on the acquired points and give the slope of the contact line between the drop and the surface. Red points in the figure refers to the detected drop border. In the next pages I show the front panel and the scheme of the software.

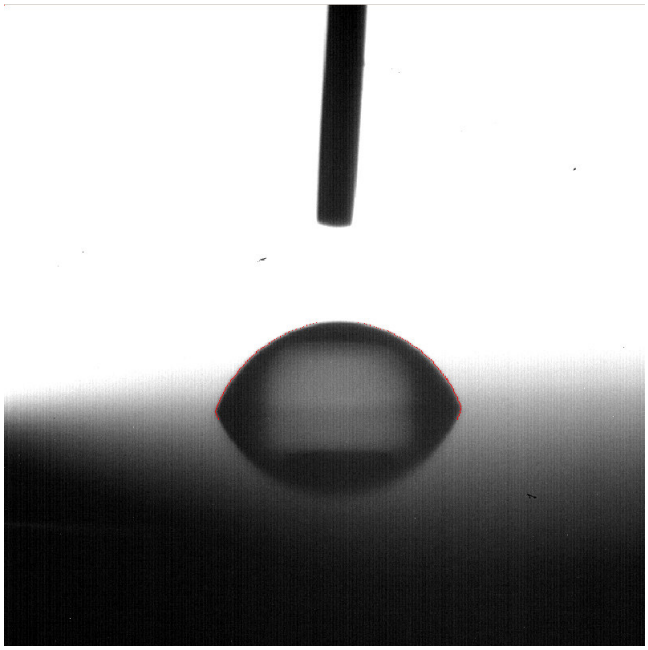

Figure B.1: Picture acquired with our home built apparatus for contact angles measurements.

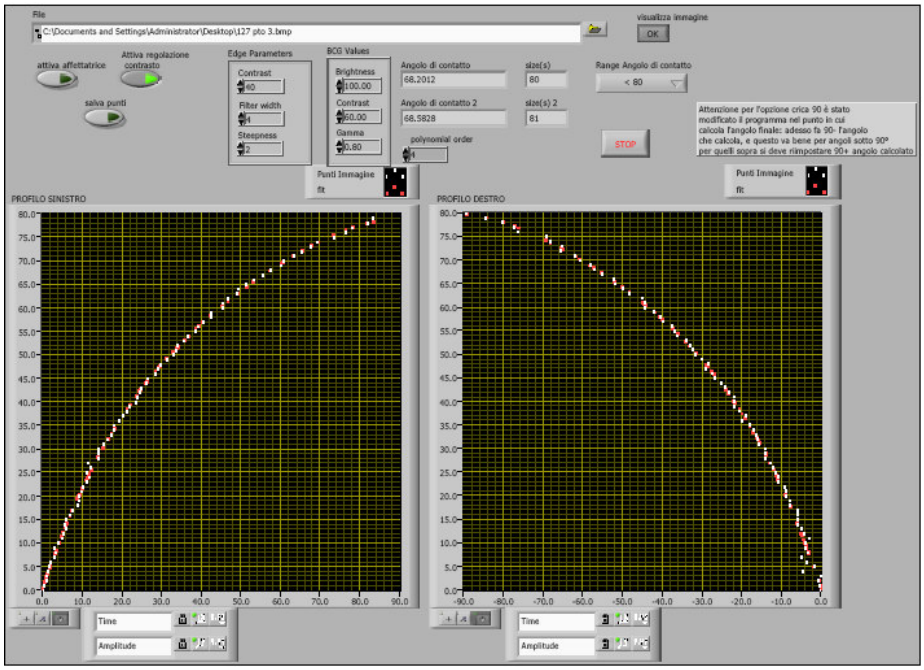

Figure B.2: Front panel of the software developed for the contact angle measurements.

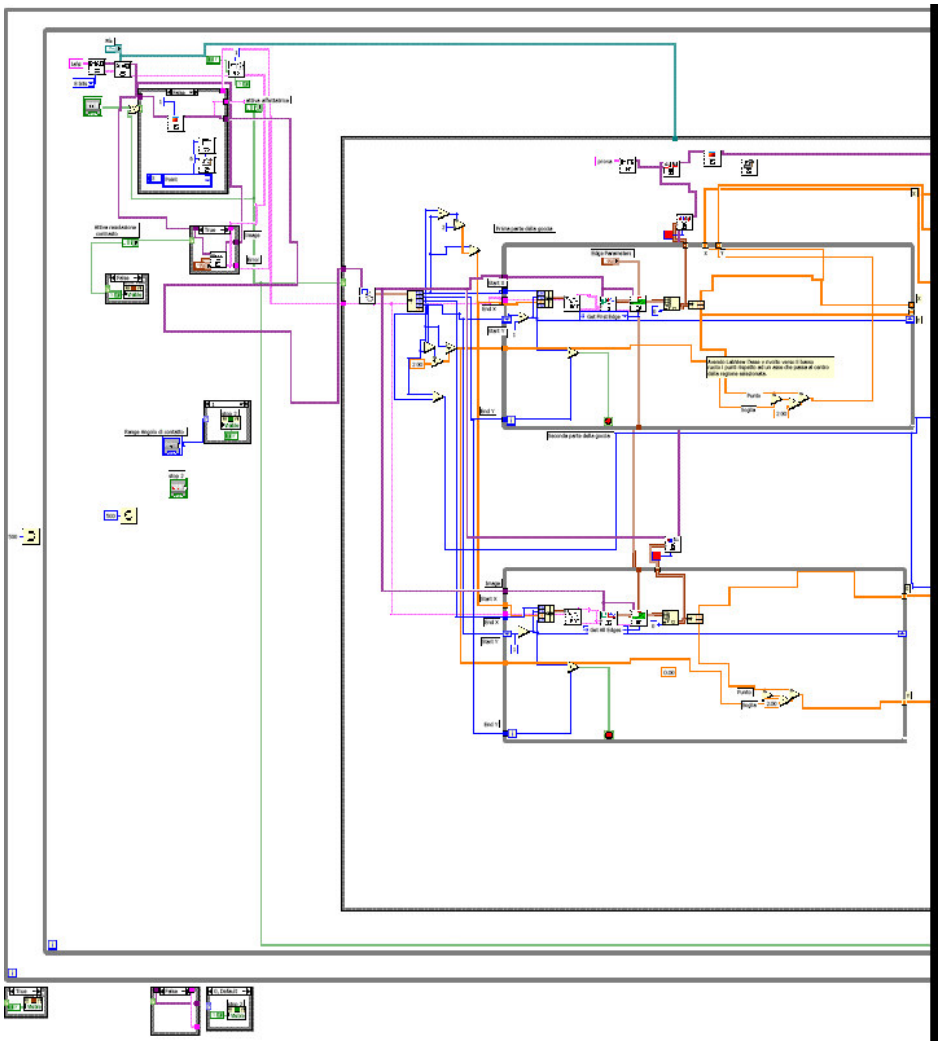

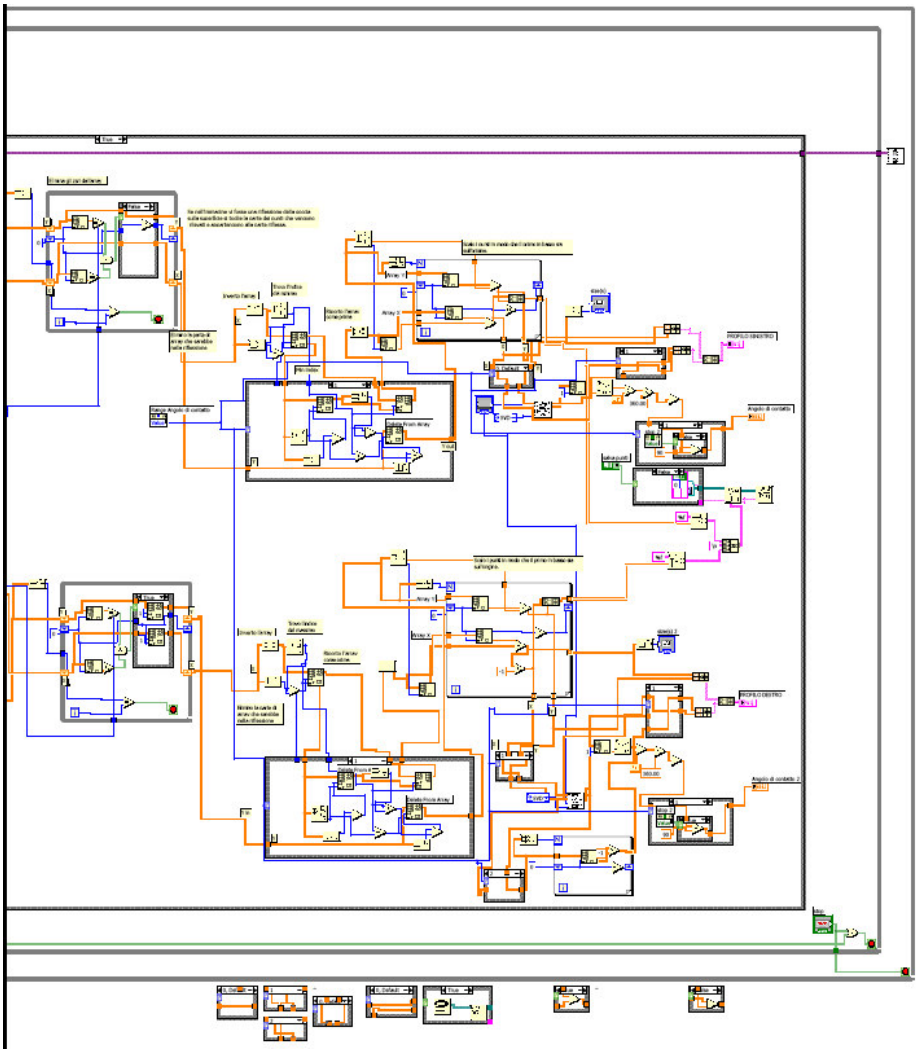

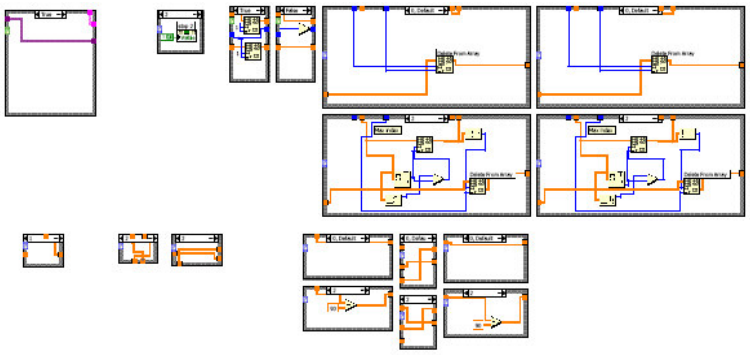

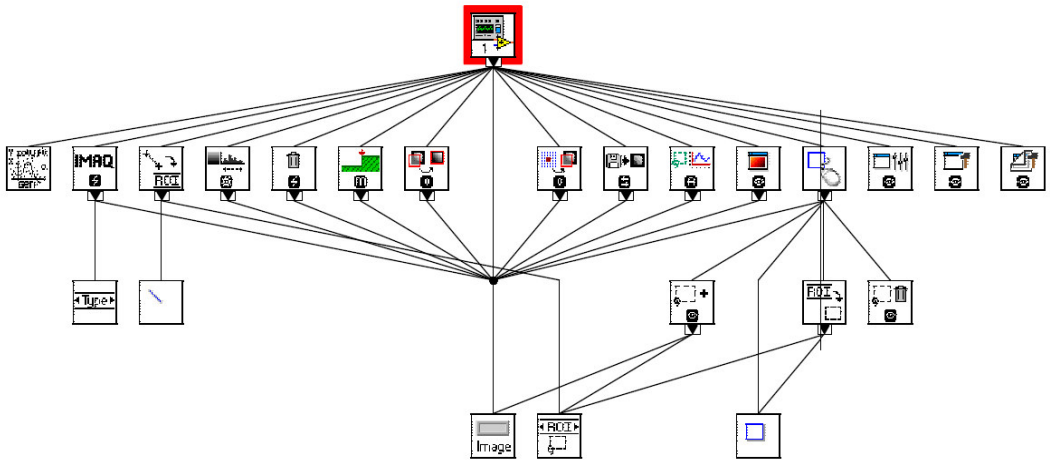

Figure B.3: Hierarchy of the software.

B.2 Slip time software

In this section I show the diagram of the software developed to calculate automatically the slip time directly from files saved with the experimental acquisition software[1].

[1]For the diagram of the data acqusition software see: G. Fois, *Misure di adsorbimento di gas nobili su superfici polimeriche microstrutturate*, Laurea degree thesis in Physics, Università degli studi di Padova, A. A. 2003-2004.

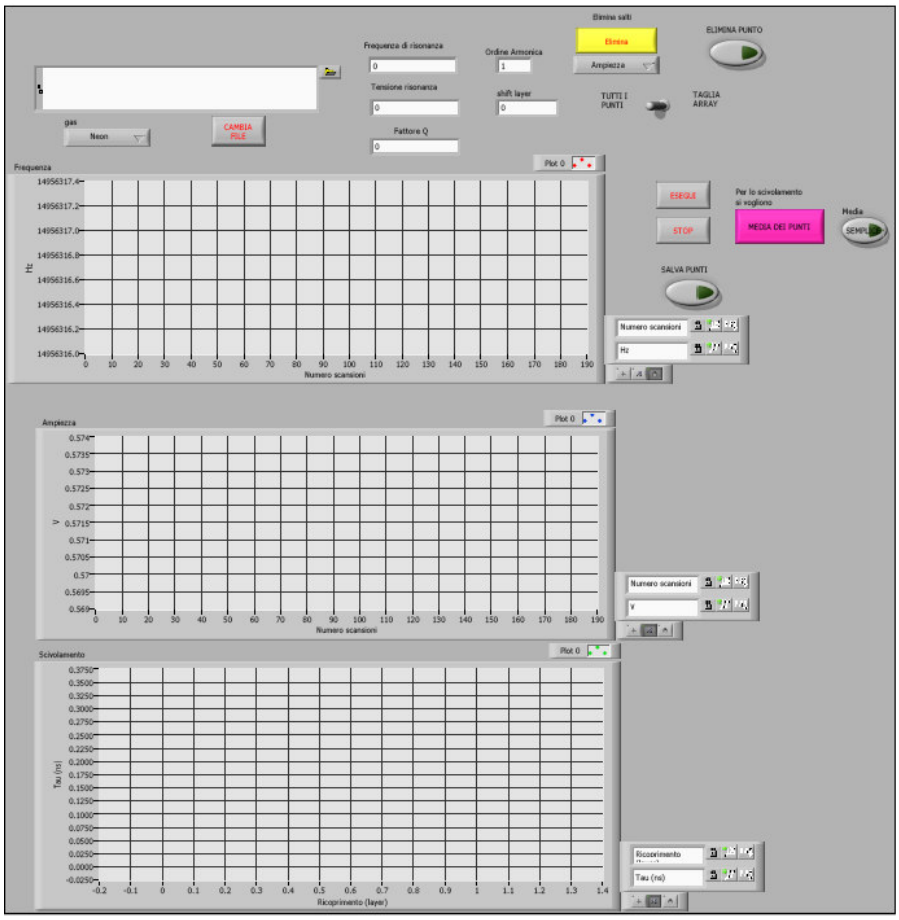

Figure B.4: Front panel of the software developed to calculate the slip time.

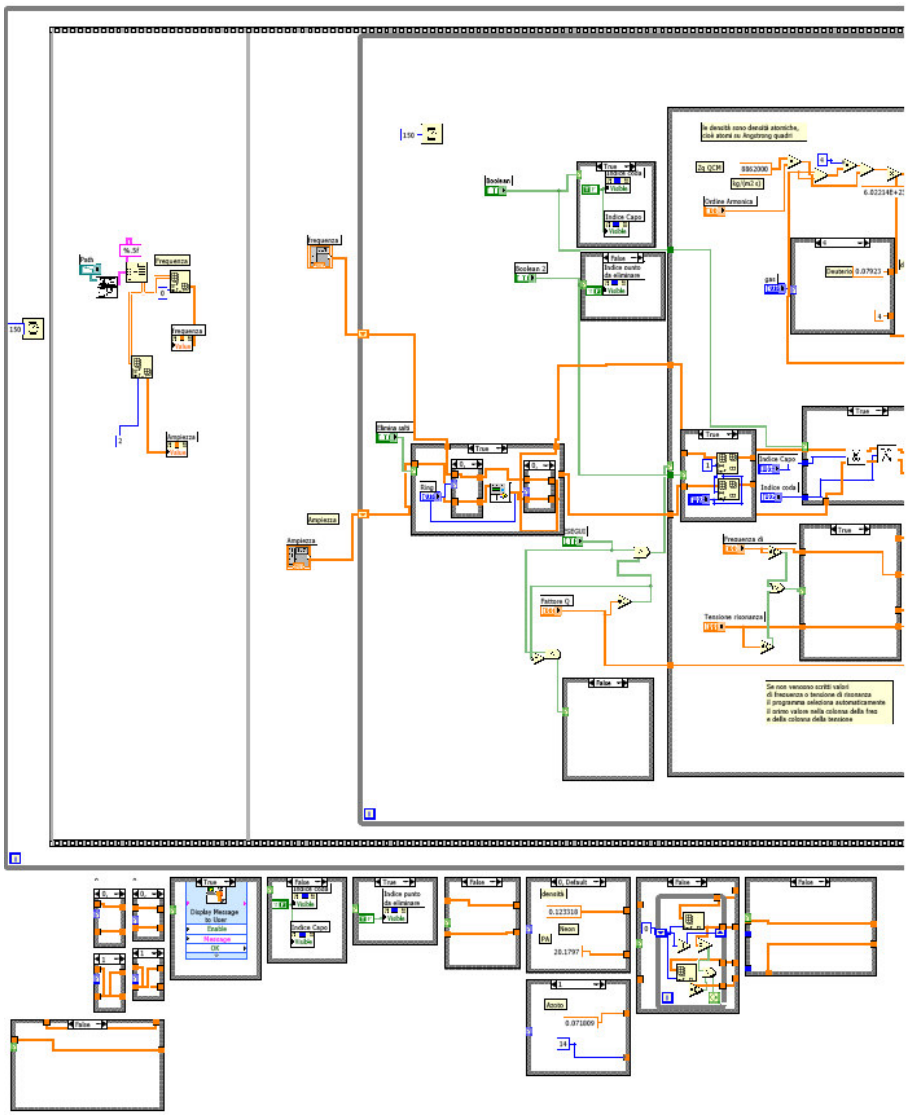

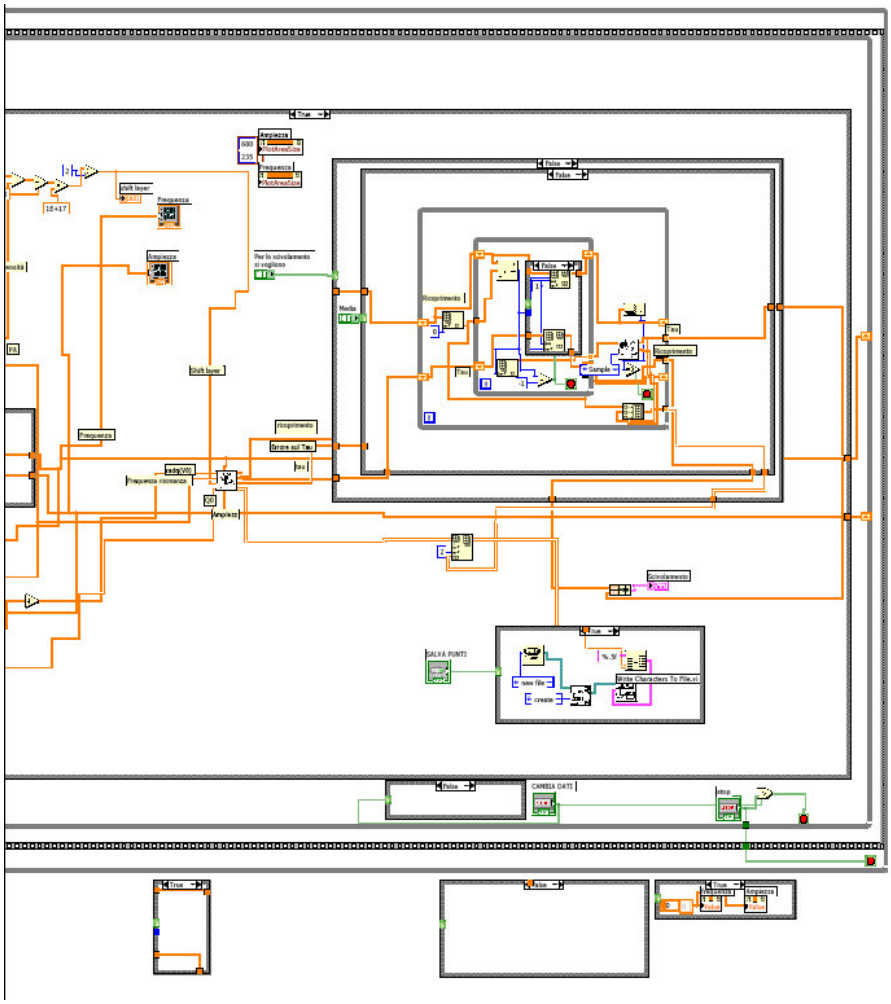

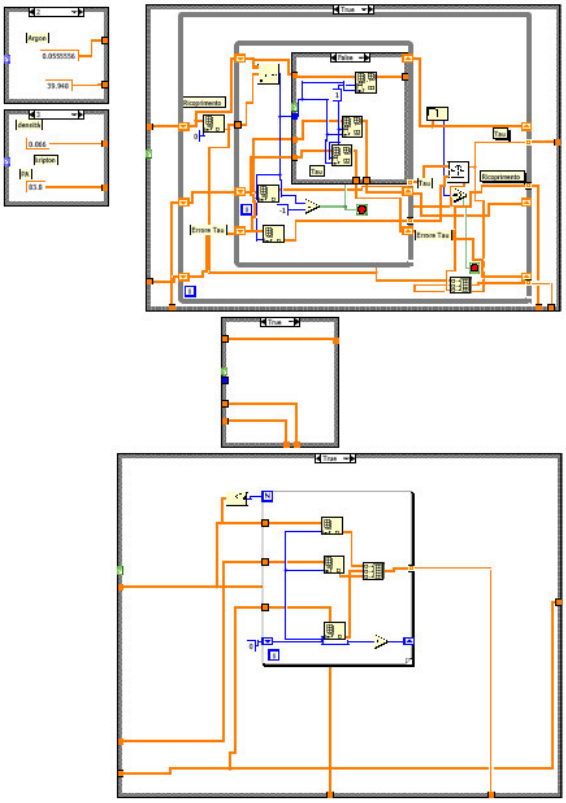

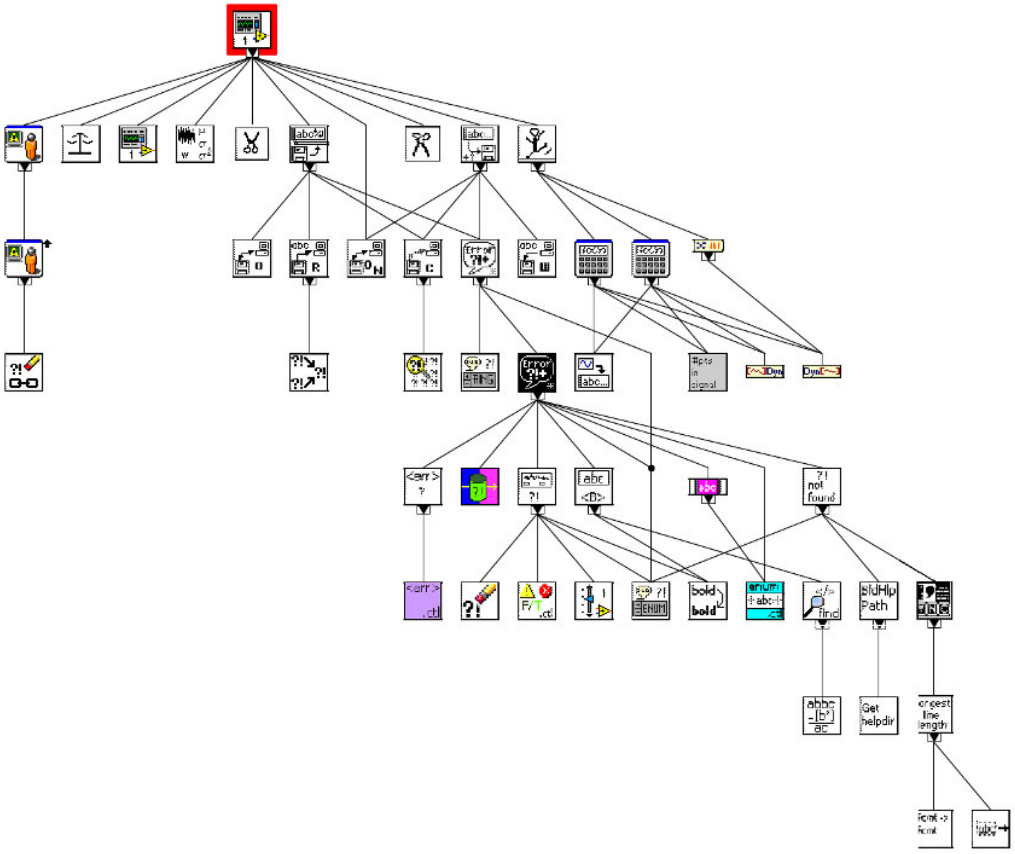

Figure B.5: Hierarchy of the software.

Bibliography

[1] B.N.J. Persson: *Sliding Friction: Physical Principles and Applications*, Springer (1998).

[2] D.Dowson, *History of Tribology*, Longman, NY, (1979).

[3] G. Amontons: *De la Resistance caus'ee dan les machines*, Memoires de l'Academie Royale, Chez Gerard Kuyper, Amsterdam, (1706) pp 257-282.

[4] F.P. Bowden, D. Tabor: *Friction and Lubrication* Methuen, London (1967).

[5] W. R. Ashurst, C. Yau, C. Carraro, R. Maboudian and M. T. Dugger, J. Microelectromech. Systems **41**, 10 (2001).

[6] M. Dienwiebel, G. S. Verhoeven, N Pradeep, J. W. M. Frenken, J. A. Heimberg and H. W. Zandbergen, Phys. Rev. Lett. **92,**126101 (2004).

[7] B.N.J. Persson: Phys. Rev. Lett. **71**, 1212 (1993); B. N. J. Persson: Phys. Rev. B **48**, 18140 (1993).

[8] H.A. Kramers: Physica **7,** 284 (1940).

[9] D. Schumacher: *Surface Scattering Experiments with Conduction Electrons*, Springer Tracts in Modern Physics, Vol.128, Springer, Berlin (1993); B.N.J. Persson: Surf. Sci. Rep. **33,** 83 (1999).

[10] A. Dayo, W. Alnasrallah and J. Krim: Phys. Rev. Lett. **80**, 1690 (1998).

[11] B.N.J. Persson and R. Rydberg: Phys. Rev. B **32**, 3586 (1985).

[12] J.A. Barker, D. Henderson and F.F. Abraham: Physica A **106**, 226 (1981).

[13] A.I. Larkin and Yu.N. Ovchinnikov: Journ. of Low Temp. Phys. **34**, 409 (1979).

[14] L. Bardotti, P. Jensen, A. Hoareau, M. treilleux, B. Cabaud, A. Perez and F. Cadete Santos Aires, Surf. Sci. **367**, 276 (1996).

[15] P. Deltour, J.L. Barrat and P. Jensen, Phys. Rev. Lett. **78**, 4597 (1997).

[16] W.D. Luedtke and Uzi Landman, Phys. Rev. Lett. **82** (19), 3835 (1999).

[17] L. J. Lewis,P. Jensen, N. Combe and J-L Barrat, Phys. Rev. B **61**, 16084 (2000).

[18] S. Pisov, E. Tosatti, U. Tartaglino and A. Vanossi, J. Phys.: Condens. Matter **19**, 305015 (2007).

[19] C. DeW. Van Siclen, Phys. Rev. Lett. **75**, 1574 (1995).

[20] H. Hertz, J. Reine Angew. Math., **92,** 156 (1881).

[21] K. Johnson, K. Kendall, and A. Roberts, Proc. R. Soc. Lond. **A324**, 301 (1971).

[22] A. Podestà, *Development of protocols for a quantitative characterization of morphological and tribological properties of nanostructured films via the Atomic Force Microscope*, PhD thesis, Facoltà di Scienze MM FF NN, Univeristà degli studi di Milano Bicocca (2001).

[23] Published by C. Lu and A.W. Czanderna: *Applications of Piezoelectric Quartz Crystal Microbalances* (Elsevier, Amsterdam 1984).

[24] J.A. Phillips, D. Ross, P. Taborek and J.E. Rutledge: Phys. Rev. B **58**, 3361 (1998) and references therein; G. Mistura, H.C. Lee and M.H.W. Chan: J. Low Temp. Phys. **96**, 1 (1994); D. Ross, P. Taborek and J.E. Rutledge: Phys. Rev. B **58** R4274 (1998); G.B. Hess, M.J. Sabatini and M.H.W. Chan: Phys. Rev. Lett. **78**, 1739 (1997).

[25] M. Chester, L.C. Yang and J.B. Stephens: Phys. Rev. Lett. **29**, 211 (1972).

[26] J Krim and A. Widom: Phys. Rev. B **38**, 12184 (1988).

[27] J. Krim: Scient. Am. **275**, 74 (1996).

[28] E.T. Watts, J. Krim and A. Widom: Phys. Rev. B **41**, 3466 (1990).

[29] L. Bruschi and G. Mistura, *The quartz crystal microbalance as a nanotribology technique* in *Nanotribology: Friction and Wear on the atomic scale*, edited by E. Meyer and E. Gnecco, (Springer, New York) (2006).

[30] L. Bruschi and G. Mistura: Phys. Rev. B **63**, 235411 (2001).

[31] K.K. Kanazawa: Farad. disc. **107**, 77 (1997).

[32] B. Borowsky, B.L. Mason and J. Krim: J. Appl. Phys. **88**, 4017 (2000).

[33] L. Bruschi, G. Delfitto and G. Mistura: Rev. of Scient. Instr. **70**, 153 (1999).

[34] L. Bruschi, G. Delfitto and G. Mistura: Rev. of Scient. Instr. (2006).

[35] M.J. Lea, P. Fozooni and P.W. Retz: Journ. of Low Temp. Phys. **54**, 303 (1984).

[36] M. J. Madou, *Fundamentals of microfabbrication: the science of miniaturization*, CRC Press (2002).

[37] S. Jensen, "*Inductively coupled plasma etching for microsystems*", PhD thesis, MIC Department of Micro- and Nanotechnology, Technical University of Denmark (2004).

[38] Y. Xia and G. M. Whitesides: Annu. Rev. Mater. Sci. **28**, 153 (1998) and its bibliography.

[39] A. Ulman, *An introduction to ultrathin organic films*, Academic Press (1991).

[40] G. M. Whitesides, P. E. Laibinis, Langmuir, **6**, 87 (1990); L. H. Dubois, R. G. Nuzzo, Annu. Rev. Phys. Chem., **43**, 437 (1992); A. Ulman, Mater. Res. Soc. Bull., **June**, 46 (1995); A. R. Bishop, R. G. Nuzzo, Curr. Opin.Coll. Interface Sci., **1**, 127 (1996).

[41] L. Libioulle, A. Bietsch, H. Schmid, B. Michel, and E. Delamarche, Langmuir **15**, 300 (1999).

[42] P. E. Laibinis, R. G. Nuzzo and G. B. Whitesides, J. Phys. Chem. **96**, 5097 (1992).

[43] J. L. Wilbur, H. A. Biebuyck, J. C. Macdonald and G. B. Whitesides, Langmuir **11,** 825 (1995).

[44] B.N.J. Persson and E. Tosatti:Surf. Sci. **411**, L855 (1998).

[45] V.L. Popov: Jetp Lett. **69**, 7, 520 (1999).

[46] T. Novotny and B. Velicky: Phys. Rev. Lett. **83**, 20, 4112 (1999).

[47] J.B. Sokoloff, M.S. Tomassone and A. Widom: Phys. Rev. Lett. **84**, 3, 515 (2000).

[48] B.N.J. Persson: Sol. St. Comm.**115**, 145 (2000).

[49] R.L. Renner, J.E. Rutledge and P. Taborek: Phys. Rev. Lett. **83,** 1261 (1999).

[50] R.L. Renner, P. Taborek and J.E. Rutledge: Phys. Rev. B **63**, 233405 (2001).

[51] J. Krim, D.H. Solina and R. Chiarello: Phys. Rev. Lett. **66**, 181 (1991).

[52] B.L. Mason, S.M. Winder and J. Krim: Trib. Lett. **10**, 59 (2001).

[53] G. Fois, L. Bruschi, L. d'Apolito, G. Mistura, B. Torre, F. Buatier de Mongeot, C. Boragno, R. Buzio and U. Valbusa, J. Phys.: Condens. Matter **19,** 305013 (2007).

[54] L. Bruschi, A. Carlin and G. Mistura: Phys. Rev. Lett. **88**, 046105 (2002).

[55] L. Bruschi, G. Fois, A. Pontarollo, G. Mistura, B. Torre, F. Buatier de Mongeot, C. Boragno, R. Buzio, and U. Valbusa, Phys. Rev. Lett. **96**, 216101 (2006).

[56] B.N.J. Persson, J. Chem. Phys. **103**, 3849 (1995).

[57] L. W. Bruch, Phys. Rev. B **61**, 16201 (2000).

[58] M.J. Rost, D.A. Quist and J.W.M. Frenken: Phys. Rev. Lett. **91**, 026101 (2003).

[59] L. Bruschi, G. Fois, A. Carlin and G. Mistura, in *Advances in contact mechanics: implications for materials science, engineering and biology*, editor R. Buzio (Transworld research network) (2006).

[60] B. Michel, et al: IBM J. Res. & Dev. **45**, 697 (2001).

[61] M. Barigazzi , G Santoro, A Franchini and V Bortolani, J. Phys.: Condens. Matter **19,** 305014 (2007).

[62] K. Mougin, H. Hamidar and G. Castelein, Coll. Surf. A **193**, 231 (2001).

[63] A. B. D. Cassie and S. Baxter, Trans. Faraday Soc. **40**, 546 (1944).

[64] www.memsnet.org/material/siliconsibulk/

Ringraziamenti (Acknowledgements)

Un ringraziamento particolare va ai miei supervisori prof. G. Mistura e prof. L. Bruschi per il costante appoggio e sostegno cha mi han dato in questi anni, a G. Delfitto per la parte tecnica e tutti i ragazzi che han lavorato al mio fianco qui al LaFSI.